A COMPREHENSIVE DARK MATTER ANALYSIS ON THE SPIRAL GALAXY NGC 4321 (M100)

TAN WEI SHEN

FACULTY OF SCIENCE
UNIVERSITI MALAYA
KUALA LUMPUR

2021

A COMPREHENSIVE DARK MATTER ANALYSIS ON THE SPIRAL GALAXY NGC 4321 (M100)

TAN WEI SHEN

DISSERTATION SUBMITTED IN FULFILMENT OF THE REQUIREMENTS FOR THE DEGREE OF MASTER OF SCIENCE

DEPARTMENT OF PHYSICS
FACULTY OF SCIENCE
UNIVERSITI MALAYA
KUALA LUMPUR

2021

UNIVERSITI MALAYA

ORIGINAL LITERARY WORK DECLARATION

Name of Candidate: **TAN WEI SHEN**

Matric No: **SMA170036 (17036082/1)**

Name of Degree: **MASTER OF SCIENCE**

Title of Dissertation ("this Work"):

A COMPREHENSIVE DARK MATTER ANALYSIS ON THE SPIRAL GALAXY NGC 4321 (M100)

Field of Study: **ASTRONOMY**

I do solemnly and sincerely declare that:

(1) I am the sole author/writer of this Work;
(2) This Work is original;
(3) Any use of any work in which copyright exists was done by way of fair dealing and for permitted purposes and any excerpt or extract from, or reference to or reproduction of any copyright work has been disclosed expressly and sufficiently and the title of the Work and its authorship have been acknowledged in this Work;
(4) I do not have any actual knowledge nor do I ought reasonably to know that the making of this work constitutes an infringement of any copyright work;
(5) I hereby assign all and every rights in the copyright to this Work to the University of Malaya ("UM"), who henceforth shall be owner of the copyright in this Work and that any reproduction or use in any form or by any means whatsoever is prohibited without the written consent of UM having been first had and obtained;
(6) I am fully aware that if in the course of making this Work I have infringed any copyright whether intentionally or otherwise, I may be subject to legal action or any other action as may be determined by UM.

Candidate's Signature Date:

Subscribed and solemnly declared before,

Witness's Signature Date:

Name:

Designation:

A COMPREHENSIVE DARK MATTER ANALYSIS ON THE SPIRAL GALAXY NGC 4321 (M100)

ABSTRACT

The dark matter analysis on the spiral galaxy NGC 4321 (M100) is studied by considering the nine different dark matter profiles so far lacking in the scientific literature, i.e. Pseudoisothermal, Burkert, NFW, Moore, Einasto, core-modified, DC14, coreNFW and Lucky13 profiles. In this thesis, the rotation curve analysis was done on the galaxy NGC 4321 by using nonlinear fitting of star, gaseous and dark matter halo equations with selected VLA HI observation data. Among the nine dark matter profiles, four dark matter profiles (DC14, Lucky13, Burkert and Moore profiles) showed declining features and hence found to be not suitable for this galaxy. This is concluded to be mainly due to the characteristics of those dark matter profiles and also due to the varying levels of problems within the internal region fittings. For the remaining five accepted dark matter profiles, the analysis was conducted by using the reduced chi-square test. Four out of the five accepted dark matter profiles lie within the range of $0.40 < x^2_{redu} < 1.70$, except for the case of the core-modified profile. In addition, Pseudoisothermal profile achieved the best fitting i.e. x^2_{redu} nearest to 1, mainly due to its linearity in the internal region and flatness at large radii. Further investigation was also made into the addition of an extra tracer for better accuracy of the dark matter mass by using the carbon monoxide (CO) molecular gas in the galaxy NGC 4321. Five accepted dark matter profiles, Pesudoisothermal, NFW, Einasto, core-modified and coreNFW profiles are adopted to compute the mass of dark matter and compare between each profile. The resultant mass of dark matter via CO (using the ALMA data) in the internal region is added to the dark matter mass via HI (using the VLA data) in the external region for each dark matter profile. An interesting outcome was found whereby the amount of dark matter mass calculated using both CO and HI is found to be higher than using the traditional estimations of only HI within 2.9 kpc in three out

of five dark matter profiles (i.e. NFW, Einasto, coreNFW profiles). Furthermore, when the internal region covered by CO is considered up to the maximum range of 1.3 kpc to 1.5 kpc, the maximum accuracy increment in the dark matter mass is found to be consistent for all three profiles ranging from 4% to 6%.

Keywords: Cosmology, Rotation Curve, Dark Matter, Neutral Hydrogen, Carbon Monoxide, Radio Astronomy, Spiral Galaxy

JIRIM GELAP KOMPREHENSIF ANALISIS PADA GALAKSI PILIN NGC 4321 (M100)

ABSTRAK

Jirim gelap analisis pada galaksi pilin NGC 4321 (M100) dikaji dengan menggunakan sembilan jirim gelap profil yang berbeza, kekurangan dalam saster ilmiah setakat ini, iaitu Pseudoisothermal, Burkert, NFW, Moore, Einasto, core-modified, DC14, coreNFW dan Lucky13 profil. Dalam tesis ini, putaran lengkung analisis telah dijalankan pada galaksi NGC 4321 dengan menggunakan penyuaian persamaan yang tidak linear pada bintang, gas dan taburan halo jirim gelap dengan VLA HI data cerapan yang dipilih. Antara sembilan jirim gelap profil, empat jirim gelap profil (DC14, Lucky13, Burkert and Moore profil) menunjukkan ciri-ciri yang merosot dan oleh itu didapati tidak sesuai untuk galaksi pilin ini. Ini terutamanya disebabkan oleh ciri-ciri jirim gelap profil tersebut dan juga disebabkan oleh pelbagai tahap masalah di penyuaian jejari dalaman. Manakala untuk lima jirim gelap profil lain yang diterima, analisis telah dibuat dengan menggunakan ujian pengurangan khi-kuasa dua. Empat daripada lima jirim gelap profil yang diterima terletak dalam lingkungan $0.40 < x^2_{redu} < 1.70$, kecuali untuk kes core-modified profil. Di samping itu, Pseudoisothermal profil mencapai penyuaian yang terbaik, iaitu x^2_{redu} terdekat kepada 1, ini terutamanya disebabkan oleh garis liniernya di jejari dalaman dan kerataan pada jejari yang lebih besar. Penyelidikan yang lebih lanjut telah dijalankan untuk ketepatan jisim gelap dengan menambahkan gas molekul karbon monoksida (CO) sebagai pelacak tambahan. Lima jirim gelap profil dipakai untuk menghitung jisim gelap dan membandingkan antara setiap profil. Jisim jirim gelap yang dihasilkan melalui CO (menggunakan data ALMA) di kawasan dalam akan ditambahkan ke jisim jirim gelap yang dihasilkan melalui HI (menggunakan data VLA) di kawasan luar untuk setiap jirim gelap profil. Keputusan yang menarik telah didapati di mana jumlah jisim gelap yang dikira dengan menggunakan CO dan HI didapati lebih tinggi daripada menggunakan

anggaran tradisional dengan menggunakan hanya HI dalam 2.9 kpc di antara tiga daripada lima jisim gelap profil (i.e. NFW, Einasto, coreNFW profil). Selanjutnya, kawasan dalam yang diliputi oleh CO dipertimbangkan ke maksimum apabila julat dari 1.3 kpc ke 1.5 kpc, kenaikan ketepatan maksimum dalam jisim gelap didapati konsisten untuk ketiga-tiga profil bermula dari 4% ke 6%.

Kata Kunci: Kosmologi, Jirim Gelap, Astronomi Radio, Galaksi Pilin, Putaran Lengkung, Hidrogen Neutral, Karbon Monoksida

ACKNOWLEDGEMENTS

This journey would not be possible without the support of my family, supervisors, colleagues, and friends. First of all, I want to thank my family, my mom, dad, sisters, brother-in-law, nephews and niece who always provide me love and guidance in whatever I working. I feel grateful and will never forget their encouragement in all of my pursuits and the continuous support they have given me throughout this master journey.

Next, I want to express my heartiest acknowledgement to my research supervisors, Associate Prof. Dr. Zamri Zainal Abidin and Dr. Norsiah Hashim, for providing me the chance to conduct the research and giving instructions throughout the study. Both supervisors have given me huge individual and professional recommendations. It was a great privilege and honor to work and study under their guidance. I would also want to special thanks to Dr. Juan Carlos for giving me the chance for a newspaper appearance for the black hole imaging research translation to Chinese words.

Apart from that, I thank you to all lecturers for the knowledge sharing and LOC for successfully organizing the school and workshop I attended, ISYA school in China, VLBI workshop in Malaysia, Gravitational Wave school in Taiwan, online Indonesia ITB school, online Korea KIAS workshop, online Japan KMI School, online Malaysia CASA workshops, online NAOJ Winter School, and online East Asian VLBI workshop.

In ISYA school, I have learnt a lot from 16 lecturers. Furthermore, I have met 38 friends from 14 countries. Whenever I feel stress or depress, I gain a lot of motivation when I will think of them, a group of astronomy friends fighting hard somewhere on this Earth. In the Gravitational Wave school, I gain a lot of knowledge from 5 lecturers. Besides, I am happy to meet many new friends from different countries in Gravitational Wave school. It was really nice to know them and had an unforgettable experience travel Taiwan with them.

I am extending my thank you to my study colleagues, Danial, Shazwan, Zhan Hao, Sasi, Zul, Shaiful, Hassan, Ridhauddin Aziz and Dr. Farah for their guidance and knowledge from the first day I met them until today. In addition, I want to thank my lunch friends Zhan Hao, Wen Sin, Ah Gan, Jing Wen, Ojibala, Max, Hong Chun and Yen Theng for bringing me to delicious food, nice sightseeing hiking and badminton session.

I also want to thank all companies and jobs I worked during my master study, working in Antlysis with my friends James Lee and Han Zhong, working as a part time actor for two movies, working as a tuition teacher for four classes and three one-to-one students and working as a Test Development Engineer in On Semiconductor. Finally, my thanks go to all my working colleagues and friends who have supported and inspired me to complete the research work.

TABLE OF CONTENTS

LIST OF FIGURES

LIST OF TABLES

LIST OF SYMBOLS AND ABBREVIATIONS

α	:	Alpha
θ	:	Azimuth Angle
β	:	Beta
$\boldsymbol{\chi^2}$	:	Chi-Square
ρ	:	Density
ϵ	:	Epsilon
f_n	:	Function
γ	:	Gamma
G	:	Universal Gravitational Constant
i	:	Inclination Angle
κ	:	Kappa
M	:	Mass
N	:	Number of Data Points
r	:	Radius
x^2_{redu}	:	Reduced Chi-Square
σ	:	Sigma
V	:	Velocity
X	:	The Stellar-to-halo Mass Ratio
ALMA	:	Atacama Large Millimeter/ Submillimeter Array (ALMA)
ASKAP	:	Australian Square Kilometre Array Pathfinder
BIMA	:	Berkeley-Illinois-Maryland Association
BINGO	:	Baryon Acoustic Oscillations in Neutral Gas Observations
CASA	:	Common Astronomy Software Application
CDM	:	Cold Dark Matter

CHIME	:	Canadian Hydrogen intensity Mapping Experiment
CO	:	Carbon Monoxide
DC14	:	Di Cintio et al. 2014
Dec	:	Declination
DM	:	Dark Matter
FAST	:	Five-hundred-meter Aperture Spherical Telescope
Hα	:	H-alpha
HI	:	Neutral Hydrogen
HII	:	Ionized Hydrogen
HIRAX	:	Hydrogen Intensity and Real-time Analysis eXperiment
ISM	:	Interstellar Medium
MeerKAT	:	Karoo Array Telescope
Mom	:	Moment Map
NFW	:	Navarro, Frenk and White
NGC	:	New General Catalogue
NII	:	Ionized Nitrogen
NRAO	:	National Radio Astronomy Observatory
PSF	:	Point Spread Function
PV	:	Position-Velocity
RA	:	Right Ascension
RC	:	Rotation Curve
rms	:	Root Mean Square
SKA	:	Square Kilometre Array
VLA	:	Very Large Array

LIST OF APPENDICES

CHAPTER 1: INTRODUCTION

1.1 Research Background

Dark matter is one of the longest investigations in cosmology history. Until today, dark matter is one of the significant research in the cosmos and there is still a lot of unsolved mysteries about dark matter. In a galaxy, the composition of the baryonic matter could not explain the observed distribution (Albert Bosma, 1981). In more detail, the profiles indicate that the composition of light cannot be equal with the composition of mass in a galaxy (Persic et al., 1996). In general, there is an existence of an extra and indiscernible mass matter (Albert Bosma, 1981; Faber & Jackson, 1976; Rubin et al., 1978). This is often explained by an additional mass component, which is the dark matter halo (Donato et al., 2009).

A galaxy is a gravitationally attracted body that is made up of stars, interstellar gas, dust and dark matter (Sparke & Gallagher III, 2007). The range in size of galaxies is from dwarfs with a few hundred million (10^8) stars to the giants with one hundred trillion (10^{14}) stars, which every one of them is rotating the central of galaxy respectively (Uson et al., 1990). In 2016, researchers have updated the galaxies number in the visible cosmos from the past prediction of about 200 billion ($2x10^{11}$) (Gott III et al., 2005) to a suggested at least 2 trillion ($2x10^{12}$) (Fountain, 2016). Furthermore, the overall of stars in the galaxies is as many as an estimated $1x10^{24}$ (Marov, 2015), which means there are more stars in the universe than all the grains of sand on the Earth (Mackie, 1999). The diameter of most of the galaxies is from one thousand to one hundred thousand parsecs (approximately three thousand to three hundred thousand light-years) and the distances between galaxies are divided into the order in million parsecs (or mega parsecs).

Galaxies are classified based on their visual morphology, which is spiral, elliptical and irregular (Jarrett, 2000). The dark matter mass composition of an elliptical galaxy can be

measured by using the virial theorem, together with the measured velocity distribution (Faber & Jackson, 1976). For spiral galaxies, the dark matter mass distribution can be identified by using rotation galaxy curves (Jog, 2002). The dark matter mass of the irregular galaxies can be measured by using the universal rotation curve with the gamma-ray telescope (Gammaldi et al., 2018). The targeted galaxy NGC 4321 is a spiral galaxy, hence the rotation curve will be selected as the method to analyze the dark matter distribution in this research.

Rotation Curve (RC) has been applied to detect the presence, capacity and composition of the dark matter (Donato et al., 2009). Rotation curve is a graph variation of the rotational velocity of all matter in the galaxy against the different distances from its center. The rotational velocities vary with radius reflects the composition of the mass in a galaxy. The formula of the velocity is included the mass of the galaxy, which means if the mass of a galaxy is high, its velocities of light emitted are supposed to be high as well. The rotation curves of most galaxies illustrate steep raising in the central of the galaxy, then gradually raising and finally becoming constant in the external of the galaxy. The flatness of the rotation curves in the external indicated that the galaxies contain a huge number of dark components (Xin & Zheng, 2013). Nonlinear rotation curve model is the model made by various formula and calculation of all matter in the galaxy, especially neutral hydrogen (HI) and carbon monoxide (CO) since these are the main component that contributes to the mass of the galaxy (Hashim et al., 2015).

The HI line is a very strong equipment to acquire the kinematics of the spiral galaxies, this is due to its radial area being usually larger, which is about three or four times larger than the observable disk. Bosma studies (Albert Bosma, 1978, 1981; A Bosma & Van der Kruit, 1979) act a significant fundamental part in building the foundation about the research of HI line on spiral rotation curves. Due to the HI disk extent, it is often more

susceptible than the stellar disk to do research studies via the hydrodynamical (ram-pressure stripping) interactions and the external gravitational (tidal interactions, galaxy mergers) (Džudžar et al., 2019). These characteristics show that the HI gas is an outstanding tracer of the physical processes that are influencing the galaxies (Barnes et al., 2001; Gunn & Gott III, 1972; Hess et al., 2017; Verdes-Montenegro et al., 2001; Yun et al., 1994), include tracer for observation data which use on rotation curve for dark matter studies.

CO constitutes a huge contribution to the total interstellar gas mass in many galaxies and dominates the composition of the interstellar medium (ISM) in the central regions of most luminous spiral galaxies (J. Young & Scoville, 1982). CO molecular lines are one of the most common methods for deriving rotation curves because of the huge density of molecular gas in the central of many galaxies, also the high angular and velocity resolutions in the CO observations (Sofue et al., 1999).

1.2 Problem Statement

The past CO rotation curve researches by Ali (Ali et al., 2019) have intensively concentrated in the center area of the spiral galaxy NGC 4321, which is up to a radius of 0.7 kpc and only uses one dark matter halo model. The extraordinary findings of the dark matter in the center area of this galaxy indicate the demand for extra researches to understand more about the comprehensive dark matter halo composition in the galaxy. To fill this literature gap, this research will obtain the data up to the higher radius to determine the entire dark matter halo distribution of this galaxy. Generally, the CO observed data is focused on the central region of the galaxy. For the purpose of obtaining the overall dark matter halo model distribution, the HI observed data will be employed, since the HI data can be observed up to a higher radius than the CO data. Apart from the higher radius obtained, the dark matter profile applied is also being paid attention. Previous dark matter analysis by Ali only apply one dark matter profile. Meanwhile, in

this research, the nine dark matter halo models will be applied to further understand how the dark matter distribute in this galaxy by using different dark matter halo models. The nine dark matter halo models used are Pseudoisothermal, Burkert, NFW, Moore, Einasto, core-modified, DC14, coreNFW and Lucky13 dark matter profiles. This research aims to deliver the following issues: What is the dark matter distribution when the observed data change to use by HI instead of CO? How is the dark matter distribution by applying the nine different dark matter halo models? Which dark matter halo model performs the best fit rotation curve by using reduced chi-square test?

Usually, HI is used as observed data to determine the mass of dark matter since HI is a strong equipment to capture the kinematics of spiral galaxies, mainly due to its radial region being three or four times than observable disk (A Bosma & Van der Kruit, 1979). However, if only considering HI, there would be a loss in the mass of dark matter in the central region due to HI is often weak or absent in the central regions (Sofue & Rubin, 2001). As a metaphor, measuring the mass of dark matter by using HI only is just like a doughnut, the external part is filled but the central part is empty. For the purpose of having a complete mass of dark matter in a galaxy, CO is the best puzzle piece to fill in the empty central part of this doughnut (HI). This is because the central few kpc of the galaxy is dominated by CO molecular gas (Garcia-Burillo et al., 1993; Kenney & Young, 1988; Nakai et al., 1994; Sakamoto et al., 1999; J. Young & Scoville, 1982; J. S. Young et al., 1995). Hence to have a full picture of the mass of dark matter, it is important for us to measure the mass of dark matter by considering both HI and CO at the same time. This research will further discuss the following questions: For the total dark matter mass, which range of internal radius should cover by CO and which range of external radius should cover by HI? How much the accuracy of dark matter mass can be increased by comparing the total dark matter mass by both HI and CO with the dark matter mass by

HI only? Does the accuracy increment have any similarity among the different dark matter profiles?

1.3 Research Objectives

(a) Analyze the dark matter distribution in the galaxy NGC 4321 to a larger radius by applying the HI observed data

HI observed data are most often derived from velocity fields. A velocity field gives a compact dynamics of a galaxy by allocating a typical velocity to every spatial position (De Blok et al., 2008). Its accurate data on every spatial position and leads to a larger radius are the reasons why the HI line has been selected as observed data to analyze the dark matter in this galaxy.

(b) Identify the best model among the dark matter profiles for the galaxy NGC 4321

The dark matter halo profiles can be classified into the cored profile and cuspy profile. In this research, both cored and cuspy profiles would be used. Seven cored profiles and two cuspy profiles, a total of nine dark matter profiles would be selected for the dark matter analysis on this galaxy. The seven cored profiles selected are Pseudoisothermal, Burkert, Einasto, core-modified, DC14, coreNFW and Lucky13 profiles, while the two cuspy profiles selected are NFW and Moore profiles. The rotation curve will be constructed by applying these nine dark matter halo models and identifying the best fit dark matter halo model by examining the dark matter distribution and applying reduced chi-square test.

(c) Compute the mass of dark matter in the spiral galaxy NGC 4321

The mass of dark matter in a galaxy is very important for future researcher studies comparison. The mass of the dark matter halo of a spiral galaxy can be calculated by using the dark matter halo model. After the rotation curve fitting by applying the nine

dark matter profiles, some of the profiles will be accepted and some of the profiles will be rejected. This is because each dark matter model is built by different equations and specific theory respectively. The mass of dark matter halo in the spiral galaxy NGC 4321 will be computed by obtaining those accepted dark matter profiles.

(d) Evaluate the accuracy of dark matter mass improved in the galaxy NGC 4321 by considering both HI and CO

Up to the knowledge, the internal region of a galaxy is usually dominant by CO while the other region can be detected by HI. The summation of the dark matter mass will be done by using CO in the internal region with the dark matter mass by using HI in the external area of the galaxy. Furthermore, the comparison of this summation with both the internal and external region by using HI only will be made to determine the percentage of maximum increase in accuracy of dark matter mass.

1.4 Significant of Research

The study is aimed to analyze the dark matter distribution by applying the nine different dark matter profiles and by considering HI and CO observed data on a spiral galaxy, particularly NGC 4321, which is so far lacking in the scientific literature. This study implied the method by applying nonlinear fitting of star, gaseous and dark matter halo models with the selected HI and CO observation data. These methods, if successful, would lead to a significant study on other galaxies. In addition, these two techniques will identify the best model among the nine dark matter halo models and the accuracy of dark matter halo mass improved by considering both HI and CO in the galaxy NGC 4321.

CHAPTER 2: LITERATURE REVIEW

2.1 Dark Matter

For the last 80 years, a new concept had arisen in which the visible matter observed in current telescopes are only representing a low percentage of the total mass in the Universe. Most of the matter is emerging in the form of not emitting light, or very little. Most of these matters are known as dark matter. Until today, this elusive component is still a huge mystery and one of the most important investigations in the Universe (Zackrisson, 2005).

The first dark matter detection is attributed to Zwicky, a Swiss-American astronomer who is the most famous pioneer in the dark matter research. In 1933, he researched the redshifts of a few galaxy clusters and identified a big scatter in the apparent velocities of the galaxies within the Coma Cluster, with differences that exceeded 2000 kms^{-1} (F Zwicky, 1933). Zwicky researched deeper by applying the virial theorem to estimate the mass of the cluster. He found that 800 galaxies in the distance of 106 light-years should display a velocity dispersion of 80 kms^{-1}. However, the observation only reveals an average velocity dispersion of approximately 1000 kms^{-1}. From there, he concluded that there was evidence which 85% of the universe's matter was non-luminous, or "dark" (Fritz Zwicky, 1933) and the investigation has grown increasingly since then.

The research by Zwicky on the Coma Cluster was continued by Sinclair Smith (1936) to an estimate the mass of the Virgo cluster of galaxies. Smith calculated that the total mass of the Virgo cluster is $10^{14}M\odot$, when this mass divided by the number of observed galaxies, the average mass per galaxy is $2 \times 10^{11}M\odot$, which was much higher than Hubble's estimate $10^{9}M\odot$ (Bertone & Hooper, 2018). Much like Zwicky, Smith thought this large number of mass-per-galaxy which implied by his calculations is an issue, since it was a mismatch with Hubble's estimate. However, he also acknowledges that both

could be correct, which the difference represents internebular material surrounding the galaxies. But again, the velocities of the constituent galaxies illustrated that there is an unexpectedly high mass-to-light ratio (Smith, 1936).

A few years later on the year 1939, Horace Babcock used the optical spectroscopy technique to compute the rotational velocity of the Andromeda galaxy (M31), which is the nearest large galaxy in the neighborhood of the Milky Way. Horace Babcok presented M31 out to 100 arc minutes away from the central of the galaxy and he identified that the rotational velocity at large radii is too large if it only contains luminous components (Babcock, 1939). Approximating M31 as a sphere and is surrounded by a flattened ellipsoid, he measure the mass composition of the galaxy and implied there is a presence of huge value of mass in the external region of the galaxy.

In 1959, Franz Kahn and Lodewijk Woltjer recommended a spectacular idea to resolve the total mass combined by the galaxy M31 and the Milky Way. From the velocities of the galaxy M31 and Milky Way moving towards each other, they derived the mass of the Local Group of galaxies. They estimated a lower bound mass of the M31-Milky Way system by expecting these two galaxies are part of a bound system. However, this lower bound was 6 times higher than the latest accepted mass in the system. By comparing this estimated value to that currently accepted value of the luminous matter in these two galaxies, the authors concluded that most of the mass of the Local Group must be dark and it is one of the earliest findings that the dark matter halos are surrounding the galaxies (Kahn & Woltjer, 1959).

In the 1970s, the first unambiguous statements start to arise that the additional mass was required in the external region of some galaxies as well as the dark matter became a well-recognized concept. In 1970, Ken Freeman made a comparison between the radiuses at the rotation curve to the peak, under the calculation of an exponential disk and fit the

rotation curve of photometric observations. This combination of radio observations and theoretical modelling stretching above the disk allowed him to come to a firming finding for the galaxy M33 and NGC 300, the observed rotation curves stroked at larger radii are much higher than the estimated (Freeman, 1970).

The first person to introduce the significance of the observed flatness of rotation curves was Morton Roberts. In 1972, he issues the rotation curve of the galaxy M31 extended up to 120 arc minutes from the center of galactic, together with R. Whitehurst (Whitehurst & Roberts, 1972). In 1973, he further the rotation curve analysis to the galaxies M81 and M101, he disputes these spiral galaxies illustrated flat rotation curves in their external region of the galaxy (Roberts & Rots, 1973). The authors interpret the large radii of these three galaxies rotation curve to signify a huge mass at larger distances, the evidence for dark matter in these three galaxies developed higher.

In 1978, the results from Albert Bosma PhD thesis included the radio observation of the velocity fields and the relevant rotation curves of 25 galaxies. This research finding convincingly proved that most of the galaxies had flat rotation curves out to the largest observed radius, and again the observations were exceeded the optical size of the galaxies, hence illustrating the mass carries on to rise above the area accounted by the gas and stars. Albert Bosma concluded that the mass composition of the baryonic components cannot signify the observed profiles (Albert Bosma, 1981).

A few months later, Rubin, Ford and Norbert Thonnard published the optical rotation curves of ten high luminosity spiral galaxies and found that they were flat out to the outermost measured radius. This research finding had become one of the most well-known and widely cited in the dark matter literature history. In 1980, Vera Rubin and Kent Ford show the observations of a set of spiral galaxies that the orbital velocities of stars in galaxies were unexpectedly high at the external region of the galaxy (Rubin et al.,

1980). This unexpected result illustrated that the difference in the luminous mass with the distance from the central region of the galaxy is balanced by an increase in non-luminous mass. Although initially met with skepticism, but Rubin's result of the proven of dark matter became scientifically accepted after the subsequent decades by researching more than 200 galaxies and huge documented data show that the universe was virtually 90 percent undiscovered matter (Tank, 2015).

This section concludes with a general overview of some great astronomers' efforts on dark matter research and findings. This history was significantly important because it gave the first dynamical evidence for matter in the local Universe beyond the visible stars. Until today, these findings are still very significant, as the future for identifying the dark matter and the observations continuously grow widely and the research is significantly extended further by the astronomers today.

2.2 Spiral Galaxy

In 1925, the pioneer study of the Galaxy rotation and the spiral arms formation was initiated by Bertil Lindblad. He found the permanently of stars in a spiral shape arrangement was unjustified. Since the angular speed of the galactic disk rotation is varies with the distance from the center of the galaxy, a radial arm would become curved as the galaxy rotates. After some rotations, the arm would eventually increasingly curved and the wind around the galaxy would become closer. Although the measurement reveals that the rotational velocity of the stars in the spiral galaxies with corresponding to its distance from the center of the galaxy is assuredly higher than the estimated from the Newtonian dynamics, however, it still could not illustrate the solidity of the spiral structure (Lindblad, 1925).

Spiral galaxies classified as a type of galaxy were originally primitive determined by Edwin Hubble in 1936 and subsequently the Hubble sequence part was formed. Most of

the spiral galaxy is made up of few distinct elements, such as a center stellar bulge of mainly older stars, a supermassive black hole at the central of the bulge, a bar-shaped distribution of stars, a spiral arms which composed of a flat, rotating disk of stars and interstellar matter and a near-spherical dark matter halo. These different components are varying from galaxy to galaxy which will cause a difference in terms of luminosity, mass and size of a spiral galaxy. The flat rotating disk of a spiral galaxy usually contains stars, gas and dust. Although the stars and other luminosity components accommodate in a galaxy majority situate on a plane, however, most of the mass in a spiral galaxy is retained by a spherical halo of dark matter, as illustrated by the universal rotation curve concept (Williams et al., 2009).

Spiral galaxies resemble spiraling pinwheels and they are named by their spiral structure characteristic which stretches from the galactic central until the galactic disc (Hubble, 1934). This region of stars extends from the galactic center until the galactic disc is known as spiral arms. In the Hubble classification outline, the spiral galaxies are named as type S, continue by a letter either a, b or c. These letters demonstrate the magnitude of the center bulge and the degree of tightness of the spiral arms. A Sa type galaxy has a closely wound, poorly defined arms and huge core region. On the other hand, a Sc type galaxy has an open, well-defined arm and small core region. Furthermore, a galaxy with prominent well-defined arm is known as a grand design spiral galaxy while in opposite to a flocculent spiral galaxy which has a poor-defined arm (Bergh & Van den Bergh, 1998).

A spiral arm is the location of on-progressing stellar formation and is brighter than the encircled disk due to the young, more massive, luminous and hot stars that occupy them. As the massive star develops in more faster, their demise will grant a darker background of dimmer stellar together with a density wave (Belkora, 2002). As the spiral arms move

in their galactic orbits, they are simply able to cross through the old established stars. The space velocity of every stellar system is altered by the local higher gravitational force as the stars move along the arm. Furthermore, the newly established stars do not fix in the location within the spiral arms forever. After the stars move away from the other side of the arm, the space velocity will return to its normal value (Henbest & Couper, 1994).

In the central of galaxies, the bulge is a huge and tightly concentrated star distribution. The center collective of stars is found in many spiral galaxies, usually denoted as the overflowing of stellar light beyond the external disk light. The bulge is often encircled by a much dimmer halo of stellar, which most of them are located in the globular clusters (Hubble, 1934). The bulge of Sa type galaxies is often larger, made up of red and old Population II stars. On the other side, the bulges of Sc and SBc are smaller, made up of blue and young Population I stars (Graham & Worley, 2008). Some bulges of the spiral galaxies have higher larger in disk central and similar characteristics to the disk galaxies. While others have similar characteristics to elliptical galaxies, which have lower luminosity and mass.

Many supermassive black holes are thought to pose in the central of bulges. There are many evidences that the presence of a black hole in the centers of a spiral galaxy. This includes the active nuclei is exists in some spiral galaxies, and a large compact central mass is found in the many galaxies by using dynamical measurements. If there are observational data, certainly a supermassive black hole will be found to be located in the galaxy center. However, it is not confirmed yet whether a supermassive black hole appears in every central of the spiral galaxy or not.

About two-thirds of all spiral galaxies are observed to have an extra structure in the form of a bar-like component, it stretches from the center bulge until the part where the spiral arms (Binney et al., 1998). The ratio of barred spirals to the bar-less cousins has

transformed along with the cosmos history. Some of the bars can exist in either strong or weak. The existence of the bar in an edge-on lenticular and spiral galaxies can often be distinguished by out-of-plane X-shaped structures. This is usually has a peak insight at a half-length of the plane bar (Ciambur & Graham, 2016). Around 8 billion years to approximately a quarter 2.5 billion years ago, about 90% of the spiral galaxy contained bar-less. Until today, more than two-thirds of the spiral galaxies in the visible universe have bars (Melvin et al., 2014). The research galaxy is a barred spiral galaxy, named as M100 in Messier Catalog or designation as NGC 4321 in New General Catalog.

2.3 NGC 4321 (M100)

The very first discovery of M100 is found by Pierre Mechain on March 1781, situated in the ear of Virgo together with its apparent neighbors, M98 and M99. In April 1781, his friend, Charles Messier acquire the M100 position and include it in his third published edition catalog. During the observation, Charles Messier describe M100 as a nebula without a star and it was hard to identify the nebula due to its faintness (Cavin, 2012). William Herschel was then discovered that there was a bright cluster of stars within the nebula during his observations. In April 1832, John Herschel extended the findings with M100 observation by using better telescopes. John Herschel was able to observe a very faint, very large, round and brighter toward the middle nucleus. He also added that it is barely visible through the clouds and not a very remarkable nebula (Herschel, 2012). M100 is among the first batch of spiral galaxies that has been detected and then listed by Lord Rosse in one of the fourteen spiral nebulae early discovery to the year 1850 (Parsons, 1968). Since then, M100 have widely observed by a huge mass of researchers.

NGC 4321 is a grand design galaxy and one of the brightest galaxies located in the Virgo cluster, and situated in the southern part of the constellation Coma Berenices. M100 has an apparent magnitude of 10.1 and lies at an approximate 55 million light-years of

distance from Earth. The area of M100 cover is 7.4 by 6.3 arc minutes of apparent sky, which is similar to a linear diameter of 107000 light-years. M100 is a tilted nearly face-on galaxy as observed from Earth. M100 has been imaged extensively by using Hubble Space Telescope for observation, which leads to more than 20 Cepheid variables and a nova has been discovered (Ferrarese et al., 1996). Furthermore, there are seven supernovae have been discovered in M100 so far. The first supernovae, SN 1901B was found in March 1901 and the latest seventh supernovae, SN 2020oi was found in January 2020 (Horesh & Sfaradi, 2020).

The internal disk of M100 has been researched by Nasa Ultraviolet Imaging Telescope, and M100 is found as a starburst galaxy (Wozniak et al., 1999) with an intense star formation rate within a ring in the center galaxy along the periphery of the innermost spiral arms. M100 has a 1 kpc radius nuclear bar which attaches to two wound spiral arms (Sakamoto et al., 1995). The star formation has been happening in this nuclear bar since at least 500 million years ago. The galaxy is estimated to have 400 billion stars (Allard et al., 2006).

M100 behaves similarly to most of the spiral galaxies on the Virgo Cluster, which is lacking in terms of neutral hydrogen and hence does not illustrate signs of star formation outside of the internal disc (Koopmann & Kenney, 2004). The interactions with an intracluster medium of Virgo causes M100 to be truncated within the galaxy disk compared to the similar Hubble type of isolated spiral galaxies (Chung et al., 2009). As the galaxy moves through the Virgo Cluster, it undergoes ram pressure stripping and this process will leave it without gas.

M100 is a SAB(s) bc type galaxy with two symmetric well-defined spiral arms and some fainter ones. The arms of M100 are composed of numerous clusters of hot, young, blue stars and star-forming regions. These young blue stars in the arm are formed from

density perturbations which is due to the interactions with neighboring galaxies. About the brightness, the galaxy appears slightly asymmetric, this is because more young brighter stars are formed on the southern part of the nucleus (Elmegreen & Elmegreen, 1987).

The first inclination angle of M100 was investigated by Danver (Danver, 1942). In 1942, Danver researches a morphological investigation of some nearby galaxies including inclination angle investigation. In their calculation, the inclination angle of the galaxy M100 is 30.8°. In 1958, Holmberg (Holmberg, 1958) gives major and minor diameters of 10.0' and 9.1', respectively. With an axial ratio of the spheroid of 0.2, they indicate an inclination angle of 36°. In 1973, a third determination was performed by Van Der Kruit (Van der Kruit, 1973) using the spiral structure under the assumption that the two arms have an identical shape and are exactly 180° out of phase. This leads to $i = 37°$ and they choose to use an inclination angle of 35°. The rotation curve of Rubin (Rubin et al., 1980) implemented the inclination angle used by Van der Kruit, which is 35°.

On the other hand, the inclination angle employed by Knapen (J. H. Knapen et al., 1993) is based on The Second Reference Catalogue of Bright Galaxies (RC2) by de Vaucouleurs (1976), which is a standardized documentation file which containing information on 4364 galaxies with references to papers published between 1964 and 1975, which is 27°.

There are two reasons that the inclination angle of 27° is employed. First, Knapen's research (J. H. Knapen et al., 1993) is more updated compared to Rubin's research (Rubin et al., 1980). Second, the Second Reference Catalogue of Bright Galaxies (RC2) is a standardized documentation file which contains very huge information of 4364 galaxies, which is a more accurate data.

There are a few reasons that NGC 4321 received a huge amount of theory and observation attention. One of the reasons is it is one of the closest Virgo cluster galaxies, which means its structure could be analyzed clearly. Another reason is its bar of moderate strength contributes a raise to a clear circumnuclear structure (J. Knapen et al., 2000). The moderate inclination and relative proximity of galaxy NGC 4321 leads to a convenient research on its kinematics, distribution and content of the neutral hydrogen gas in both its molecular (CO) and atomic (HI) form (Cepa et al., 1992).

2.4 Rotation Curve

The rotation curve of a galaxy defines the galaxy rotational velocity as well as support some of the most convincing proof for the presence of dark matter halo (Tiley et al., 2019). Rotation curve analysis on a spiral galaxy is the large equipment to determine the composition of mass in a spiral galaxy. The rotation curve provides the essential knowledge for identifying the dynamics, formation and evolution of a spiral galaxy (Sofue & Rubin, 2001). The rotation curve confirms that the distribution of light observation is not matched with the distribution of the star mass in a galaxy (Persic et al., 1996). The mismatching between the distribution of light and the distribution of mass indicated that there is some “invisible” matter that contributes mass to the galaxy, the astronomers name this “invisible” matter as dark matter.

In 1914, the rotation of the galaxy was first identified by Slipher. Slipher determined the inclined absorption lines in the nuclear spectra of the Sombrero galaxy and M31 (Slipher, 1914), and in the same year, Wolf discovered the inclined lines in the nuclear spectrum of M81 (Wolf, 1914). These findings lead Pease to employ the Mt. Wilson 60-inch to do the rotation investigation of the great nebula in Andromeda with an exposure of taken over 84 hours in 1916 and a major axis spectrum of 79 hours taken in 1917. The absorption lines only stretched until radius 1.5 arc minutes, which is less than 2% of the

optical radius and it was very adequate to illustrate the steepness of a rise in the velocity (Pease, 1918).

Some years later, M31 rotation studies by Babcock in 1939 (Babcock, 1939) and Mayall in 1951 (Mayall, 1951) have extended major axis rotation velocities to almost 2° from the center nucleus, but the spectrographs had stability problems due to the exposure times were only ten hours. Interestingly, both M31 rotational velocity from Babcock and Humason unpublished rotational velocity for the galaxy NGC 3115 illustrated the last measured point is having a velocity of more than 400 kms^{-1}, which is almost twice larger than the usual and subsequently rise the question of mass composition (Sofue & Rubin, 2001).

At the McDonald Observatory in 1939, Oort found the mass distribution in the galaxy NGC 3115 shows to be mostly no connection to that light (J. H. Oort, 1940). The ratio of the mass density to the light density in the external region of the nebula is indicated to be a very large number and this finding is applicable for whatever dynamical model. Since the ratio did not larger than 1 and only can occupy roughly 50% of the mass, hence the remainder must compose of either extremely faint dwarfs having a ratio of mass to light about 200 to 1 or else is dust and interstellar gas. Later on in 1954, Schwarzschild reanalysis the velocity dispersion for M31 and confirmed that the flat rotation curve was in disagreement with the hypothesis of the same light and mass distribution (Schwarzschild, 1954).

An optical observational program of rotational velocity to identify the kinematics and hence the masses of the spiral galaxies were adopted by Page in 1952 (Page, 1952) and especially Margaret in 1960. Margaret and Geoffrey Burbidge reproducing the technology adopted by Pease in 1918 but with the improvements of larger telescopes, faster spectrographs and the new red sensitivity of photographic plates to observe the NII

and Hα emission lines which emerge from the HII region within the spiral disks (Burbidge & Burbidge, 1960). In the time of a decade, the rotation curves appeared for some dozens of galaxies and many galaxies is expanding only over the initial and turnover velocity.

The early galaxy observations are surveys by de Vaucouleurs (De Vaucouleurs, 1959) and the galactic dynamics by Lindblad (Lindblad, 1925) show the growth of the observations and the explanation of the spiral kinematics. In the 1970s, the flat rotation curves were constantly detected by Rogstad and Shostak (Rogstad & Shostak, 1972), however, the concern about the sidebands still existed, the possible explanation of these incidents are there is a variation in the mass to luminous across the galactic disk (Roberts & Rots, 1973). These findings are historically remarkable because this records the early findings, which most of them have faded into oblivion.

By 1970, Rubin & Ford deliver the results of the rotation curve on the galaxy M31, composed of the velocity from 67 HII regions, the results show that the mass keeps on raise up to the last measure of the region, which is 24 kpc (Rubin & Ford Jr, 1970). A few years later in 1978, Rubin and other researchers had studied that the rotation curves of high luminosity spiral galaxies are flat, at a radius as far as 50 kpc (Rubin et al., 1978). The first flat HI rotation curves were identified by applying a single dish telescope (Roberts & Rots, 1973). However, a few years later, the observers and the theorist recognized each other's work, they collectively confirm that the disk galaxies are steep in a widen dark halos (Einasto et al., 1974; J. Ostriker et al., 1974; J. P. Ostriker & Peebles, 1973).

The higher and deeper resolution of HI observations with composite telescopes displayed the most spiral galaxies that the rotation curves remain flat above the optical disks (Begeman, 1989; Albert Bosma, 1981). The summary of a flat rotation curve is

because there is a huge dark matter halo encircling the spiral disk, which the cosmological distances are held by the Newtonian gravitational theory.

Rotation curves are a very useful tools that can serve for many reasons, which is for the kinematics of galaxies studies, evolutionary history inspection and estimated rotation curve Keplerian form to analyze the mass and composition of dark matter. The rotation curves can be determined by the emission lines, and HI, CO and Hα lines are specifically more beneficial on the mass distribution derivation in the galactic disk. This is due to the demonstration of the motion of population I interstellar gases, which is much smaller velocity dispersion compared to the rotational velocities, which is about the order of 5 to 10 kms^{-1} (Sofue & Rubin, 2001).

2.5 Neutral Hydrogen (HI)

The neutral hydrogen (HI) line is an electromagnetic radiation spectral line, which is generated during a difference that occurs in the energy state level by a neutral hydrogen atom. A hydrogen atom is made up of a positive and negative charged particle, which is proton and electron. These particles have some intrinsic angular momentum in the quantum mechanical effect, which is known as spin. When these two particles are spin in an antiparallel way, the hydrogen atom will remain in the lowest energy state level. However, the hydrogen atom has extra energy when the spins of these particles are in parallel. The interstellar hydrogen atoms in the very cold space are at the lowest energy state level. The collisions between particles in the space will make the particles receive extra energy and excite to a higher energy state level. After the hydrogen atom cools down and drop to the lowest energy state level, the atom will release electromagnetic radiation at a frequency of 1420 MHz, which is the same as a 21 cm vacuum wavelength in the outer space (Hellwig et al., 1970).

During the 1930s, a radio hiss sound was identified that keeps changing on a daily cycle and arise as an extraterrestrial in origin. Then, there were some suggestions that this was due to the Sun, consequently the observation is made and these radio waves seemed to be propagated from the galactic center. These discoveries were published by Jan Oort in the year 1940. He added on there could be possibly a significant advance in astronomy if the radio waves were the emission lines in the radio spectrum (J. Oort, 1941). The first 21 cm line of atomic hydrogen theoretically might be detectable in interstellar space was estimated by a Dutch astronomer, which is H.C. van de Hulst in the year 1945. After the World War II, the research is initially done in both Holland and United States. However, the receiver of the Dutch team was caught fire and unfortunately destroyed, delaying their work from recovering back by a few months (Van de Hulst, 1982).

The first 21 cm line was discovered in an interstellar medium by Ewen and Purcell at Harvard University in the year 1951 (Ewen & Purcell, 1951). Before publication, they confirm their discovery by collaborating with Dutch astronomers Muller and Oort, and Australian astronomers Christiansen and Hindman. After a few weeks, both groups successfully made the 21 cm line detection, which the Dutch astronomer (Muller & Oort, 1951) send their collaboration results to the Nature discovery paper with the Australian detection as a footnote. The first neutral hydrogen maps in the galaxy were produced after the year 1952, which demonstrate the spiral structure of the Milky Way for the first time. An early 21 cm line discovery history illustrates an interesting insight into how science evolved in gentle times. The original detection horn antenna by Ewen and Purcell is preserved until nowadays, and is currently exhibited at the National Radio Astronomy Observatory (NRAO) in Greenbank (Sullivan, 2012).

21 cm hydrogen line has brought advantages in the cosmology field. In cosmology, theoretically the greatest contribution of 21 cm hydrogen line is in the Big Bang

discovery. This is due to it is currently the exclusive method to probe the dark ages by using hydrogen recombination to reionization. By measuring the neutral hydrogen ionized by radiation from quasars or stars, the 21 cm hydrogen map will reveal an image of how the universe reionization occurs. Furthermore, it can illustrate an image of the power spectrum in the time after recombination by mapping the luminosity of 21 cm hydrogen radiation (Bowman, 2008). However, the 21 cm hydrogen observations in the cosmology field are very difficult. If the observations experiments are made in ground-based, the radio signal will be interrupted by the interference from the ionosphere and television transmitters. In order to eliminate the interference, the observations experiment must be made from a very secluded location. One of the proposals is to set the experiments in space-based, for example, the far side of the Moon to recompense the interference. In spite of these problems, the 21 cm hydrogen is commonly considered as the next huge frontier in cosmology observational. In the meantime, the HI distribution mapping by using current and future facilities are underway with several efforts, such as SKA, BINGO, FAST, TianLai, CHIME, HIRAX, ASKAP and MeerKAT observations experiment (Padmanabhan, 2017).

The 21 cm hydrogen line findings have brought a huge contribution to radio astronomy for last the 70 years. In radio astronomy, the 21 cm spectral line reveals in the radio spectrum. Two huge advantages of 21 cm line in radio astronomy stand out, which is can be conducted during the day and the observation can be made regardless of the weather conditions (Storey et al., 1994). Usually, the hydrogen atoms are equally allocated in the galaxy and every line of sight pass the galaxy will display a hydrogen line. These 21 cm hydrogen lines can be used to plot the rotation curve of a galaxy by determining the rotational velocity and distance of a galaxy from Earth. Besides, hydrogen line also could be applied to compute the mass of an individual galaxy and to investigate the dynamics of the galaxies.

Since the year 1951, the 21 cm of neutral hydrogen line has become one of the best partners of a human being in the investigation and understanding on the mystery of cosmology and radio astronomy. After the 21 cm line discovery, the knowledge has been expanded widely in the subsequent century. In addition, the new enhancement in instrumentation and computation from decade to decade has created the opportunity for researchers to further utilize the ability of HI line in researches. Now, 70 years after the HI line discovery, the 21 cm can be found in a lot of radio observatories and even a low cost receiving system can be assembled in the university laboratory to further the HI line achievement in cosmology and radio telescope (Storey et al., 1994).

2.6 Carbon Monoxide (CO)

In an interstellar medium, the molecular hydrogen is the most common molecule that could be discovered. After molecular hydrogen, the second most common molecule that can be found in the interstellar medium is carbon monoxide (CO). CO is much easier to detect than the hydrogen molecule. This is due to the asymmetry of CO makes this polar molecule generate brighter spectral lines than the hydrogen molecule. Although molecular hydrogen is the most general molecule in an interstellar medium, however, CO is the most common gas tracer selection as the research on the interstellar medium of galaxies. This is because the molecular hydrogen only can be identified in the ultraviolet light that required a space telescope as the ultraviolet light would be blocked by Earth's atmosphere. Furthermore, the carbon monoxide observation is given huge information about the molecular clouds, a place where most of the star formation occurs (Combes, 1991).

There is a lot of advantages by using carbon monoxide to do rotation curve analysis. The CO rotational transition range at 1.32 mm and 2.63 mm in the millimeter-wave range are very precious in studying molecular gas concentration toward the central of the galaxy

and the rotation kinematics at the internal radius of the disk (Sofue, 1997). High inclination and edge-on galaxies are especially beneficial for the rotation curve analysis. This is because CO minimizes the uncertainty that appears from inclination corrections, due to the extinction-free measurements are critical, particularly for the center rotation curve. In addition, the CO rotation curves can emerge from the contamination of the continuum stellar light and the extinction of the optical lines from central bulges. Another good point of CO spectroscopy is it contains high spatial and velocity resolution from one to several kms^{-1} by interferometric observations (Sofue & Rubin, 2001).

There are many CO observations that have been done in the galaxy NGC 4321. CO observation in the center region was done by using the Five College Radio Astronomy Observatory (J. S. Young et al., 1995). The CO (J=1-0) observations to study gas kinematics and its relation to active phenomena in the center region were done by using Nobeyama Millimeter Array (Sakamoto et al., 1995). CO observations using the Institut de Radioastronomie Millimétrique interferometer were made to interpret their relations with stellar and gaseous tracers with numerical model simulations (Garcia-Burillo et al., 1993). Sofue generated the CO rotation curves on the galaxy NGC 4321 (Sofue et al., 1999). CO observation was also used for the analysis of velocity fields, spectra and channel maps from the molecular emission by the BIMA Survey of Nearby Galaxies (Helfer et al., 2003). A CO observation focusing on the study star formation rate in the internal radius of the galaxy using ALMA was also previously done by Azeez (Azeez et al., 2016) and Ali (Ali et al., 2019).

The combination of CO in the internal region with HI in the external region is not a new concept in dark matter analysis. In Frank et al. paper, among 5 out of their 11 galaxies analysis, they added CO observed data in the internal region with HI observed data (COHI) before fitting the mass model rotation curve (Frank et al., 2016). Shelest and Lelli

took CO combined with HI for three lenticular galaxies due to the rotation curve are hard to trace for the early-type galaxies due to they are insufficient in the high densities disk as in late-type galaxies (Shelest & Lelli, 2020). In Frank et al. 2016 paper, they have combined CO in the internal region with HI in the external region before performing the rotation curve fitting. In their conclusion, they remarked that the impact of these additional changes provided significant improvement of mass modellings in selected galaxies. However, they did not extend the work on calculating the mass of dark matter. In this research, the dark matter mass will be further calculated, and the accuracy will be improved by using CO and HI. The rotation curve will be fitted separately for HI and CO observed data first then adding the dark matter mass by CO in the internal region of a galaxy with the dark matter mass by HI in the external region of a galaxy. The total dark matter mass by CO and HI is then compared with dark matter mass by HI only to calculate the accuracy improvement by using both CO and HI.

CHAPTER 3: METHODOLOGY

3.1 Mass Modelling Rotation Curve

The galaxy rotation curves are interpreted by the galaxy rotational velocity as a function of galactocentric radius. They support some of the most compelling evidence for the existence of dark matter (Tiley et al., 2019). Rotation curve analysis on the spiral galaxies is the major tool to determine the distribution of mass of different components in spiral galaxies. The rotation curve can be presented as a model which is the sum of the contribution from the stellar, dark matter and gas component (Randriamampandry & Carignan, 2014) as follow:

$$V_{rot}^2 = V_{gas}^2 + V_{star}^2 + V_{DM}^2 \tag{3.1}$$

Where V_{rot}^2 is total rotation velocity, V_{gas}^2 is gas velocity, V_{star}^2 is star velocity and V_{DM}^2 is dark matter velocity.

As mentioned in the introduction, the nonlinear fitting rotation curve method will be used in this research to compare the model with the observed data. The flow chart of nonlinear fitting rotation curve modelling is as shown in Figure 3.1:

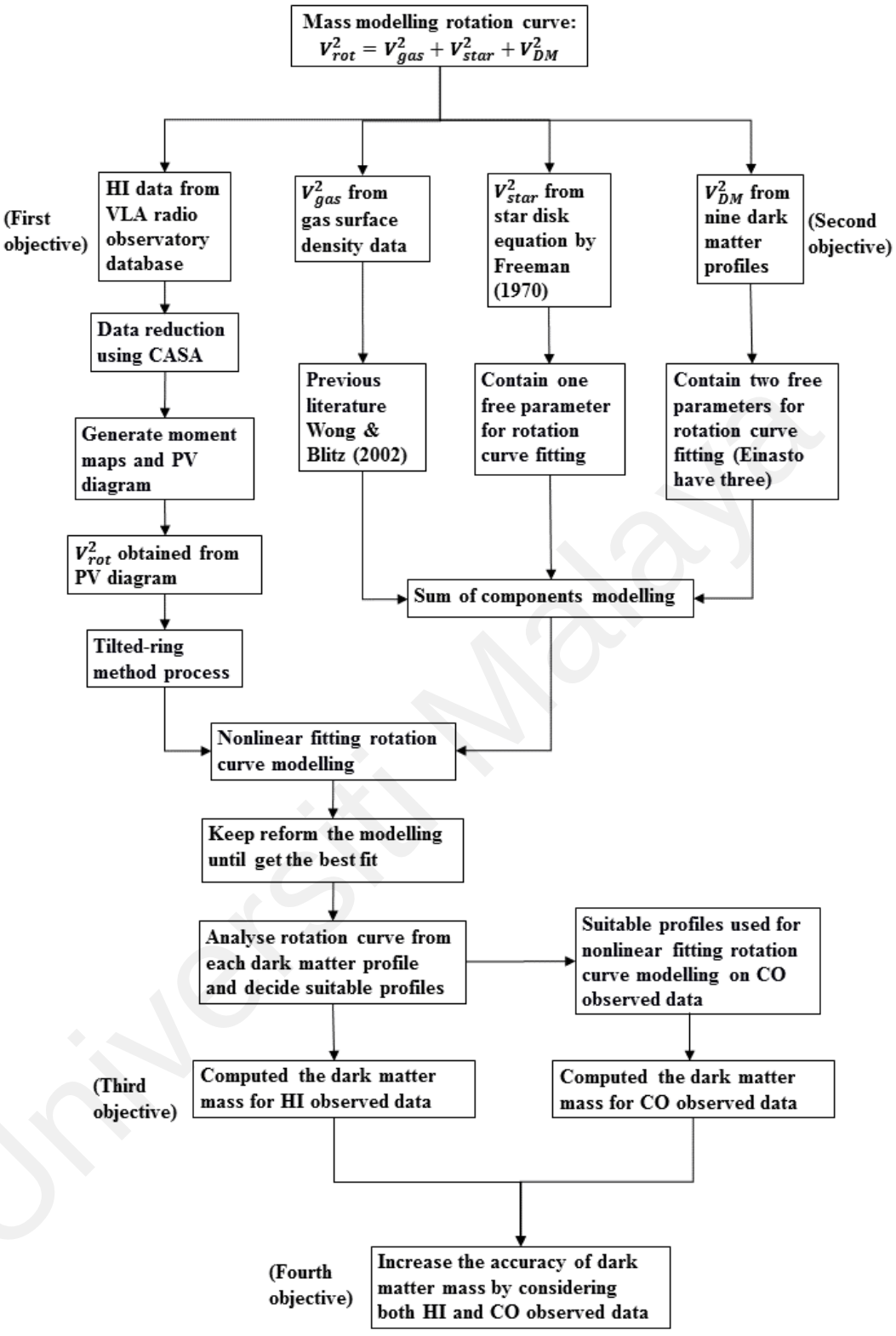

Figure 3.1: The flow chart of nonlinear fitting rotation curve modelling

3.2 HI Observed Data

The HI (neutral atomic hydrogen) observed data for the galaxy NGC 4321 is obtained from the Very Large Array (VLA) radio astronomy observatory. The Very Large Array

(VLA) is a centimeter wavelength radio astronomy observatory is located on the plains of San Agustin, central New Mexico, United States. The VLA is a facility of the National Radio Astronomy Observatory (NRAO) and it started operation in the year 1980. The VLA comprises twenty-eight 25-meter radio telescopes. Among them, 27 are operational parabolic dishes while the other one is always rotating through maintenance. Each dish can be moved independently by using the transporter along with rails path arrange in an enormous Y-shaped pattern and all instrumentation, equipment and computing power is function as an interferometer. The observation resolution of the VLA is altered by moving the positions of the dishes. The radio signals recorded by the component dishes are integrated by a computer. The computer integrated the signal to give a resolving power which a single dish can be as huge as 36 km in diameter. The maximum angular resolution of VLA is comparable with the Hubble Space Telescope at its optical wavelength (Thompson et al., 1980).

VLA has been used widely by the astronomers from all over the world. Astronomers have used the VLA for a wide variety of research programs devoted to key observations of the black hole, solar system, Milky Way Galaxy, protoplanetary disk around young stars, radio stars, radio galaxies, magnetic filaments, pulsars, atomic molecular gas, gas motion, quasars, probed the Universe cosmological parameters and provided new knowledge about the physical mechanisms that produce radio emission. In this research, the VLA archive data is obtained with the project number AS0750_D030325. The data reduction generating is processed by using CASA (Common Astronomy Software Application) software. The distance applied for this galaxy was 17.1 Mpc (Yuan & Kuo, 1998). The entire HI observational parameters on galaxy NGC 4321 are illustrated in Table 3.1.

Table 3.1: HI observational parameter on spiral galaxy on NGC 4321

Parameter	Value
Total observation time	12910 seconds
Observation date	25th March 2003
Total data recorded	855738
Total antennas used	27
Primary calibrator	1331+305
Secondary calibrator	1221+282
Configurations	D
Band	L
RA	12:22:54
Dec	+15:49:20
Position Angle	-26°
Divided channel	63
Velocity resolution	10 kms^{-1}
Primary calibrator	1331+305
Secondary calibrator	1221+282

A channel map is an image that contains only emission from within a given interval of velocities along the line of sight. Channel maps are the most common form of displaying velocity information in molecular radio observations. A "stack" of channel maps is called a "data cube", with two spatial dimensions and one velocity dimension. Since the mapping is linear, each channel map represents a “slice” through the object. While a position-velocity diagram is a slice along the line of sight, a channel map is a slice in the plane of sky to generate the position-velocity diagram. Figure 3.2 illustrates the HI velocity-channel map in the spiral galaxy NGC 4321 produced by using the Briggs weighting. The HI emission is detected in 35 channel maps with a velocity width of 10 kms^{-1} from 1406 kms^{-1} to 1746 kms^{-1}. The outcome of Figure 3.2 is comparable with the previous study (see (Azeez et al., 2016) Figure 2).

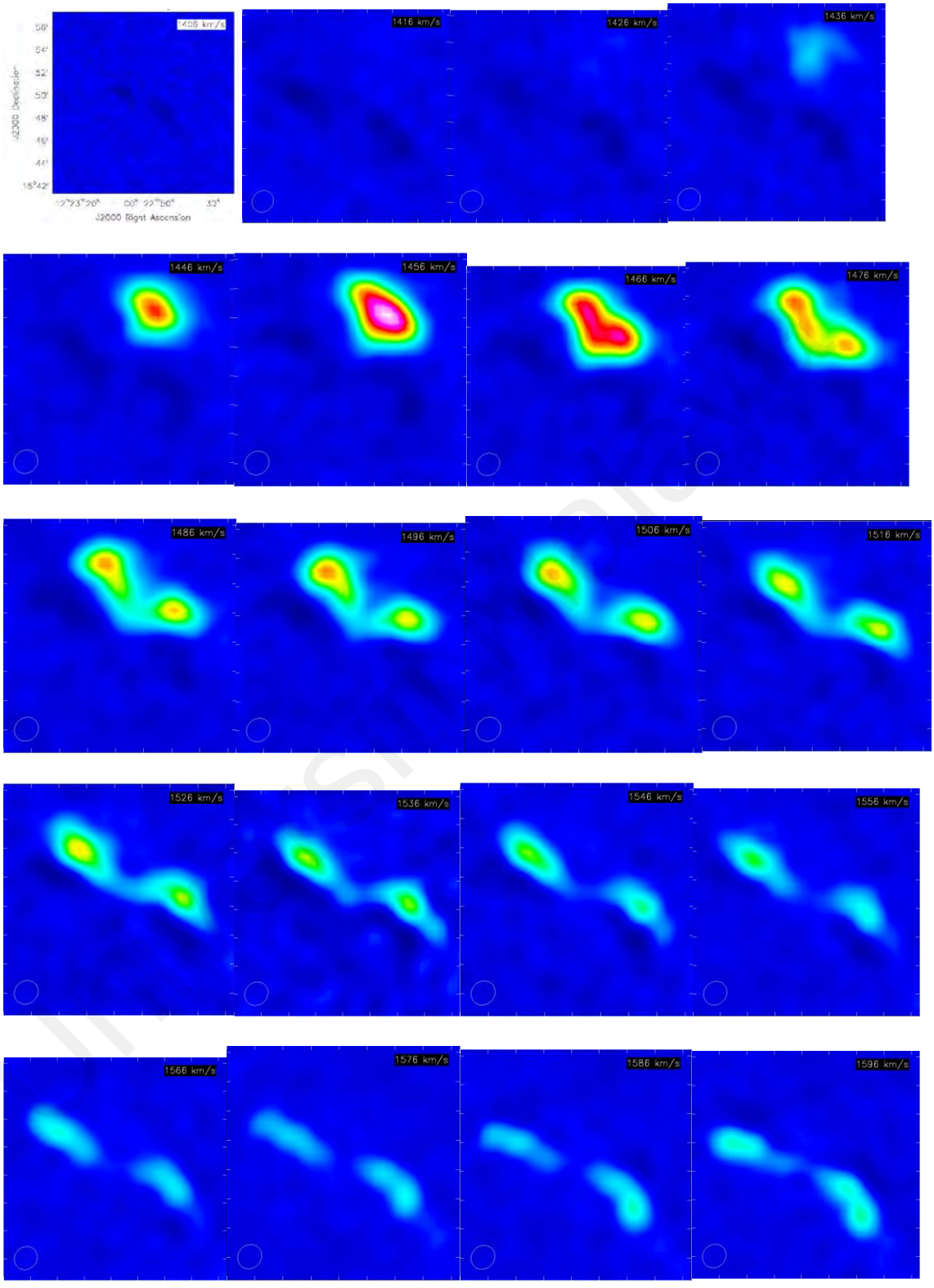

Figure 3.2: HI velocity-channel map in the spiral galaxy NGC 4321

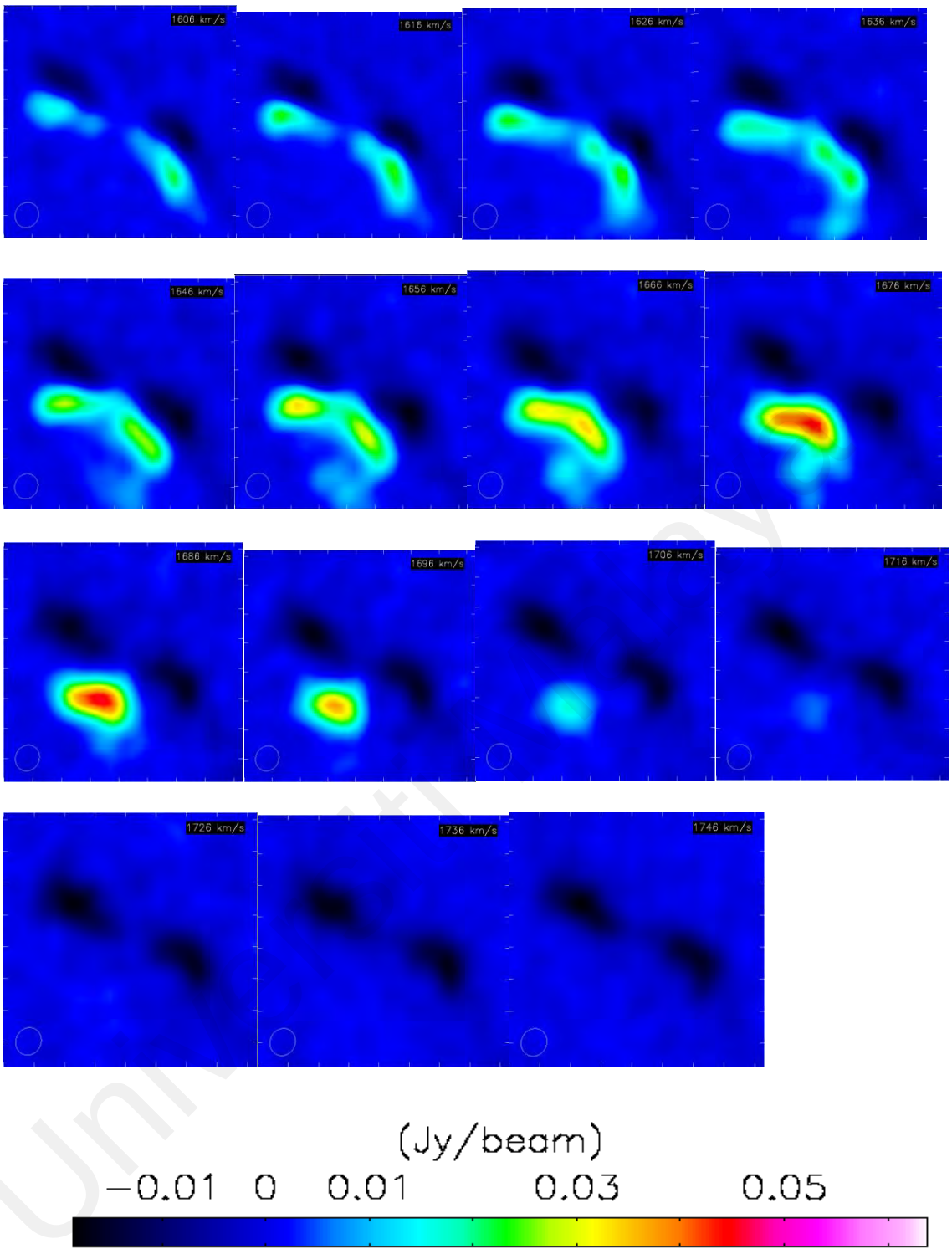

Figure 3.2, continued

3.3 CO Observed Data

HI observed data is used for all objectives, meanwhile the CO observed data only apply for third and fourth objectives. The CO (carbon monoxide) observed data for the galaxy NGC 4321 is obtained from Atacama Large Millimeter Array (ALMA) radio astronomy

observatory. The ALMA is an astronomical interferometer composed of 66 high precision dish antennas in the Atacama deserts of northern Chile. ALMA observed the electromagnetic radiation at millimeter and submillimeter wavelengths. ALMA is able to probe the Universe at millimeter and submillimeter wavelengths with unprecedented resolution and sensitivity, with a vision ten times sharper than the Hubble Space Telescope. The 66 dish antennas are arranged in different configurations, which gives ALMA a powerful variable in zoom and focus for finer details of large and dimmer objects. ALMA is an international partnership between Europe, Japan, Chile, Canada, United States, South Korea and Chile. There are a lot of contributions have been made by ALMA, such as providing insight on star birth, detailed imaging of building blocks of the star, planet formation, protoplanetary disks, planetary systems, distant galaxies, dark matter, detection of complex organic molecules, molecular gas and dust (Wootten & Thompson, 2009).

In this research, the rotational transitions of CO (J=1-0) are obtained from the ALMA science verification calibrated data. ALMA consists of 10 bands and each band provided a different frequency range. For the galaxy NGC 4321, Band 3 (frequency range 84 – 116 GHz) receiver is used for the observation. The emission was mapped with the 12 m array, 7 m array, and Total Power (TP). Each array acts as different function. The 12 m main array stimulates a maximum resolution that is even higher than the Hubble space telescope's resolution on visible wavelengths, while the 7 m array and Total Power both from Atacama Compact Array (ACA) are used to concentrate on a smaller area without interfering with each other and measure the absolute glow of the objects observed that cannot be measured with an interferometer. More detailed information for each array used on NGC 4321 data observation is as shown in Table 3.2.

Table 3.2: CO observational parameter of ALMA on galaxy NGC 4321

Array	12m array	7m array	Total Power
Observed started date	10th August 2011	17th March 2013	01st July 2014
Observed ended date	10th September 2011	11th May 2013	01st July 2014
Total time observed (s)	2.68e+06	4.75e+06	2610.82 seconds
Total antennas used	22 (out of 50)	10 (out of 12)	3 (out of 10)
Total data recorded	273441	177120	24456
RA	12:22:54.6	12:22:54.3	12:22:54.4
Dec	+15:48:56.5	+15:48:51.4	+15.48.50.6

The data reduction for inspection, flagging, calibration, combination of 12 m + 7 m + TP, imaging, feathering and making moment maps are also processed using CASA. Figure 3.3 illustrates the CO velocity-channel map of CO in the spiral galaxy NGC 4321 with restoring beam of 3.87″ × 2.53″. The CO emission is detected in 22 channel maps with a velocity width of 10 kms^{-1} from 1470 kms^{-1} to 1680 kms^{-1}. The outcome of Figure 2 is comparable with a previous similar study (see (Ali et al., 2019) Figure 1).

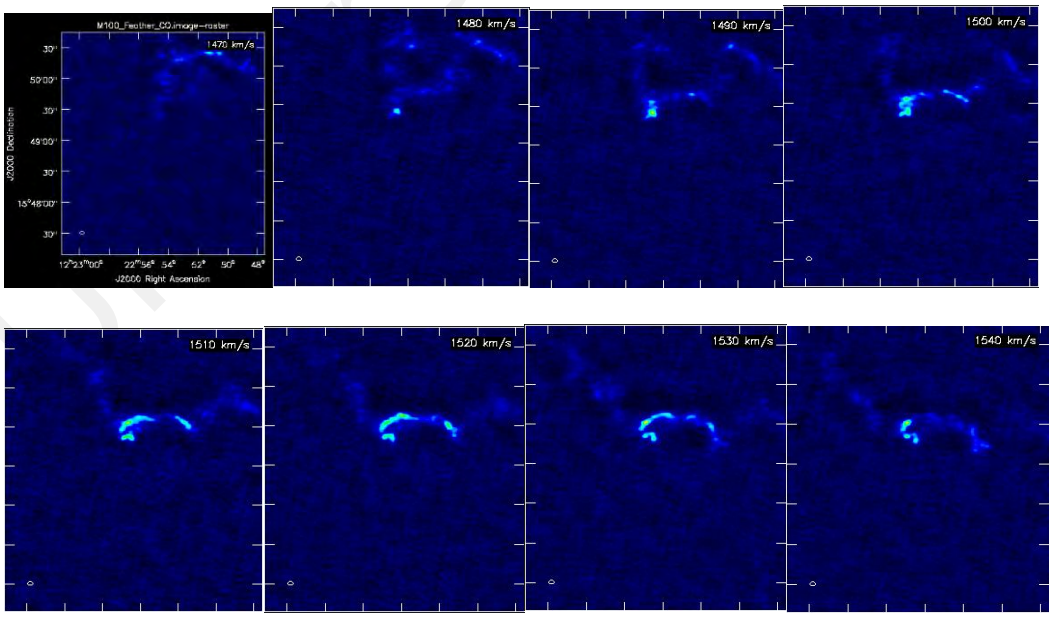

Figure 3.3: CO velocity-channel map in the spiral galaxy NGC 4321

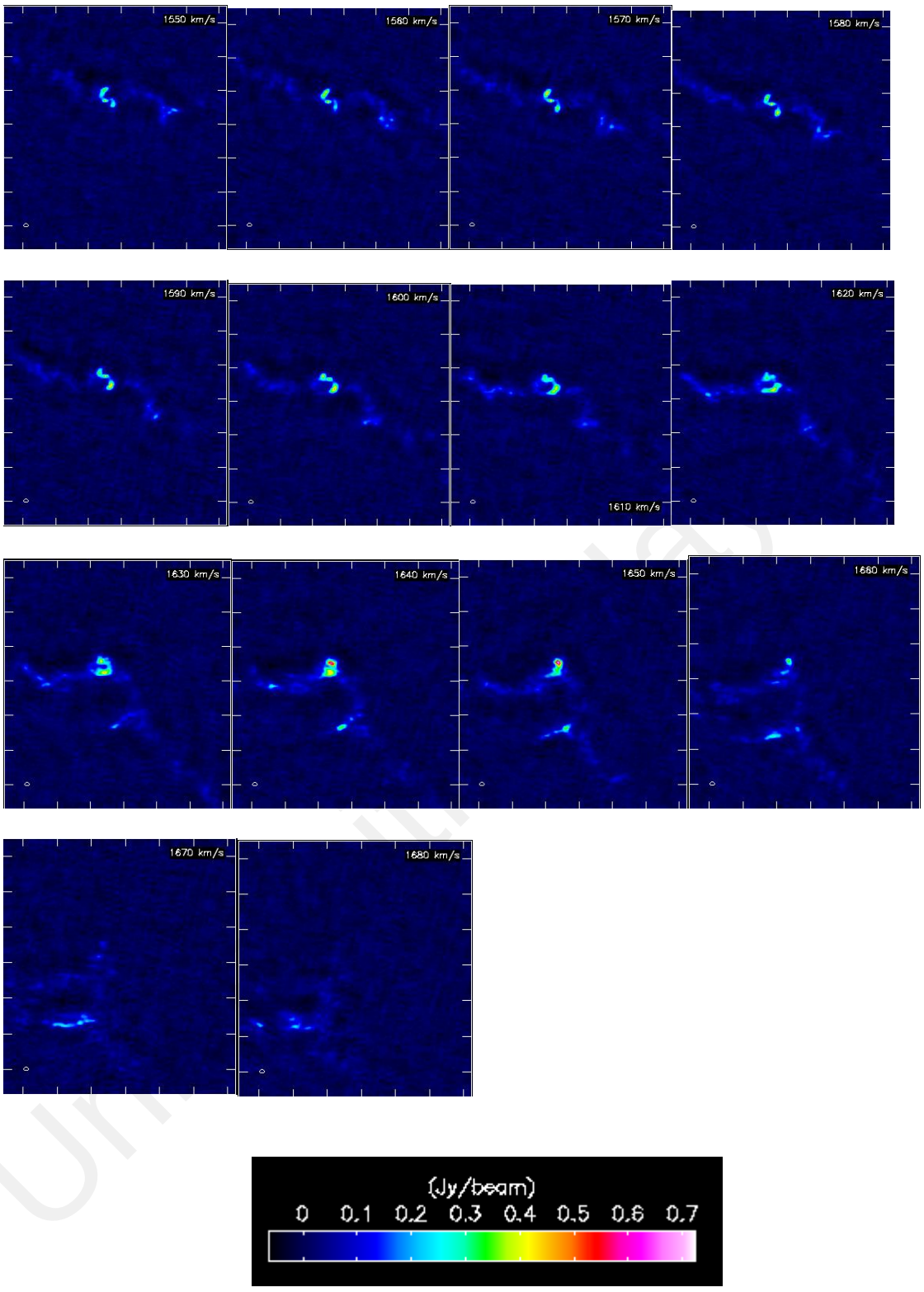

Figure 3.3, continued.

3.4 HI & CO moment maps and PV diagram

Moment maps refer to collapsing an axis (the moment axis) to one pixel and setting the value of that pixel (for all of the other non-collapsed axes) to something computed

from the data values along the moment axis. For example, take an RA-DEC-Velocity cube, collapse the velocity axis by computing the mean intensity at each RA-DEC pixel. This function offers many different moments and a variety of automatic methods to compute them.

The HI and CO channel maps from Figure 3.2 and Figure 3.3 respectively are then used as input to generate the integrated intensity moment map zero (mom0), mean velocity moment map one (mom1) and PV diagram. The CO color scale map will be overlaid with HI contours of integrated intensity (mom0), which is as displayed in Figure 3.4. For mom1 and PV diagram, the HI with CO is not overlaid as both contour line does not illustrate any useful shape. The color scale map with overlaid contours of HI will be independent with CO for mean velocity (mom1) and PV diagram, as shown in Figure 3.5 and Figure 3.6 respectively.

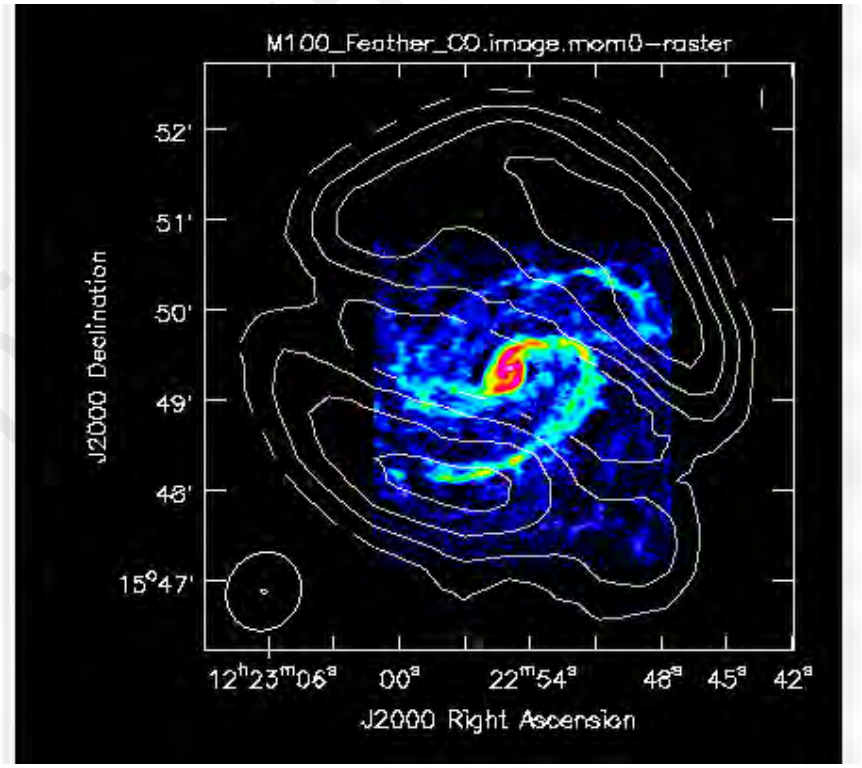

Figure 3.4: Integrated Intensity (mom0) map of HI contour overlaid with CO color scale map of NGC 4321. For HI of mom0, the color scale ranges 0 to 45 Jy/beam.km/s and for CO of mom0, the contour levels are plotted at the value of 0.4164, 0.7858, 1.155 and 1.525 Jy/beam.km/s.

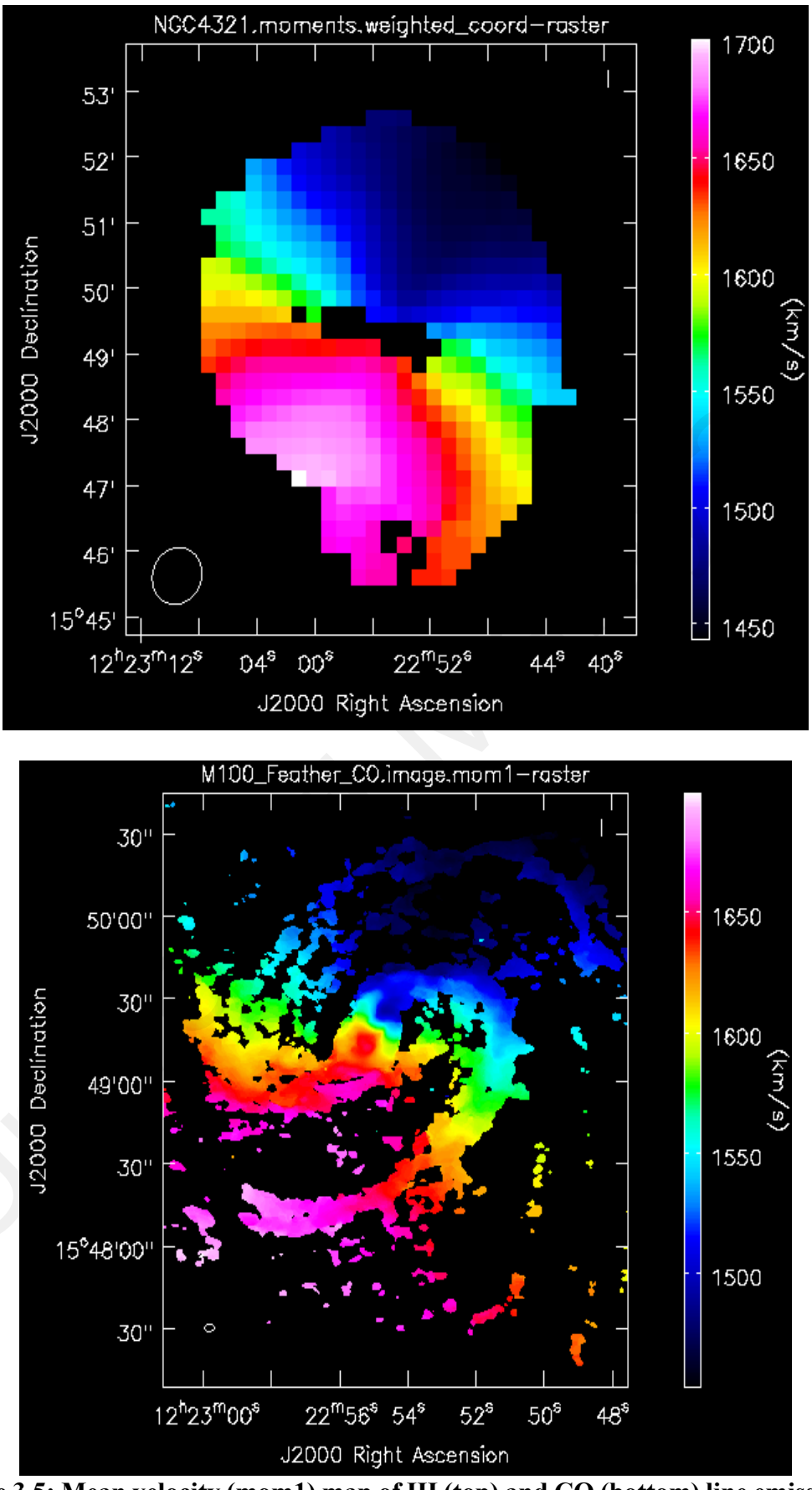

Figure 3.5: Mean velocity (mom1) map of HI (top) and CO (bottom) line emission of NGC 4321. For HI mom1, the color scale ranges from 1450 to 1700 km/s and the contour levels are plotted at the value of 1495, 1546, 1598 and 1649 km/s. For CO mom1, the color scale ranges from 1450 to 1700 km/s and the contour levels are plotted at the value of 1502, 1552, 1601 and 1651 km/s.

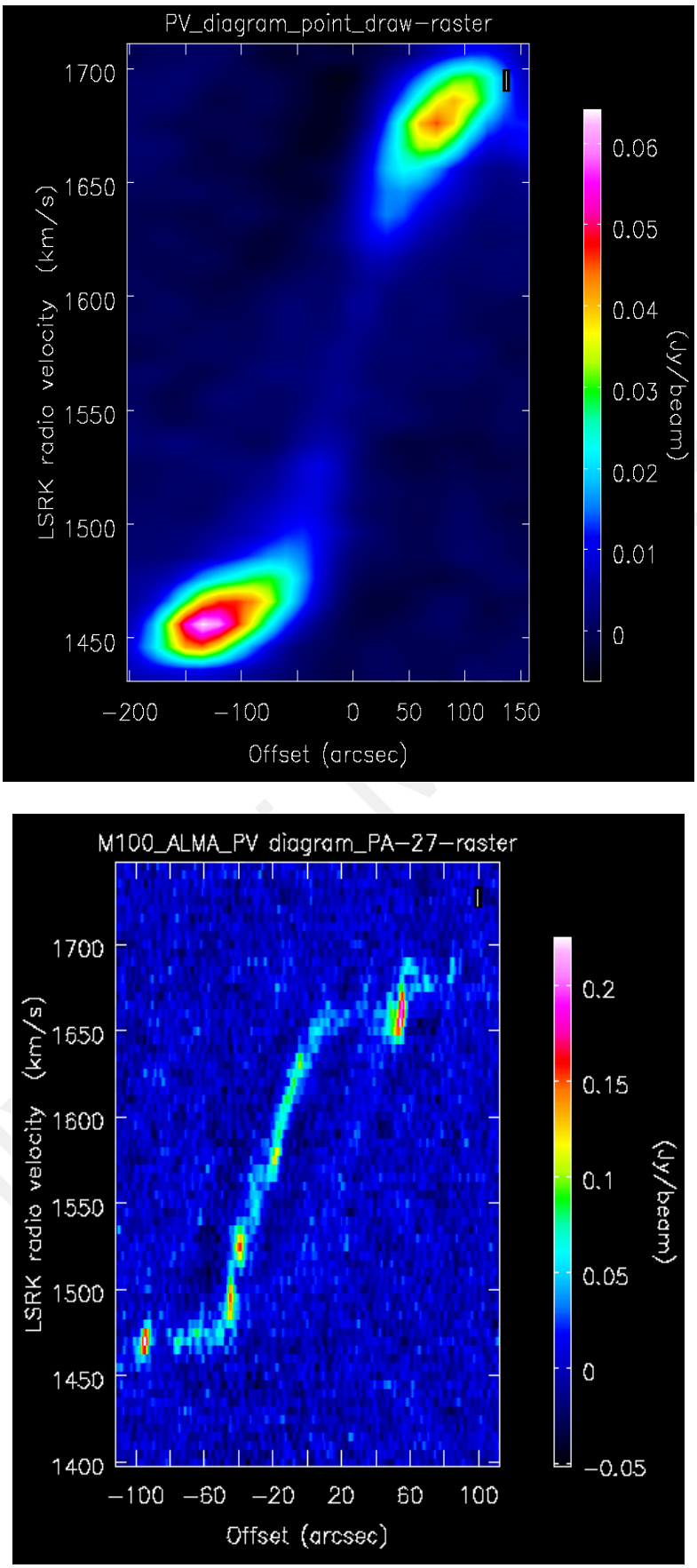

Figure 3.6: PV (Position-Velocity) diagram of HI (top) and CO (bottom) in NGC 4321. For HI PV diagram, the color scale ranges from 0 to 0.06 Jy/beam and the contour levels are plotted at the value of 0.0129, 0.0257, 0.0386 and 0.0514 Jy/beam. For CO PV diagram, the color scale ranges from -0.05 to 0.20 Jy/beam and the contour levels are plotted at the value of -0.045, 0.045, 0.09, 0.135 and 0.18 Jy/beam.

By referring to Figure 3.6 PV diagram, there is a lack of HI distribution in the center area of the spiral galaxy NGC 4321 but its distribution extended until 200 arcsec. In contrast to HI, the CO distribution is covered well in the center area of the spiral galaxy NGC 4321 but its distribution only extended until 100 arcsec.

3.5 Data Processing by Using Tilted-Ring Method

HI and CO observed velocity in Figure 3.6 is then used to acquire the rotation velocity by applying the tilted-ring method (Begeman, 1989), as below:

$$V_r(r,\theta) = V_{obs}(r,\theta) - V_{sys} = V_{rot}(r)\cos\theta\sin i \quad (3.2)$$

Where $V_r(r,\theta)$ is the radial velocity, $V_{obs}(r,\theta)$ is the observed radial velocity, r is the radius of galaxy, θ is the azimuth angle. V_{sys}, $V_{rot}(r)$ and i are the systemic velocity, rotation velocity and inclination angle of the galaxy respectively.

The functional shape of $V_r(r,\theta)/V_r(r,0)$ is against the position angle on the sky. In this case, $V_r(r,0)$ is the maximum value of V_r along the chosen ring (Oikawa & Sofue, 2014). For $\theta = 0$, $V_{rot} = V_r(r,0)/\cos 0 \sin i$, where $V_r(r,0) = V_{obs}(r,0) - V_{sys}$. The systemic velocity and inclination angle adopted for the galaxy NGC 4321 is 1575 kms^{-1} (J. Knapen et al., 2000) and 27° (J. H. Knapen et al., 1993) respectively. Since the error of systemic velocity from the original study by Knapen (J. Knapen et al., 2000) and the latest study by Ali (Ali et al., 2019) both is zero, so the error of observed velocity minus systemic velocity ($V_{obs} - V_{sys}$) is the same with the error of observed velocity (V_{obs}). Furthermore, $\sin i$ do not provide any error, hence the error of rotation velocity (V_{rot}) is the same with the error of observed velocity (V_{obs}) too in Table 3.3 and Table 3.4. The complete rotation velocity calculation of galaxy NGC 4321 by using HI and CO observed data is as shown in Table 3.3 and Table 3.4 respectively.

Table 3.3: The radius, observed velocity, radial velocity and rotation velocity of the galaxy NGC 4321 (M100) calculation by using HI observed data

Radius, r (kpc)	V_{obs} (kms^{-1})	$V_{obs} - V_{sys}$ (kms^{-1})	$V_{rot} = ((V_{obs} - V_{sys})/\sin i)$ (kms^{-1})
0.41	1603.5 ± 6.95	28.50 ± 6.95	65.04 ± 6.95
0.83	1614.27 ± 7.61	39.27 ± 7.61	89.62 ± 7.61
1.24	1622.81 ± 9.69	47.81 ± 9.69	109.11 ± 9.69
1.66	1631.35 ± 5.79	56.35 ± 5.79	128.60 ± 5.79
2.07	1637.49 ± 4.71	62.49 ± 4.71	142.62 ± 4.71
2.49	1643.8 ± 5.02	68.80 ± 5.02	157.02 ± 5.02
2.90	1649.00 ± 6.70	74.00 ± 6.70	168.89 ± 6.70
3.31	1652.71 ± 6.32	77.71 ± 6.32	177.35 ± 6.32
3.73	1656.42 ± 8.74	81.42 ± 8.74	185.82 ± 8.74
4.14	1660.5 ± 7.02	85.50 ± 7.02	195.13 ± 7.02
4.56	1664.96 ± 6.32	89.96 ± 6.32	205.31 ± 6.32
4.97	1668.3 ± 6.40	93.30 ± 6.40	212.93 ± 6.40
5.39	1671.27 ± 4.80	96.27 ± 4.80	219.71 ± 4.80
5.80	1674.24 ± 8.71	99.24 ± 8.71	226.49 ± 8.71
6.21	1675.73 ± 4.29	100.73 ± 4.29	229.89 ± 4.29
6.63	1678.33 ± 3.49	103.33 ± 3.49	235.82 ± 3.49
7.04	1679.81 ± 3.08	104.81 ± 3.08	239.20 ± 3.08
7.46	1681.66 ± 7.67	106.66 ± 7.67	243.42 ± 7.67
7.87	1684.71 ± 2.04	109.71 ± 2.04	250.39 ± 2.04
8.29	1686.55 ± 3.37	111.55 ± 3.37	254.58 ± 3.37

Table 3.3, continued

Radius, r (kpc)	$V_{obs}\ (kms^{-1})$	$V_{obs} - V_{sys}\ (kms^{-1})$	$V_{rot} = ((V_{obs} - V_{sys})/\sin i)\ (kms^{-1})$
8.70	1688.38 ± 3.97	113.38 ± 3.97	258.76 ± 3.97
9.11	1690.21 ± 4.29	115.21 ± 4.29	262.94 ± 4.29
9.53	1691.44 ± 3.21	116.44 ± 3.21	265.75 ± 3.21
9.94	1693.27 ± 3.68	118.27 ± 3.68	269.92 ± 3.68

Table 3.4: The radius, observed velocity, radial velocity and rotation velocity of the galaxy NGC 4321 (M100) calculation by using CO observed data

Radius, r (kpc)	$V_{obs}\ (kms^{-1})$	$V_{obs} - V_{sys}\ (kms^{-1})$	$V_{rot} = ((V_{obs} - V_{sys})/\sin i)\ (kms^{-1})$
0.41	1650.54 ± 2.56	75.54 ± 2.56	166.47 ± 2.56
0.83	1654.48 ± 3.00	79.48 ± 3.00	175.15 ± 3.00
1.24	1660.00 ± 2.81	85.00 ± 2.81	187.32 ± 2.81
1.66	1660.79 ± 2.37	85.79 ± 2.37	189.06 ± 2.37
2.07	1661.58 ± 2.62	86.58 ± 2.62	190.80 ± 2.62
2.49	1662.36 ± 2.51	87.36 ± 2.51	192.52 ± 2.51
2.90	1663.15 ± 2.04	88.15 ± 2.04	194.26 ± 2.04
3.31	1666.31 ± 1.30	91.31 ± 1.30	201.22 ± 1.30
3.73	1668.67 ± 1.39	93.67 ± 1.39	206.42 ± 1.39
4.14	1671.28 ± 1.77	96.28 ± 1.77	212.17 ± 1.77
4.56	1672.61 ± 1.45	97.61 ± 1.45	215.11 ± 1.45
4.97	1674.19 ± 2.02	99.19 ± 2.02	218.59 ± 2.02
5.39	1674.98 ± 2.83	99.98 ± 2.83	220.33 ± 2.83
5.80	1677.34 ± 1.19	102.34 ± 1.19	225.53 ± 1.19
6.21	1677.34 ± 1.19	102.34 ± 1.19	225.53 ± 1.19
6.63	1679.71 ± 1.98	104.71 ± 1.98	230.75 ± 1.98

Table 3.4, continued

7.04	1680.49 ± 4.14	105.49 ± 4.14	232.47 ± 4.14

In Table 3.3 and 3.4, the maximum radius obtained by HI and CO observed data are 10 kpc and 7 kpc radius respectively.

3.6 HI & CO Rotation Curve Comparison with Previous Studies

The HI rotation curve is then compared with Rubin (Rubin et al., 1980) and Knapen (J. H. Knapen et al., 1993) rotation curves and the CO rotation curve is compared with Ali (Ali et al., 2019) rotation curve.

For Rubin rotation curve, they did provide the rotation velocities in their publication. For Knapen and Ali rotation curves, they did not include the rotation velocities in their publication, hence the rotation velocity is traced from the figures in their publication. All units in the mentioned publication will be standardized with this research. The HI total rotation velocity comparison between Rubin, Knapen and this research rotation curve is as presented in Figure 3.7. Meanwhile, the CO rotation velocity comparison between Ali and this research rotation curve is as shown in Figure 3.8.

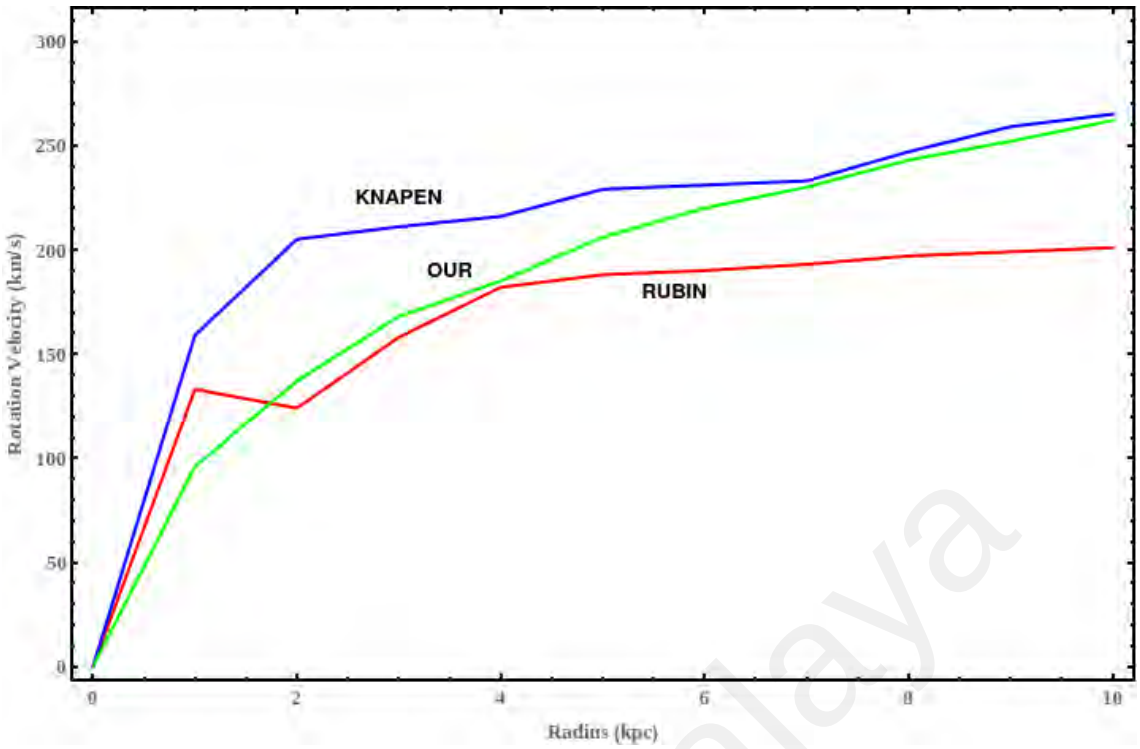

Figure 3.7: The total rotation velocity comparison between Rubin, Knapen and this research rotation curve.

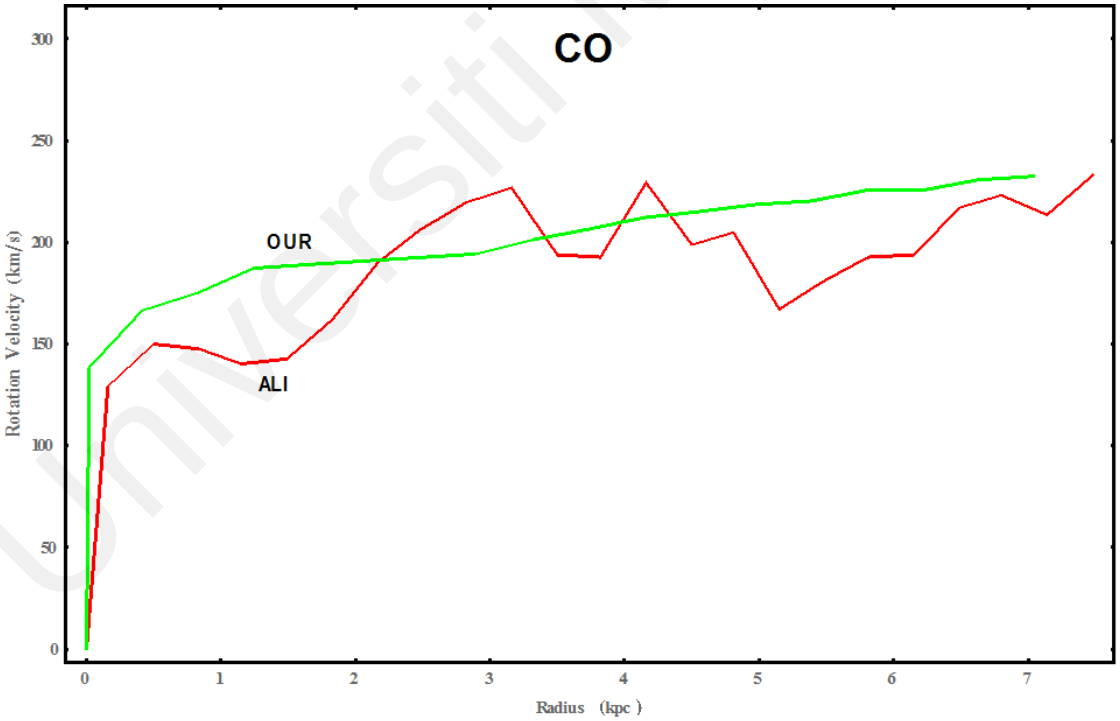

Figure 3.8: The CO rotation velocity comparison between Ali and this research rotation curve.

By referring to Figure 3.7, Rubin rotation curve has a big difference between Knapen and this research rotation curves. This difference comes from the different instruments used, also the position angle, inclination angle and systemic velocity employed. The parameters comparison is demonstrated in Table 3.5.

Table 3.5: The comparison of parameter adopted between Rubin et al, Knapen et al. and in this research

Parameter	Rubin et al.	Knapen et al.	This research
Systemic velocity (kms^{-1})	1545	1570.8	1575
Position angle (°)	140	153	-26 (same as 154)
Inclination angle (°)	35	27	27

The rotation curve of Vera Rubin was observed in the HII regions emission from the Kitt Peak 4 m RC spectrograph in 1978 (Rubin et al., 1980). While the rotation curve of Knapen and this research were observed in the 21 cm line of neutral hydrogen with Very Large Array (VLA) in 1990 and 2003, respectively. In Table 3.5, different position angles applied in the galaxy will generate a different Position-Velocity diagram. Furthermore, different systemic velocities and inclination angles applied in the galaxy will generate different rotation velocity measurements. The reason is due to the tilted ring equation including both systemic velocity and inclination angle consideration.

Apart from that, Knapen uses a different measurement technique with this research. They generated the velocity-channel maps by a resolution of 12.7”x 13.3” uniform weighting and 31.75”x 28.75” natural weighting (J. H. Knapen et al., 1993). However, the images of this research are generated with a resolution of 52.95”x 47.66” Briggs weighting. Natural weighting weighs all visibilities equally and produces a maximum point-source sensitivity in the images. However, this weighting provides a poorly

synthesized beam-shape and side-lobe levels. The uniform weighting produces a better resolution but lowers the sensitivity of the image (Vafaei Sadr et al., 2019). Both natural and uniform weighting have weaknesses, but Briggs weighting is able to overcome these negative sides. Briggs weighting creates a PSF that smoothly varies between natural and uniform weighting based on the signal-to-noise ratio of the measurements and a tunable parameter that defines a noise threshold (Briggs, 1995), which produced a better image. In addition, Knapen publication stated that their rotation velocity raises sharply in the central area. This is mainly due to their curve was determined by a high full width at half maximum within a beam of half-power width, which contribute to a sharply raising in a central area (J. H. Knapen et al., 1993). Starting from 2 kpc radius (0.4 arcmin), the sharply raising rotation velocity slowed down and after 6 kpc radius, the rotation velocity of Knapen is comparable with this research.

The CO rotation velocity of Ali and this research rotation curve is obtained from the same data source, which is ALMA science verification (SV) data. The difference between Ali and this research rotation curve obtained is due to different software and parameter used during data reduction. Both data reduction using same software Common Astronomy Software Application (CASA) for channel maps and moment maps. For rotation curve derivation, Ali derives with 3D code Barolo while this research is derived with CASA software. During rotation curve derivation, the systemic velocity employed for Ali and this research rotation curve are the same. However, the position angle and inclination angle applied by Ali and us are using a different method. For position angle and inclination angle, Ali fit these two parameters in the CO cube map and generated the Position Velocity diagram. On the other hand, these two parameters are obtained by using the same method for the HI rotation curve, which fixes these two parameters as the same value as the parameter obtain for the HI rotation curve. Furthermore, Ali mentioned that the galaxy shows a linear rotation velocity increase at the internal most central regions

and becomes nearly constant in the external regions. This is very similar to this research rotation curve. In Figure 3.8, both rotation velocity shows a linear increase until 0.5 kpc radius. After 0.5 kpc radius, Ali rotation curve demonstrates the rotation velocity decreasing then increasing and this process repeated two times before external region 7 kpc radius. Meanwhile, the rotation curve of this research illustrates the rotation velocity increase steadily and consistently after 0.5 kpc radius and becomes nearly persistent in the external regions. In a nutshell, although Ali and this research rotation curve have a difference in trend but have the same in overall, which is increase linearly at the internal most central regions and becomes nearly constant in the external region.

3.7 Dark Matter Profiles

Astronomers extend the dark matter researches into a huge theoretical framework in order to construct better methods to reveal its appearance (Millar, 2014). After this, a large number of dark matter halo models has been generated by many researchers.

3.7.1 Pseudoisothermal Profile

Pseudoisothermal profile is a singular density profile that approaches a power law at the central and the mass distribution for larger radii would diverge proportional to the radius. The density, mass and velocity equation of the Pseudoisothermal model (Jimenez et al., 2003):

$$\rho_{Iso}(r) = \frac{\rho_s}{1+(r/r_s)^2} \tag{3.3}$$

$$M_{Iso}(r) = 4\pi\rho_s r_s^2 \left(r - r_s \tan^{-1}\left(\frac{r}{r_s}\right)\right) \tag{3.4}$$

$$V_{Iso}^2(r) = 4\pi G\rho_s r_s^2 \left(1 - \frac{r_s}{r}\tan^{-1}\left(\frac{r}{r_s}\right)\right) \tag{3.5}$$

Where parameter *G* is the universal gravitational constant, ρ_s is the scale density, r_s is the scale radius and *r* is the radius from the center of the galaxy. These few parameters are the same for the following dark matter halo models besides Einasto and DC14 models, so these few parameters will not defined for other halo models.

3.7.2 Burkert Profile

Burkert profile modifies the density law of Pseudoisothermal profile in the central area of the galaxy. The mass profile for larger radii diverges logarithmically with increasing radius (Burkert, 1995). The density (Burkert, 1995), mass (Salucci & Burkert, 2000) and velocity equation (Hashim et al., 2015) of the Burkert model:

$$\rho_{Bur}(r) = \frac{\rho_s {r_s}^3}{(r+r_s)(r^2+r_s^2)} \tag{3.6}$$

$$M_{Bur}(r) = 6.4\rho_s r_s^3 \left[\ln\left(1+\frac{r}{r_s}\right) - \tan^{-1}\left(\frac{r}{r_s}\right) + \frac{1}{2}\ln\left(1+\left(\frac{r}{r_s}\right)^2\right)\right] \tag{3.7}$$

$$V_{Bur}^2(r) = \frac{6.4G\rho_s r_s^3}{r}\left(\ln\left[\left(1+\frac{r}{r_s}\right)\left(1+\left(\frac{r}{r_s}\right)^2\right)^{0.5}\right] - \tan^{-1}\left(\frac{r}{r_s}\right)\right) \tag{3.8}$$

3.7.3 Navarro, Frenk and White (NFW) Profile

NFW profile is a traditional benchmark profile motivated by N-body simulations, which shallower than Pseudoisothermal in the central and steeper than Pseudoisothermal in the external part of the galaxy (J. F. Navarro et al., 1997). The density regions (J. F. Navarro et al., 1997), mass and velocity equation (Hashim et al., 2015) of the NFW model:

$$\rho_{NFW}(r) = \rho_s \frac{r_s}{r}\left(1+\frac{r}{r_s}\right)^{-2} \tag{3.9}$$

$$M_{NFW}(r) = 4\pi\rho_s r_s^3 \left(\ln\left(1+\frac{r}{r_s}\right) - \frac{r}{r_s+r}\right) \tag{3.10}$$

$$V_{NFW}^2(r) = \frac{12.6G\ \ _s r_s^3}{r}\left(\ln\left(1+\frac{r}{r_s}\right) - \frac{r}{r_s+r}\right) \tag{3.11}$$

3.7.4 Moore Profile

Moore profile behaves similarly to the NFW profile at large radii but is steeper than the NFW profile at smaller radii (Diemand et al., 2004). The density (Moore et al., 1999), mass (Klypin et al., 2001) and velocity equation of the Moore model:

$$\rho_{Moo}(r) = \frac{\rho_s}{\left(\frac{r}{r_s}\right)^{1.5}\left(1+\left(\frac{r}{r_s}\right)^{1.5}\right)} \tag{3.12}$$

$$M_{Moo}(r) = \frac{8}{3}\pi\rho_s r_s^3\left(\ln\left(1+\left(\frac{r}{r_s}\right)^{1.5}\right)\right) \tag{3.13}$$

$$V_{Moo}^2(r) = \frac{8.38G\rho_s r_s^3}{r}\left(\ln\left(1+\left(\frac{r}{r_s}\right)^{1.5}\right)\right) \tag{3.14}$$

3.7.5 Einasto Profile

Compared to other dark matter halo models that have two free parameters, the Einasto profile has three free parameters to describe the halo mass profile and significantly improves the accuracy of the fits to the internal density profiles of simulated halos (J. Navarro et al., 2010). The density, mass (Chemin et al., 2011) and velocity equation of the Einasto model:

$$\rho_{Ein}(r) = \rho_{-2}e^{\left[-2n\left(\left(\frac{r}{r_{-2}}\right)^{1/n}-1\right)\right]} \tag{3.15}$$

$$M_{Ein}(r) = 4\pi n r_{-2}^3\rho_{-2}e^{2n}(2n)^{-3n}\gamma\left(3n,\frac{r}{r_{-2}}\right) \tag{3.16}$$

$$V_{Ein}^2(r) = \frac{4\pi G n r_{-2}^3\rho_{-2}}{r}e^{2n}(2n)^{-3n}\gamma\left(3n,\frac{r}{r_{-2}}\right) \tag{3.17}$$

Where $\gamma(3n, x) = \int_0^x e^{-t} t^{3n-1} dt$, r_{-2} is the radius where the density profile has a slope of -2, ρ_{-2} is the local density at that radius and *r* is the radius from the center of the galaxy. The third free parameter of the Einasto model, *n* is an Einasto index that measures the shape of the density (Chemin et al., 2011).

3.7.6 Core-modified Profile

The NFW profile is singular at the central of the galaxy. To avoid the singularity, Brownstein proposed the core-modified profile, a model with constant density in the central core (Brownstein, 2009). The density, mass and velocity (X. Li et al., 2017) equation of the core-modified model:

$$\rho_{com}(r) = \frac{(\rho_s r_s^3)}{(r^3 + r_s^3)} \tag{3.18}$$

$$M_{com}(r) = \frac{4}{3}\pi\rho_s r_s^3[\ln(r^3 + r_s^3) - \ln(r_s^3)] \tag{3.19}$$

$$V_{com}^2(r) = \frac{4}{3}\pi G\rho_s \frac{r_s^3}{r}[\ln(r^3 + r_s^3) - \ln(r_s^3)] \tag{3.20}$$

3.7.7 DC14 Profile

DC14 profile considers the baryonic feedback on the halo due to the supernovae, and hence modifies the halo profiles (Cintio et al., 2014). Cintio et al. (2014) published the DC14 model, a profile determined in terms of the model class (α, β, γ) (Hernquist, 1990; Zhao, 1996):

$$\rho_{\alpha\beta\gamma}(r) = \frac{\rho_s}{((\frac{r}{r_s})^{\gamma}[1+(\frac{r}{r_s})^{\alpha}]^{((\beta-\gamma)/\alpha)})} \tag{3.21}$$

Where beta and gamma are the internal and external slopes respectively, and alpha describes the transition between the central and external part of the galaxy:

$$\alpha = 2.94 - \log((10^{((X+2.33)-1.08)} + 10^{((X+2.33)2.29)})$$

$$\beta = 4.23 + 1.34X + 0.26X^2$$

$$\gamma = -0.06 + \log((10^{((X+2.56)-0.68)} + 10^{(X+2.56)}) \quad (3.22)$$

Where $X = \log(M_{star}/M_{halo})$, is the stellar-to-halo mass (SHM) ratio in logarithm space. The mass (P. Li et al., 2020) and velocity of the DC14 model:

$$M_{DC14}(r) = 4\pi p_s r_s^3 \frac{1}{\alpha}(\mathrm{B}[a, b+1, \epsilon] + \mathrm{B}[a+1, b, \epsilon]) \quad (3.23)$$

$$V_{DC14}^2(r) = 4\pi G p_s \frac{r_s^3}{r}\frac{1}{\alpha}(B[a, b+1, \epsilon] + B[a+1, b, \epsilon]) \quad (3.24)$$

Where $B(a, b, x) = \int_0^x t^{(\alpha-1)}(1-t)^{(b-1)}dt$ is the incomplete Beta function, and $a = (3-\gamma)/\alpha$, $b = (\beta-3)/\alpha$ and $\epsilon = \frac{(r/r_s)^\alpha}{(1+(r/r_s)^\alpha)}$. This equation only works for the SHM ratio within -4.1 < X < -1.3, because this is the range where the supernovae feedback is significant and dominant (Cintio et al., 2014). At X < -4.1, the energy released by supernova is not enough to revise the initial cuspy model. On the another side, for X > -1.3, the feedback caused by active galactic nuclei (AGN) may begin to dominate (P. Li et al., 2020).

3.7.8 CoreNFW Profile

A coreNFW halo (Read et al., 2016) is essentially an NFW halo that transforms an internal cusp into a finite central core by a spherically symmetric function f_n that models the effects of supernova feedback (Allaert et al., 2017). The mass of coreNFW model:

$$M_{cNFW}(< r) = M_{NFW}(< r) f^n(r) \quad (3.25)$$

With

$$f(r) = [\tanh(\frac{r}{r_s})] \quad (3.26)$$

The strength of the core is determined by the parameter *n*, which ranges between $0 < n \leq 1$. The equation of *n*:

$$n = \tanh(\kappa \frac{t_{SF}}{t_{dyn}}) \tag{3.27}$$

Where κ is a tuning parameter and t_{SF} is the star formation time of the galaxy. The parameter is set, κ = 0.04 and t_{SF}= 14 Gyrs as suggested by the simulations of (Read et al., 2016). The dynamical time, t_{dyn} is the duration of 1 circular orbit at the scale radius in the unmodified NFW halo:

$$t_{dyn} = 2\pi \sqrt{\frac{r_s^3}{(GM_{NFW}(r_s))}} \tag{3.28}$$

Hence, the mass and velocity of coreNFW model:

$$M_{cNFW}(< r) = 4\pi\rho_s r_s^3 (\ln(1 + \frac{r}{r_s}) - \frac{r}{r_s + r}) f^n(r) \tag{3.29}$$

$$V_{cNFW}^2(< r) = 4\pi G\rho_s \frac{r_s^3}{r} (\ln(1 + \frac{r}{r_s}) - \frac{r}{r_s + r}) f^n(r) \tag{3.30}$$

3.7.9 Lucky13 Profile

Lucky13 is a new semi-empirical profile constructed from Equation (3.21), the (alpha, beta, and gamma) models by Li et al. (2020). They consider the transition parameter alpha = 1, gamma = 0 to reach a finite core and beta = 3 to get the same decreasing rate as the NFW profile at large radii. The density, mass and velocity of the Lucky13 model (P. Li et al., 2020):

$$\rho_{130} = \frac{\rho_s}{[1 + (\frac{r}{r_s})]^3} \tag{3.31}$$

$$M_{130}(r) = 4\pi\rho_s r_s^3 [\ln(1 + \frac{r}{r_s}) + \frac{2}{(1 + \frac{r}{r_s})} - \frac{1}{(2(1 + \frac{r}{r_s})^2)} - \frac{3}{2}] \tag{3.32}$$

$$V_{130}^2(r) = 4\pi G\rho_s \frac{r_s^3}{r}\left[\ln(1+\frac{r}{r_s}) + \frac{2}{(1+\frac{r}{r_s})} - \frac{1}{(2(1+\frac{r}{r_s})^2)} - \frac{3}{2}\right] \quad (3.33)$$

3.8 Star Velocity

Most of the luminous mass is occupied by stars, and the rest is less than 10% is by interstellar gases. Hence, the star disk luminosity distribution roughly represents the luminous mass distribution (Sofue, 2013). The velocity of the star disk obtained is determined by Freeman (Di Paolo et al., 2019; Freeman, 1970) is as follow:

$$V_{star}^2 = \frac{GM_D x^2}{2R_D}(I_o K_o - I_1 K_1) \quad (3.34)$$

Where G is the universal gravitational constant, I_n and K_n are the modified Bessel functions of the first and second kinds computed at $x/2$ and $x = \frac{r}{R_D}$, M_D is the star mass and R_D is the star scale length. The star scale length for NGC 4321 obtained is 75 arcsec (Koopmann et al., 2001), which is equivalent to 6.22 kpc.

3.9 Gas Velocity

Taking account of the gas component, it is possible to calculate the rotation curve of the baryonic disk component (Zasov et al., 2017). The mass of the gas is computed from the equation (Hashim et al., 2015):

$$M_{gas}(r) = 2\pi \int_0^r r\sigma(r)dr \quad (3.35)$$

Where r is the radius from the center of the galaxy and $\sigma(r)$ is the surface density. The procedures of acquiring the gas velocity:

i. Employ the total gas surface brightness from T. Wong and L. Blitz (Wong & Blitz, 2002) as shown in Figure 3.9.

ii. Construct the best-fitting curve that is computed from a few combinations of the parameters and the result is demonstrated in Figure 3.10.

iii. Compute the goodness of fit to signify the best-fitting curves.

iv. Adopt the best model of the Σgas surface density, $\sigma(r)$ to Equation (3.35) to calculate the mass of gas for each radius.

v. The velocity for each radius is calculated by using the equation of rotational velocity as below and the result is plotted as shown in Figure 3.11.

$$v = \sqrt{\frac{GM}{r}} \tag{3.36}$$

Where v is the rotational velocity of the object, G is the universal gravitational constant, m is the mass of the object and r is the radius of the orbit.

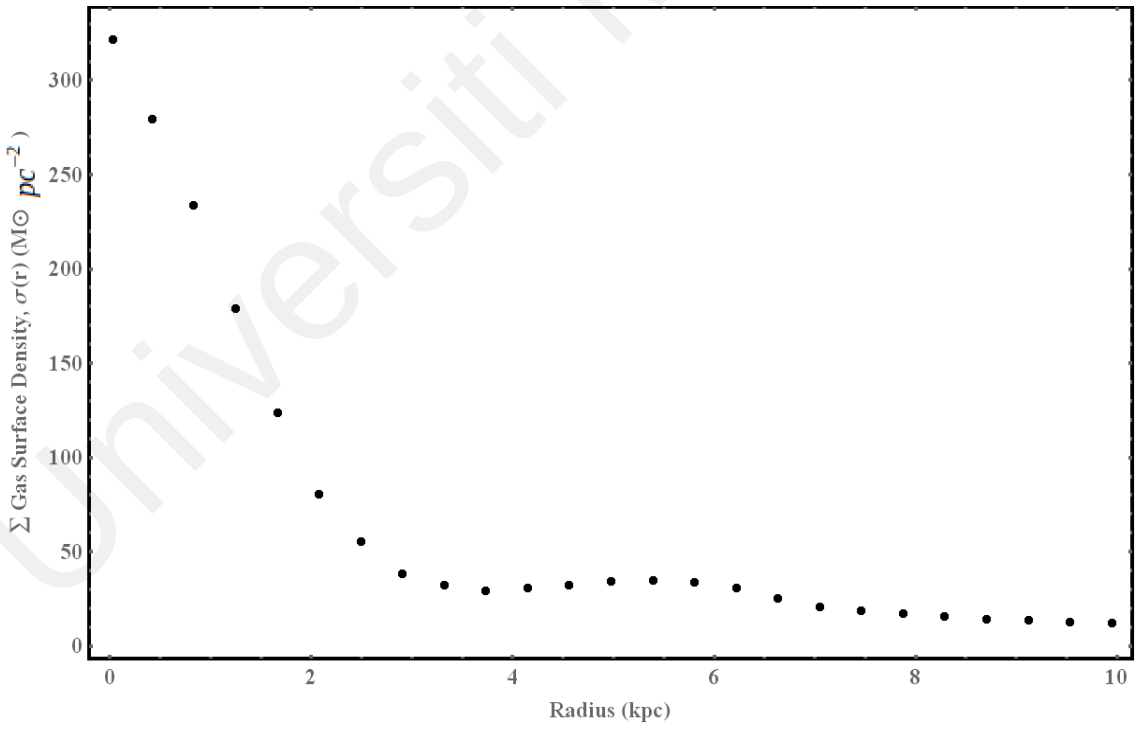

Figure 3.9: Total gas surface density graph

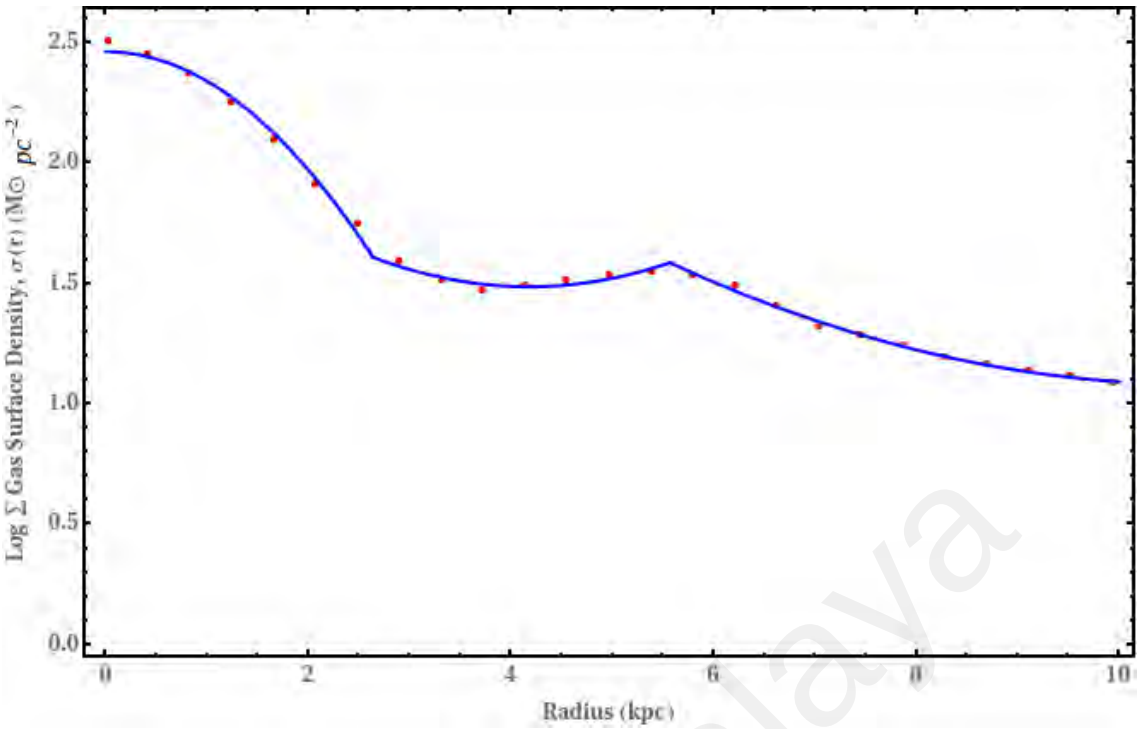

Figure 3.10: The best fit graph with χ^2 = 0.94.

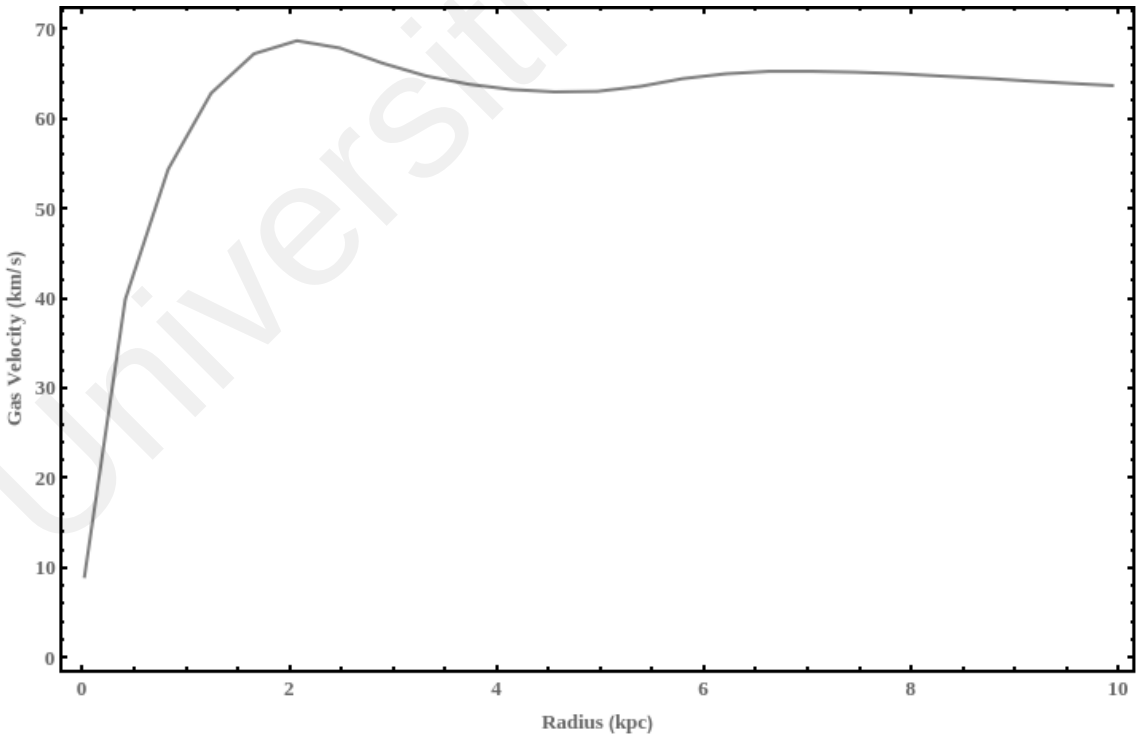

Figure 3.11: Gas velocity graph

CHAPTER 4: RESULTS & DISCUSSION

4.1 Nonlinear Fitting Rotation Curve for HI Observed Data

By referring to Equation (3.1), $V_{rot}^2 = V_{gas}^2 + V_{star}^2 + V_{DM}^2$, $V_{rot}^2 = V_{HI}^2$ from VLA data. For gas velocity, V_{gas}^2 is computed from gas surface brightness. Meanwhile, a nonlinear rotation curve fitting is applied on star and dark matter velocity to get the best fitted free parameters. For star velocity, V_{star}^2, the Equation (3.34) will be used while for dark matter velocity V_{DM}^2, the Equation (3.5), (3.8), (3.11), (3.14), (3.17), (3.20), (3.24), (3.30), (3.33) will be used for Pseudoisothermal, Burkert, NFW, Moore, Einasto, core-modified, DC14, coreNFW and Lucky13 profiles respectively. The best nonlinear fitting rotation curve by using the nine dark matter halo models are illustrated in Figure 4.1.

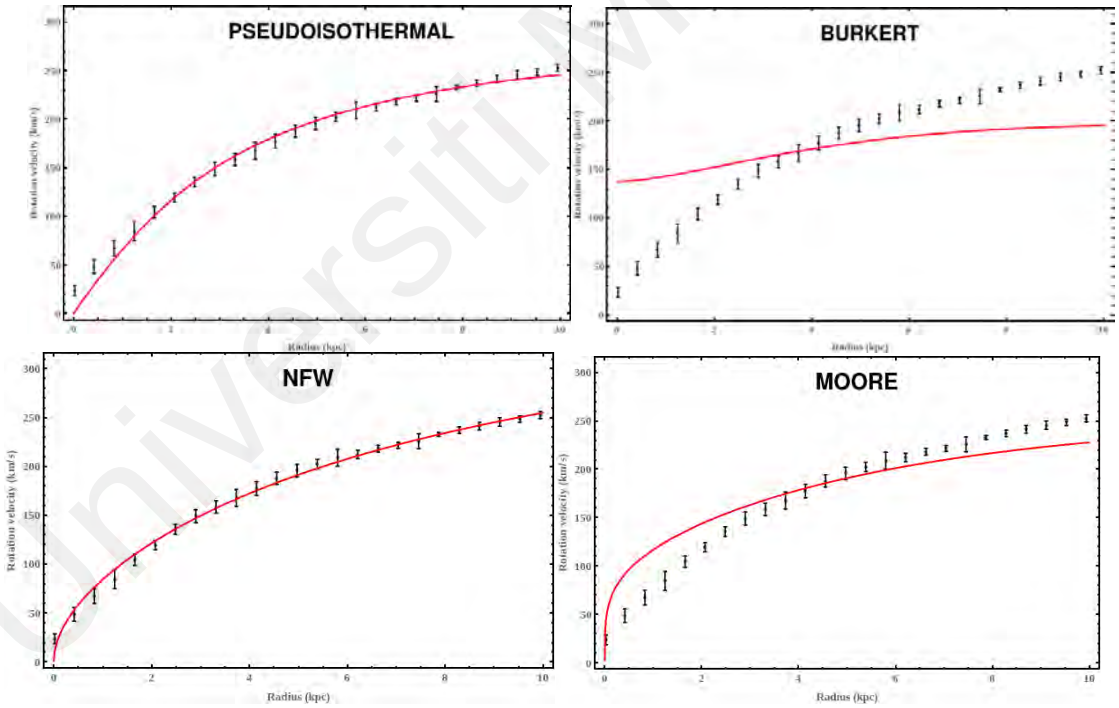

Figure 4.1: Nonlinear fitting rotation curve by applying the nine dark matter halo models

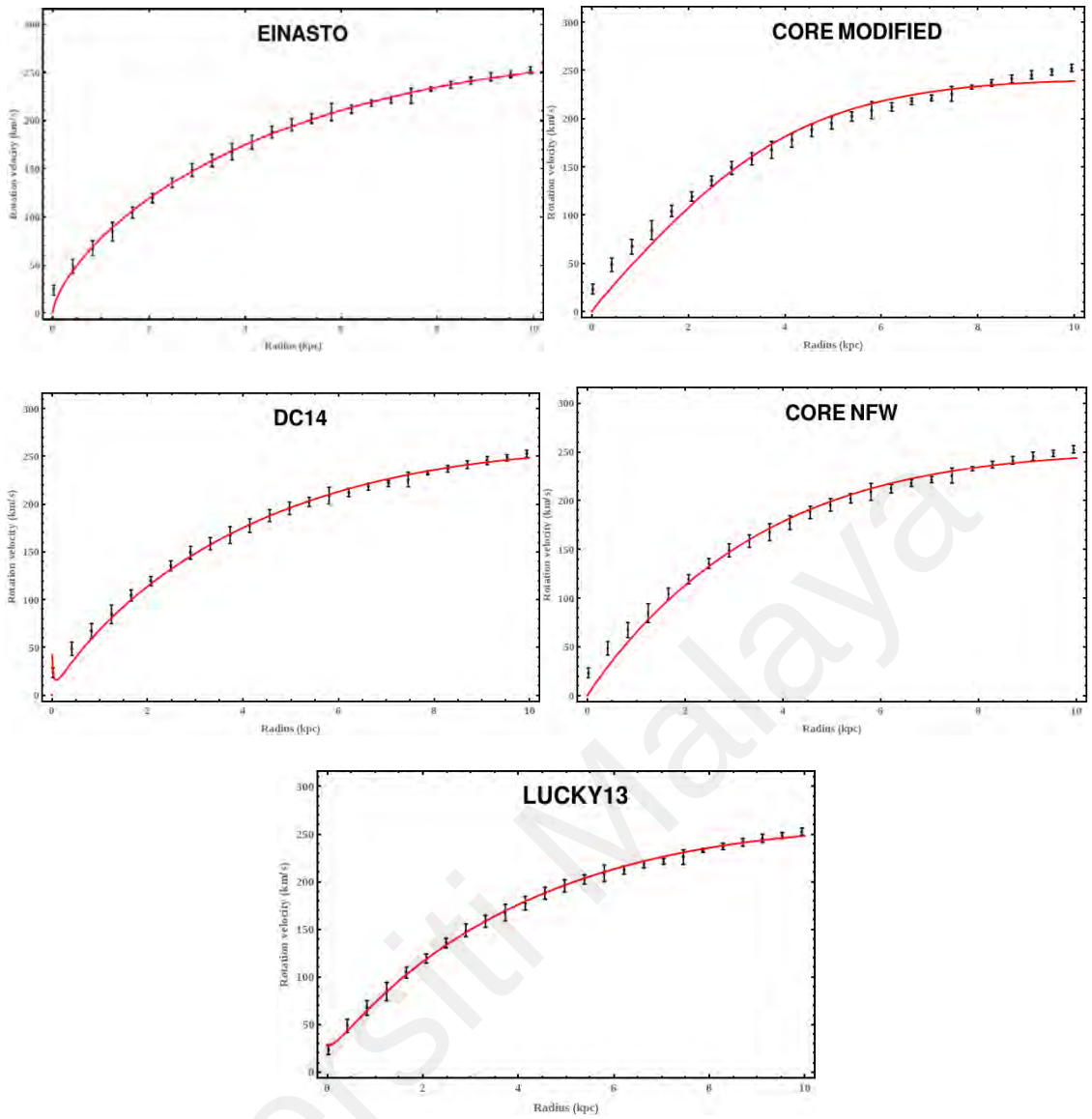

Figure 4.1, Continued.

By referring to Figure 4.1, all dark matter profiles have good fitting except Burkert and Moore profiles. While for other dark matter profiles, it is hard to analyze the other best fitting rotation curve by using the eye observing only. Hence, the results are further visualized by analyzing the goodness of fit. The goodness of fit of a statistical model illustrates how well the observation data fitted by the theoretical data that have modelled. Measuring the goodness of fit can summarize the divergence between the observed values and the modelling values. In this research, the goodness of fit will be judged by applying

the residual analysis, mean prediction band, dark matter distribution in rotation curve and reduced chi-square calculation, as further discussed in the following subchapter.

4.2 Residual Analysis

During a rotation curve fitting, the regression curve will be fit as best as possible to lie on every data point. However, usually not every data point will fall exactly on the rotation curve, they are scatted around. In general, a residual is a difference between the observed value and the predicted value. The residual can be presented in equation format:

$$V_{res} = V_{obs} - V_{pre} \tag{4.1}$$

Where V_{res} , V_{obs} and V_{pre} are the residual, observed and predicted value respectively.

Each data point has one residual. In a rotation curve fitting, the residual will show a positive value if the regression curve is below the data point and will shows a negative value if the regression curve is above the data point. In addition, if the regression line exactly connects the data point, the residual will show a value of zero. After the residual calculation for each data point, a residual graph will be plotted (Larsen & McCleary, 1972). The residual plot for rotation curve fitting by using the nine dark matter halo profiles are as shown in Figure 4.2.

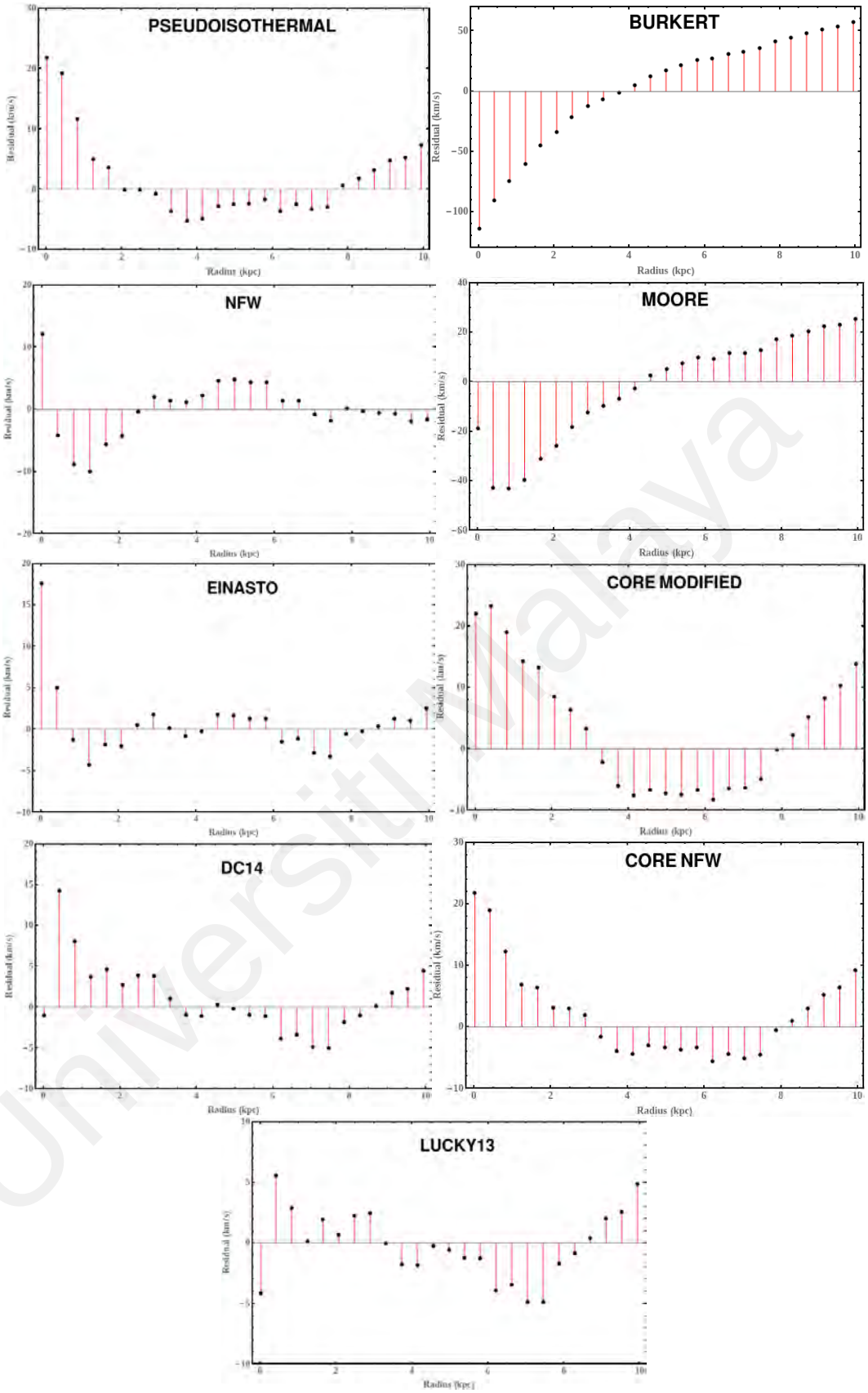

Figure 4.2: The residual plot for rotation curve fit of the nine dark matter profiles

In Figure 4.2, each residual plot illustrates a different y-axis value because each dark matter profile has different residual results between the observed value and the predicted value. Some dark matter profiles have a large residual value while some dark matter profiles have only a small residual value. Generally, Pseudoisothermal, core-modified and coreNFW perform a U-shaped pattern while the other dark matter profiles demonstrate a random pattern distribution. By analyzing each dark matter profile specifically, the Burkert and Moore profiles have a larger residual plot result. The range of residual plot for Burkert and Moore profiles are -120 $kms^{-1} < V_{res} < 60\ kms^{-1}$ and -50 $kms^{-1} < V_{res} < 30\ kms^{-1}$ respectively. Besides Burkert and Moore profiles, the other seven dark matter profiles have a smaller residual plot result. Pseudoisothermal, NFW, core-modified and coreNFW profiles have 40 kms^{-1} differences in the residual plot. The range of residual plot for NFW is between -20 kms^{-1} to 20 kms^{-1} while the range of residual plot for the other three profiles is the same, which are between -10 kms^{-1} to 30 kms^{-1}. On the other hand, Einasto and DC14 profiles have the same residual difference and range of residual plot, which are 30 kms^{-1} and -10 $kms^{-1} < V_{res} < 20\ kms^{-1}$ respectively. Lastly, the Lucky13 profile has the smallest residual difference with 20 kms^{-1} and the range of the residual plot is between -10 kms^{-1} to 10 kms^{-1}.

4.3 Mean Prediction Band

The prediction interval has provided a lot of useful information due to it indicates a method to quantify a replication research might diverge from an original research (Spence & Stanley, 2016). The prediction band is closely related to the prediction interval, which predicts the possibility regarding a position of a new data point might be located on the graph. The function of the prediction band is used to cover the values of one or more future data points with a stipulated probability from the same data set population was sampled. In this research, a mean prediction band is constructed with a confidence level

of 68%, 95% and 99%. The mean prediction band for the nine dark matter halo models are as shown in Figure 4.3.

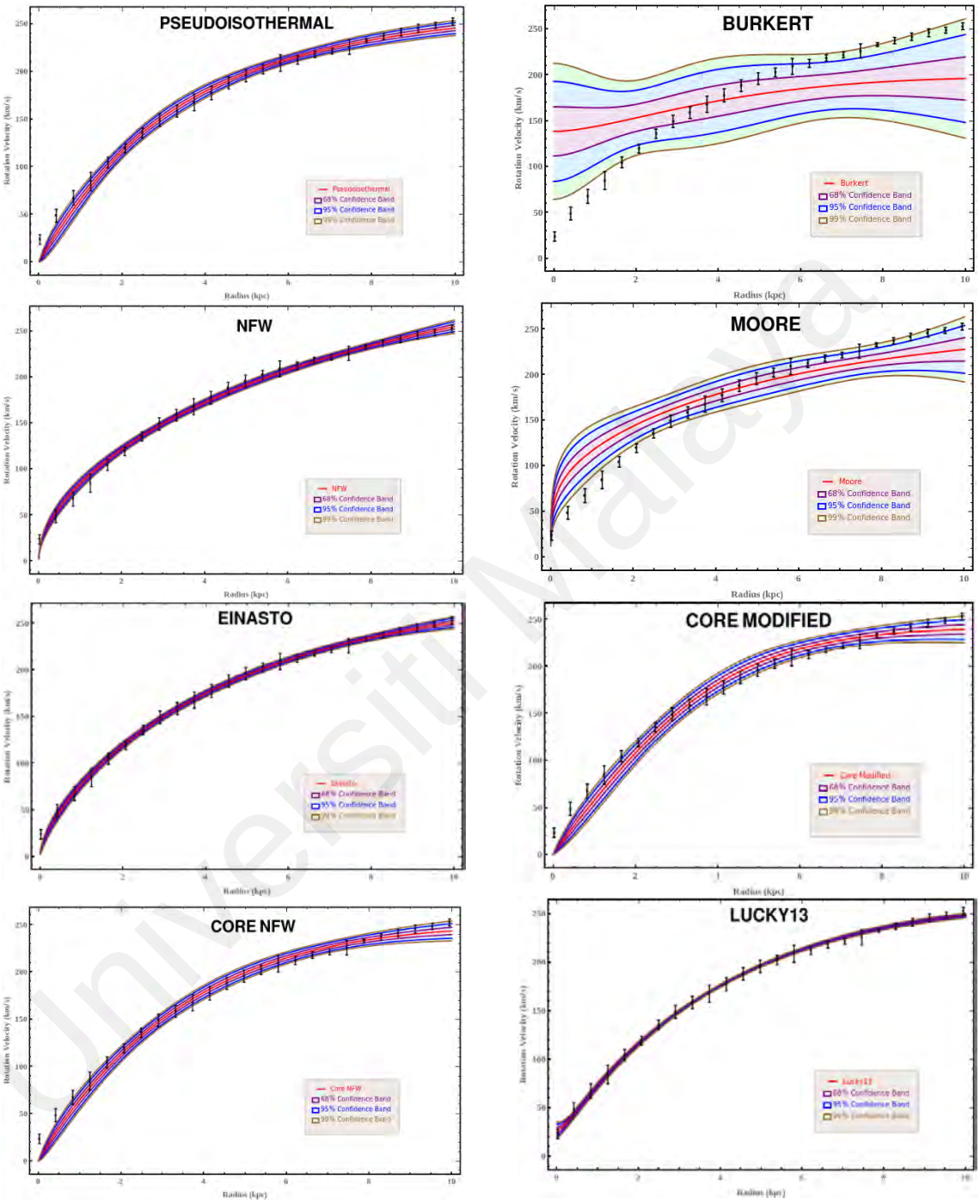

Figure 4.3: Mean prediction band with confidence level of 68%, 95% and 99% of the eight dark matter profiles (except DC14 profile).

For Figure 4.3, only 8 mean prediction band graphs have been plotted and do not have a mean prediction band for DC14 dark matter profile. This is due to the DC14 dark matter profile consisting of real and complex parts. During DC14 model fitting, for the real part,

a rotation curve is successfully plotted. Meanwhile, the complex part is invalid for the rotation curve fitting. Hence, the rotation curve is only able to be plotted for the real part and omitted the complex part. However, the mean prediction band is invalid for the complex part. During mean prediction band plotting, it displayed plotting error due to the existence of a complex part of the model. The mean prediction band has been tried to plot for the real part only but not successful due to the limitation of software Mathematica. The absence of the DC14 profile in the mean prediction band will not affect the rotation curve analysis in the following subchapter.

In Figure 4.3, Burkert and Moore profiles have larger shaded area compare to the other six dark matter profiles and many data point is out of the 99% confidence level. Lucky13 profile has the smallest shaded area among eight dark matter profiles. However, the smallest shaded area of 99% confidence level of Lucky13 profile is unable to cover most of the data point error bars. For the other five dark matter models, all of them are able to cover most of the data points but not fully cover all error bars. In addition, all five dark matter profiles have the same issue, which is the shaded area of 99% confidence level is unable to fully cover the internal radius of the galaxy especially Pseudoisothermal, core-modified and coreNFW profiles. Among these five dark matter profiles, core-modified profile has the largest shaded area, and follow by Pseudoisothermal and coreNFW profiles, both of them have a similar shaded area. Meanwhile, the NFW and Einasto profiles have a smaller issue in the internal radius of the galaxy and also both of them have a similar smaller shaded area of 99% confidence level. However, the smaller shaded area of these two profiles causes a lot of error bars is not fully covered. In a nutshell of the mean prediction band, there is no perfect dark matter profile which can fully cover all data points and error bars.

4.4 Free Parameter and Rotation Curve for HI Observed Data

Next, the value of free parameters is obtained from the best fit rotation curve in the subchapter 4.1. The free parameter of star mass M_D is for all dark matter halo profiles. The free parameters of scale density p_s and scale radius r_s obtained is for eight dark matter halo profiles, except the Einasto profile. This is because the Einasto profile have a different definition for these free parameters. The radius and density of the Einasto profile are r_{-2}, and p_{-2} respectively. Furthermore, the third free parameter of the Einasto profile, the Einasto index is fitted to n = 0.77 ± 0.027. The best fitted free parameters for the nine dark matter halo models are as shown in Table 4.1. Then, by applying the free parameters in Table 4.1, the rotation curves for the nine dark matter halo models are shown in Figure 4.4.

Table 4.1: Free parameter obtained for HI observed data by applying the nine dark matter halo models

Dark Matter Profile	M_D (M⊙)	p_s ($p_{-2}$for Einasto) (M⊙ kpc^{-3})	r_s ($r_{-2}$for Einasto) (kpc)
Pseudo-isothermal	$(5.46 \pm 12.97) \times 10^{10}$	$(1.98 \pm 1.23) \times 10^{8}$	2.55 ± 0.24
Burkert	$(5.56 \pm 4.53) \times 10^{10}$	$(1.62 \pm 7.93) \times 10^{7}$	5.72 ± 14.61
NFW	$(5.43 \pm 2.82) \times 10^{10}$	$(1.48 \pm 0.53) \times 10^{6}$	66.77 ± 21.88
Moore	$(5.56 \pm 7.94) \times 10^{10}$	$(1.20 \pm 10.11) \times 10^{6}$	43.88 ± 251.20
Einasto	$(5.50 \pm 6.21) \times 10^{10}$	$(3.87 \pm 1.38) \times 10^{7}$	8.44 ± 1.84
core-modified	$(5.26 \pm 6.88) \times 10^{10}$	$(5.57 \pm 2.00) \times 10^{7}$	4.10 ± 0.25
DC14	$(2.43 \pm 0.02) \times 10^{11}$	$(7.47 \pm 0.01) \times 10^{8}$	0.04 ± 0.01
coreNFW	$(5.57 \pm 12.89) \times 10^{10}$	$(6.43 \pm 4.17) \times 10^{7}$	5.23 ± 0.36
Lucky13	$(2.43 \pm 0.04) \times 10^{11}$	$(0.42 \pm 5.48) \times 10^{7}$	5.08 ± 32.96

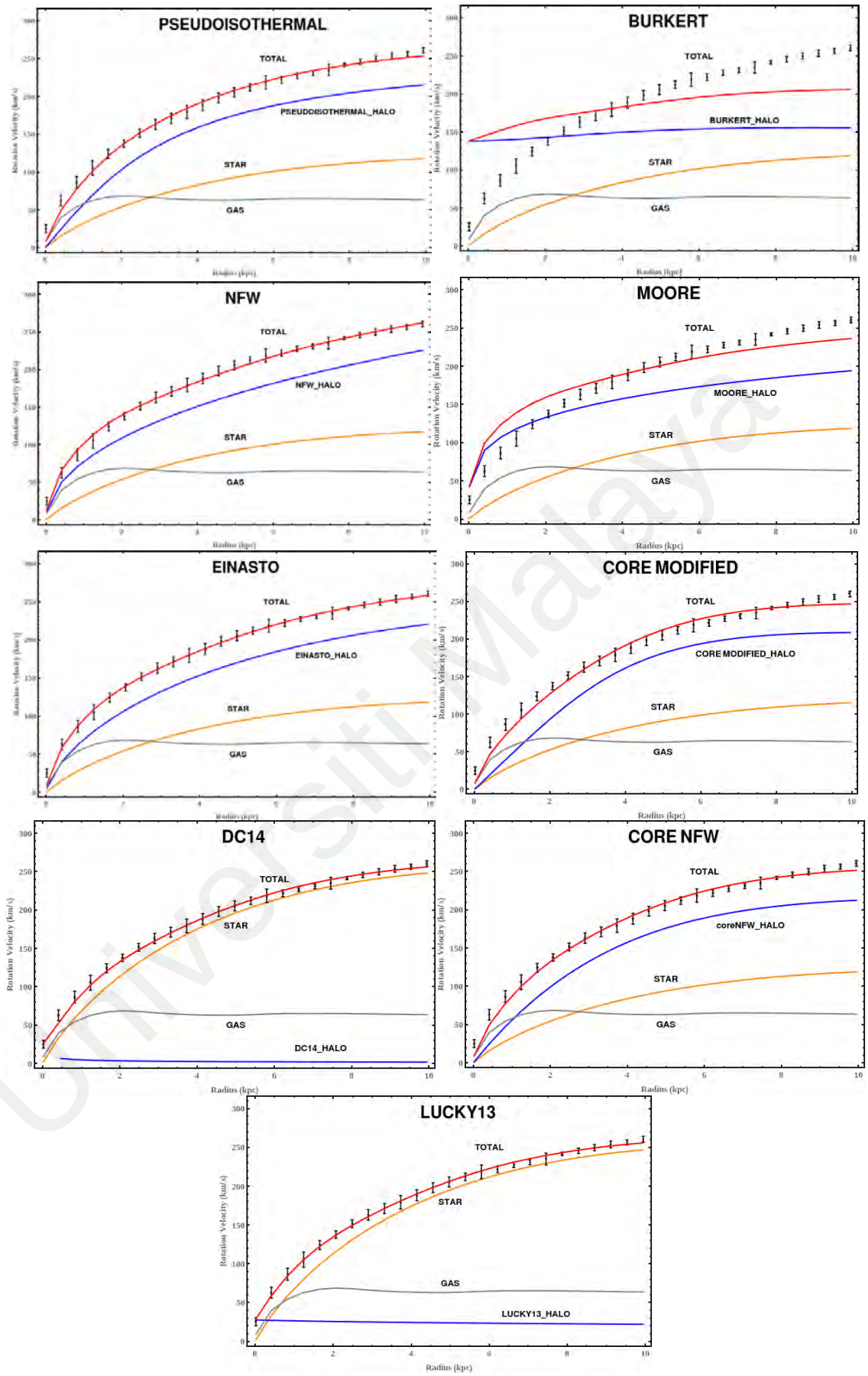

Figure 4.4: The nonlinear rotation curve of NGC 4321 by using HI observed data and the nine dark matter halo models.

In Figure 4.4, the best fitted rotation curve for DC14 and Lucky13 dark matter profiles is rejected. This is because the unpractical lower value in the velocity of dark matter for the entire radius of 10 kpc. DC14 dark matter profile not suitable in the galaxy NGC 4321 is due to the equation only applicable for SHM ratio in the range of -4.1 < X < -1.3 (Cintio et al., 2014). During rotation curve fitting, X acts as a free parameter and fitted in the range of -4.1 to -1.3. However, all values within the range given were not able to produce a reasonable dark matter velocity. On the other hand, the Lucky13 dark matter profile is a new semi-empirical profile that modifies the alpha, beta and gamma of the (α, β, γ) model. The gamma is set to 0 to reach a finite core, beta is set to 3 to get the same decreasing rate as the NFW profile at large radii and transition parameter alpha is set to 1 (P. Li et al., 2020). However, this new setting changes of the semi-empirical profile are not applicable in this galaxy.

By referring to dark matter halo model history, the Burkert profile is statistically more suitable for dark matter-dominated dwarf galaxies (Burkert, 1995). Burkert profile modifies the density law of the Pseudoisothermal profile in the central part of the galaxy and diverges logarithmically in larger radii. In Figure 4.4, the Burkert profile indicates the presence of dark matter in the central region of the galaxy with velocity 138 kms^{-1}. The velocity of dark matter is then increasing steadily until the external region of the galaxy. However, the total rotation velocity from observation data was only 25 kms^{-1} in the central region of the galaxy. The big difference between total rotation velocities with the dark matter velocity proposes that the Burkert dark matter halo profile is rejected for the galaxy NGC 4321 too.

Moore profile behaves similarly to NFW profile at the external region of the galaxy but is steeper than NFW profile at the central region of the galaxy (Diemand et al., 2004). In Figure 4.4, for the Moore profile, the dark matter velocity has the sharpest rise in the

central region of the galaxy by comparing to other dark matter profiles (except for the DC14 and Lucky13 profiles). Furthermore, the steepness of the Moore dark matter profile causes the dark matter velocity to be more than the total rotational velocity at the central part of this galaxy. Although the steepness of dark matter velocity decreases after a radius of 0.5 kpc but the dark matter velocity remains higher than the total rotational velocity within a radius of 2.0 kpc. When the radius is beyond 2.0 kpc, the velocity of dark matter is getting lower than the total rotational velocity until the external region of the galaxy. In conclusion, the total rotational velocity lower than the dark matter velocity of Moore profile before the radius of 2.0 kpc shows that the Moore profile is not applicable for the galaxy NGC 4321 too.

Meanwhile, by looking at the Figure 4.4, it is very hard to define which dark matter halo profile is better for the other five accepted dark matter halo models. Hence, a reduced chi-square test will be calculated first before analyzing the remaining dark matter halo profiles.

4.5 Reduced Chi-Square Test for HI Observed Data

A chi-square (χ^2) statistic is commonly used for measuring the difference between the observed values and the modelled values outcome of a set of variables. A chi-square test depends on the differences between actual and observed values, the degrees of freedom and the sample size of the data. The goodness-of-fit is examined by introducing the chi-square calculation. The goodness-of-fit parameter, χ^2 (Bevington & Robinson, 1969) is as below:

$$\chi^2 = \sum_{i=1}^{N} \frac{1}{\sigma_i^2} [y_i - y(x_i, a, b, c)]^2 \quad (4.2)$$

Where N is observed data points, σ_i is the uncertainty in y_i, y_i is the observed values in rotation curve, $y(x_i, a, b, c)$ are the values of the model function calculated at x_i, x_i is the radius from the center of the galaxy and *a, b, c* are the fitted parameters.

Next, a reduced chi-square calculation is performed to check the goodness-of-fit of rotation curve fitting. Reduced chi-square is determined as chi-square per degree of freedom as below:

$$\chi^2_{redu} = \frac{\chi^2}{v} \tag{4.3}$$

Where the degree of freedom, $v = N - N_c$, N and N_c is the number of data points and fitted parameters. In concept, $x^2_{redu} > 1$ explains that the fit is not fully seizing in the data and $x^2_{redu} \gg 1$ represents a poor model fitting. In contrast, $x^2_{redu} < 1$ means the model is over fitting the data. The best fit between the observed data and modelled data will show a reduced chi-square approximate to 1. A value x^2_{redu} = 1 reveals that the fitting between the observations data and the estimates value is in agreement with the error variance (Bevington & Robinson, 1969).

The reduced chi-square, x^2_{redu} for the remaining accepted dark matter halo models are demonstrated in Table 4.2. In overall, four out of five dark matter halo models achieved the reduced chi-square test in the range of 0.40 < x^2_{redu} < 1.70. Among them, Pseudoisothermal profile achieves the x^2_{redu} closest to 1. For cored profiles, the core-modified and coreNFW profiles achieved x^2_{redu} with 3.29 and 1.64 respectively. On the other hand, the Einasto and cuspy NFW profiles achieved similar x^2_{redu} with 0.52 and 0.49 respectively.

Table 4.2: The reduced chi-square test for the five dark matter halo profiles

Dark Matter Profile	x_{rdu}^2
Pseudoisothermal	1.25
NFW	0.49
Einasto	0.52
Core-modified	3.29
CoreNFW	1.64

Next, the five accepted dark matter halo profiles will be analyzed by referring to the rotation curve in Figure 4.4 and the reduced chi-square calculation results in Table 4.2.

Core-modified is a dark matter halo profile with constant density in the center core to avoid singularity in the central region of the galaxy (Brownstein, 2009). However, the constant density in the central core makes this profile only have very little flexibility during fitting the rotation curve. During the rotation curve modelling, the core-modified profile has a limited and not much fitting modification could be changed especially in the internal core of the galaxy. For the external part of the galaxy, the velocity of dark matter is increasing slowly and becomes nearly constant after the radius of 7.5 kpc. The dark matter velocity should be continuously increased since the total rotational velocity remains increasing. The increase in velocity of dark matter in the external part of the galaxy NGC 4321 can be observed in the other four accepted dark matter halo models. Generally, the core-modified profile is able to fit this galaxy and the dark matter velocity is reasonable to compare to the above four rejected dark matter halo models. However, the less flexibility in the core of the galaxy and the fixed dark matter velocity in the external part of the galaxy causes the core-modified halo model to be worse than the other four accepted dark matter halo models and achieved a x_{redu}^2 of 3.29.

A coreNFW halo is essentially an NFW halo that reforms an internal cusp into a finite central core (Read et al., 2016). The alternation of an internal cusp into a finite central core of the coreNFW profile produces an improvement during the rotation curve

modelling at the central part of the galaxy. In Figure 4.4, the steepness of coreNFW halo profile contributes a good rotation curve fitting with total rotational velocity in the central part of the galaxy NGC 4321. However, the increasing rate of dark matter halo velocity has been reducing after 8 kpc radius. The decreasing of dark matter halo velocity after the radius of 8 kpc shows a mismatch with the continuously rising total rotational velocity. The problem leads to the coreNFW dark matter halo model is not as good as the Peudoisothermal model and achieved a x^2_{redu} of 1.64.

The NFW profile is often called 'universal' because it agrees with a huge variety of dark matter masses, from individual galaxies to the large galaxy clusters (J. F. Navarro et al., 1997). The characteristic of the NFW profile makes it have a good rotation curve fitting in galaxy NGC 4321. However, the NFW profile involves the cuspy issue with increasing sharply at small radii (De Blok et al., 2001). The cuspy issue can be observed in Figure 4.4, where the dark matter velocity of the NFW dark matter profile is sharper than the Pseudoisothermal, Einasto and coreNFW profiles in the center part of the galaxy. Within the radius in the range from 0 kpc to 1 kpc, the steepness of the NFW profile makes the rotational velocity of star, gas and dark matter are not equal to the total rotational velocity. The misalignment of the rotational velocity fitting leads to the rotation curve fitting of NFW dark matter profile achieved x^2_{redu} of 0.49, a little bit different from the Einasto profile.

High-resolution *N*-body CDM simulations illustrate that the nonsingular three-parameter model of the Einasto profile accomplish better and provides an excellent fit to a wide range of dark matter haloes (Retana-Montenegro et al., 2012). The third parameter of Einasto dark matter profile, n, demonstrates the shape of the whole distribution, smaller values of *n* leads to a shallower central region and sharper external region (Graham et al., 2006). The total rotational velocity of the galaxy NGC 4321 shows a shallower in the

internal region of the galaxy and a sharper in the external region of the galaxy. In this situation, the Einasto index, *n*, make a very significant role to meet the requirement of the rotation curve fitting. A smaller number of n is needed in order to build the central region shallower and external region steeper. In Figure 4.4, the rotation curve of the Einasto profile is a good fit with the total rotational velocity. However, the additional third parameter causes the Einasto dark matter halo model too similar to every data point until it over fit with a x^2_{redu} of 0.52.

Pseudoisothermal profile is a widely used model for the analysis and is frequently fits the rotation curve better than the NFW model (De Naray et al., 2006). This characteristic of the Pseudoisothermal profile is applicable for the galaxy NGC 4321 too. In Figure 4.4, the whole distribution is a very good fit with the total rotational velocity. Furthermore, the Pseudoisothermal dark matter profile has a linear growth in the center part shift to flat at the external region of the galaxy (Begeman et al., 1991). This theory can be applied in this galaxy too, the dark matter velocity in the center region within 1 kpc is increasing linearly and then shifting to flat at the external region of the galaxy. The linearly in the center region and flat at the external region of the fitting characteristic are match with the total rotational velocity of the galaxy NGC 4321. This leads to Pseudoisothermal achieved the best fitting among the nine dark matter profiles with x^2_{redu} of 1.25, nearest to 1.

4.6 The Mass of Dark Matter for HI Observed Data

By obtaining the free parameter in Table 4.1, the total mass of star and dark matter within a radius of 10 kpc are computed and illustrated in Table 4.3. The star velocity is obtained from Equation (3.34) and transformed to star mass with Equation (3.36), while the dark matter mass is applying the Equation (3.4), (3.10), (3.16), (3.19), (3.29) for Pseudoisothermal, NFW, Einasto, core-modified and coreNFW profiles respectively.

Table 4.3: The dark matter mass within radius 10 kpc for the five accepted dark matter profiles

Dark Matter Profile	Mass of star (M⊙)	Mass of dark matter (M⊙)
Pseudoisothermal profile	$(3.23 \pm 7.66) \times 10^{10}$	$(1.08 \pm 0.01) \times 10^{11}$
Einasto profile	$(3.25 \pm 3.67) \times 10^{10}$	$(1.13 \pm 0.01) \times 10^{11}$
Core-modified profile	$(3.11 \pm 4.07) \times 10^{10}$	$(1.01 \pm 0.01) \times 10^{11}$
coreNFW profile	$(3.29 \pm 7.61) \times 10^{10}$	$(1.10 \pm 0.01) \times 10^{11}$
NFW profile	$(3.21 \pm 1.66) \times 10^{10}$	$(1.19 \pm 0.10) \times 10^{11}$

The total mass of dark matter for the five accepted dark matter halo models within a radius of 10 kpc in the galaxy NGC 4321 is in the range from $(1.01 \pm 0.01) \times 10^{11}$ M⊙ to $(1.19 \pm 0.10) \times 10^{11}$ M⊙. By taking consideration of the reduced chi-square, the Pseudoisothermal, Einasto, coreNFW and NFW profiles achieved x^2_{redu} in the range of $0.40 < x^2_{redu} < 1.70$. The dark matter mass of these four halo models in the galaxy NGC 4321 are very close, which are from the range of $(1.08 \pm 0.01) \times 10^{11}$ M⊙ to $(1.19 \pm 0.10) \times 10^{11}$ M⊙.

4.7 Free Parameter and Rotation Curve for CO Observed Data

By applying the five accepted dark matter halo profiles obtained in HI observed data, a nonlinear fitting rotation curve will be done for CO observed data. By referring to Equation (3.1), $V^2_{rot} = V^2_{gas} + V^2_{star} + V^2_{DM}$, $V^2_{rot} = V^2_{CO}$ from ALMA data, V^2_{gas} is the same as HI observed data, while for star velocity, V^2_{star}, Equation (3.34) will be used. For dark matter velocity V^2_{DM}, five accepted profiles will be used, Equation (3.5), (3.11), (3.17), (3.20), (3.30) for Pseudoisothermal, NFW, Einasto, core-modified, and coreNFW profiles respectively.

Next, the free parameters will be obtained from the best fitted rotation curve that has been plotted. The third free parameter of the Einasto profile is fitted to n = 0.39 ± 0.01. The other free parameters fitting for the five accepted dark matter halo profiles are as

shown in Table 4.4. Then, by applying the free parameters obtained in Table 4.4, the rotation curves of the total rotational velocity are plotted with gas, star and dark matter velocities for CO observed data, are as shown in Figure 4.5.

Table 4.4: Free parameter obtained for CO observe data by using five accepted dark matter halo profiles

Dark Matter Profile	M_D (M⊙)	p_s ($p_{-2}$for Einasto) (M⊙ kpc^{-3})	r_s ($r_{-2}$for Einasto) (kpc)
Pseudo-isothermal	$(1.08 \pm 0.25) \times 10^{11}$	$(3.89 \pm 9.02) \times 10^{10}$	0.12 ± 0.15
NFW	$(1.81 \pm 0.16) \times 10^{11}$	$(5.25 \pm 2.86) \times 10^{10}$	0.16 ± 0.04
Einasto	$(1.96 \pm 0.06) \times 10^{11}$	$(2.86 \pm 0.80) \times 10^{8}$	1.58 ± 0.21
core-modified	$(1.81 \pm 0.19) \times 10^{11}$	$(2.86 \pm 1.96) \times 10^{10}$	0.20 ± 0.06
coreNFW	$(1.81 \pm 0.37) \times 10^{11}$	$(3.25 \pm 4.61) \times 10^{10}$	0.19 ± 0.12

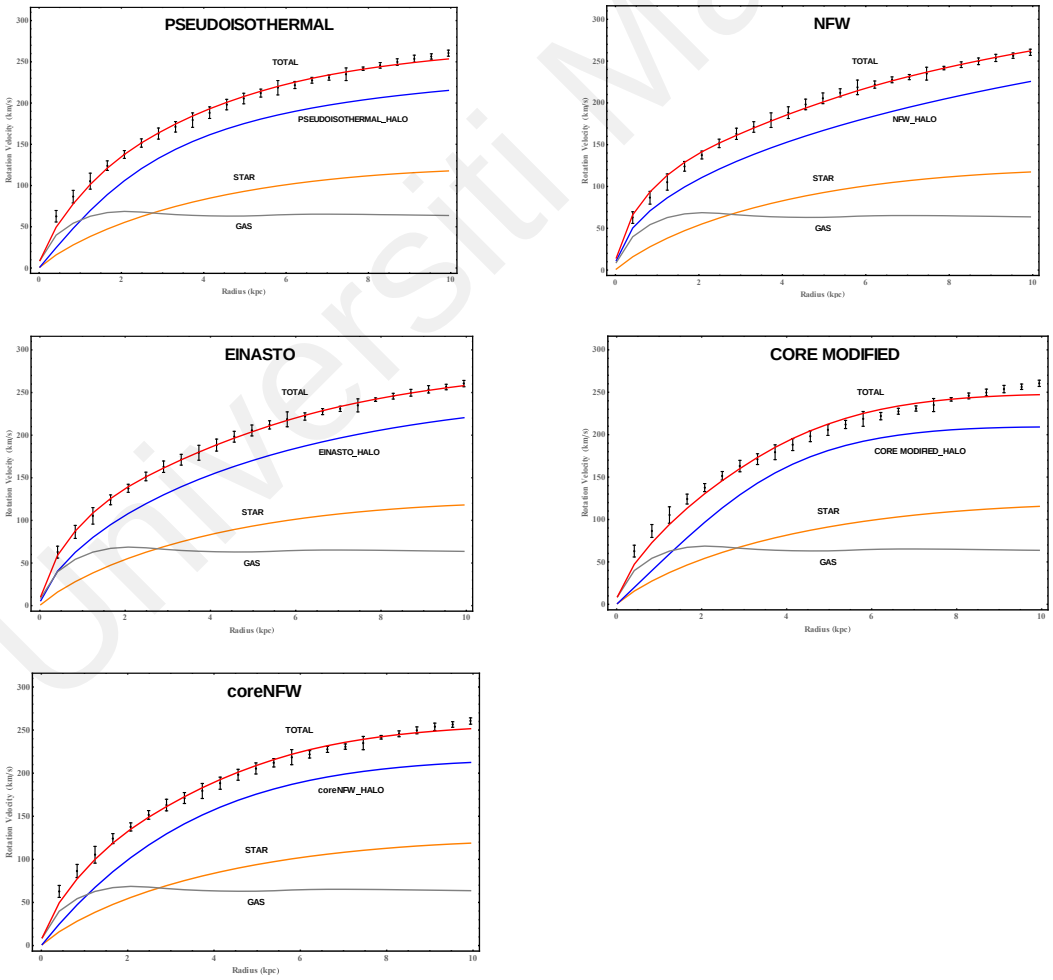

Figure 4.5: The nonlinear fitting rotation curve by using 5 dark matter profiles fitted to CO observed data.

The rotational velocities of the dark matter showed a big difference between the cases for HI and CO observed data. In Figure 4.4, the dark matter velocity of the five accepted dark matter profiles increases steadily from 0 kpc to an external radius of 10 kpc. In Figure 4.5, the dark matter velocity of the five dark matter profiles increases until 0.5 kpc radius then decreases until 7 kpc radius except for the Pseudoisothermal profile. The dark matter velocity of the Pseudoisothermal profile increases until 0.5 kpc radius then the velocity remains constant until 7 kpc radius.

4.8 Reduced Chi-Square Test and the Mass of Dark Matter for CO Observed Data

Reduced chi-square was used for CO observed data to measure the goodness-of-fit. In Figures 4.4 and 4.5, the rotational velocity of HI and CO started differently from the central region of the galaxy. CO data starts from higher rotational velocity 166 kms^{-1} while HI data starts from lower rotational velocity 62 kms^{-1}. In Figure 4.4, the lower rotational velocity in the internal region of this galaxy by HI observed data make the fitting smoothly and a good starting fit from 0 kpc to external radius 10 kpc. In Figure 4.5, the higher rotational velocity in the internal region of this galaxy by CO observed data causes the fitting hardly and most of the dark matter profile unable to fit well at internal radius, but the fitting is getting better as the radius increases. Due to the different fitting in internal radius by HI and CO observed data, their reduced chi-square has a big difference. The reduced chi-square, χ^2_{redu} for CO observed data by using five dark matter halo profiles are as demonstrated in Table 4.5.

Table 4.5: The reduced chi-square test for CO observed data by using five dark matter halo profiles

Dark Matter Profile	χ^2_{redu} for CO observed data
Pseudoisothermal	11.16
NFW	14.40
Einasto	1.45
Core-modified	23.90
coreNFW	7.96

In Table 4.5, the χ^2_{redu} of five dark matter profiles for CO observed data are within a big range except for the Einasto profile. This is due to the fitting has a bad starting at the first internal radius obtained. The gap difference between the fitting model and the CO observed data at the first internal radius causes the value of χ^2_{redu} have a large number at this data point and affects the final χ^2_{redu} result. These four dark matter profiles have a better fitting starting from the second radius obtained until the external radius 7 kpc. Meanwhile, the extra third parameter of the Einasto profile, *n*, the Einasto index makes a very important role to overcome the hardly fitting at the first internal radius. The Einasto index, *n* describes the shape of overall profile distribution, the larger values of n result in steeper internal profiles and shallower external profiles (Graham et al., 2006). The flexibility of the third parameter adjustment makes the Einasto profile able to fit the CO observed data very well starting from the first internal radius until the external radius 7 kpc.

By using the free parameter obtained in Table 4.4, the total dark matter mass is calculated for CO observed data within 7 kpc radius by applying the five dark matter halo profiles respectively as shown in Table 4.6. The dark matter mass is obtained by using

the Equation (3.4), (3.10), (3.16), (3.19), (3.29) for Pseudoisothermal, NFW, Einasto, core-modified and coreNFW profiles respectively.

Table 4.6: Total dark matter mass for the five dark matter halo profiles by CO observed data within 7 kpc radius

Dark Matter Profile	Mass of dark matter by using CO observed data within 7 kpc radius (M⊙)
Pseudoisothermal	$(0.56 \pm 2.63) \times 10^{10}$
NFW	$(1.64 \pm 0.02) \times 10^{10}$
Einasto	$(1.46 \pm 0.01) \times 10^{10}$
Core-modified	$(1.08 \pm 0.44) \times 10^{10}$
coreNFW	$(1.71 \pm 0.01) \times 10^{10}$

In Table 4.6, the total mass of dark matter for the five accepted dark matter halo profiles within radius 7 kpc by CO observed data in this galaxy is on the range from $0.56 \pm 2.63 \times 10^{10}$ M⊙ to $1.71 \pm 0.01 \times 10^{10}$ M⊙. There are two reasons why the mass of dark matter by CO observed data is much smaller than HI observed data. The first reason is the maximum obtained radius by HI observed data is 10 kpc radius while by CO observed data is 7 kpc radius. The second reason is CO observed data is dominated in the central region of the galaxy (Garcia-Burillo et al., 1993; Kenney & Young, 1988; Nakai et al., 1994; Sakamoto et al., 1999; J. Young & Scoville, 1982; J. S. Young et al., 1995) but the maximum observed radius is not as far as HI observed data due to HI observed data able to detect three or four times than visible disk (A Bosma & Van der Kruit, 1979). By referring to Equation (3.36), the mass of dark matter is directly proportional to the radius times the square of velocity. The decreasing of dark matter velocity in the external radius of CO observed data causes its dark matter mass to be much smaller than the dark matter mass by HI observed data.

4.9 Increasing the accuracy of dark matter mass by considering dark matter mass by CO in the internal region adding with dark matter mass by HI in the external region

For the purpose to have a full picture of the dark matter mass in galaxy NGC 4321, the mass of dark matter is measured by considering both HI and CO, as discussed in the introduction section. The total dark matter mass within 10 kpc radius was measured by the addition of the dark matter mass by CO in the internal region with the dark matter mass by HI in the external region of the galaxy. To respond to the question addressed in the introduction, for the total dark matter mass, which range of internal radius should cover by CO and which range of external radius should cover by HI? The range of internal radius by CO and external radius by HI is calculated for each 0.1 kpc increment. First, the dark matter mass by CO from 0 to 0.1 kpc is added with dark matter mass by HI from 0.1 kpc to 10 kpc. The total dark matter mass by CO and HI was then compared with the dark matter mass by HI only within 10 kpc radius, compared in terms of increment in dark matter mass and the percentage of dark matter mass accuracy increment. Then increase the radius by 0.1 kpc, dark matter mass by CO from 0 kpc to 0.2 kpc added with dark matter mass by HI from 0.2 kpc to 10 kpc. The radius increases continuously until the total dark matter mass by CO and HI is less than the dark matter mass by HI only. The total dark matter mass and percentage of dark matter mass accuracy increment by using five dark matter profiles are as shown in Table 7. Due to too much data if put all calculations from 0 to 0.1 kpc, then each 0.1 kpc radius increment for each dark matter profile (45 rows data for each dark matter profile) so only present 0.5 kpc radius increment for each dark matter profile in Table 4.7. A graph of the overall radius will be plotted in Figure 4.6.

Table 4.7: The comparison between the total dark matter mass by CO in the internal region and by HI in the external region with the dark matter mass by HI only within 10 kpc radius by using five dark matter profiles.

Pseudoisothermal profile				
Internal radius range covered by CO observed data (kpc)	External radius range covered by HI observed data (kpc)	Total dark matter mass by CO in internal radius with HI in external radius (x 10^11 M⊙)	Total dark matter mass by CO and HI compared with dark matter mass by HI only (x 10^9 M⊙)	Percentage of dark matter mass accuracy increment (%)
0 to 0.1	0.1 to 10	1.08 ± 0.10	0.12 ± 0.02	0.11
0 to 0.5	0.5 to 10	1.10 ± 0.10	2.20 ± 0.04	2.05
0 to 1.0	1.0 to 10	1.12 ± 0.10	4.79 ± 0.05	4.45
0 to 1.5	1.5 to 10	1.14 ± 0.10	6.54 ± 0.22	6.08
0 to 2.0	2.0 to 10	1.15 ± 0.10	7.28 ± 0.46	6.77
0 to 2.5	2.5 to 10	1.15 ± 0.09	7.08 ± 0.83	6.58
0 to 3.0	3.0 to 10	1.14 ± 0.09	6.06 ± 1.12	5.63
0 to 3.5	3.5 to 10	1.12 ± 0.09	4.39 ± 1.53	4.08
0 to 4.0	4.0 to 10	1.10 ± 0.08	2.20 ± 1.98	2.05
0 to 4.5	4.5 to 10	1.07 ± 0.08	-0.42 ± 2.48	-0.39

Table 4.7, Continued.

NFW profile				
Internal radius range covered by CO observed data (kpc)	External radius range covered by HI observed data (kpc)	Total dark matter mass by CO in internal radius with HI in external radius (x 10^11 M⊙)	Total dark matter mass by CO and HI compared with dark matter mass by HI only (x 10^9 M⊙)	Percentage of dark matter mass accuracy increment (%)
0 to 0.1	0.1 to 10	1.19 ± 0.01	0.59 ± 0.30	0.50
0 to 0.5	0.5 to 10	1.22 ± 0.09	3.54 ± 8.00	2.99
0 to 1.0	1.0 to 10	1.24 ± 0.21	5.16 ± 20.48	4.35
0 to 1.5	1.5 to 10	1.24 ± 0.34	5.28 ± 33.33	4.45
0 to 2.0	2.0 to 10	1.23 ± 0.47	4.31 ± 46.28	3.64
0 to 2.5	2.5 to 10	1.21 ± 0.60	2.42 ± 59.28	2.04
0 to 3.0	3.0 to 10	1.18 ± 0.73	-0.27 ± 72.29	-0.23
0 to 3.5	3.5 to 10	1.15 ± 0.86	-3.68 ± 85.31	-3.10
0 to 4.0	4.0 to 10	1.11 ± 0.99	-7.77 ± 98.34	-6.55
0 to 4.5	4.5 to 10	1.06 ± 1.12	-12.51 ± 111.37	-10.55

Table 4.7, Continued.

Einasto profile				
Internal radius range covered by CO observed data (kpc)	External radius range covered by HI observed data (kpc)	Total dark matter mass by CO in internal radius with HI in external radius (x 10^11 M⊙)	Total dark matter mass by CO and HI compared with dark matter mass by HI only (x 10^9 M⊙)	Percentage of dark matter mass accuracy increment (%)
0 to 0.1	0.1 to 10	1.14 ± 0.0009	0.53 ± 0.37	0.47
0 to 0.5	0.5 to 10	1.16 ± 0.0004	2.83 ± 0.42	2.50
0 to 1.0	1.0 to 10	1.18 ± 0.0002	4.71 ± 0.44	4.17
0 to 1.5	1.5 to 10	1.18 ± 0.0002	5.28 ± 0.44	4.67
0 to 2.0	2.0 to 10	1.18 ± 0.0001	4.58 ± 0.45	4.05
0 to 2.5	2.5 to 10	1.16 ± 0.0001	2.73 ± 0.45	2.42
0 to 3.0	3.0 to 10	1.13 ± 0.0001	-0.14 ± 0.46	-0.12
0 to 3.5	3.5 to 10	1.09 ± 0.0001	-3.92 ± 0.46	-3.47
0 to 4.0	4.0 to 10	1.05 ± 0.0001	-8.49 ± 0.46	-7.51
0 to 4.5	4.5 to 10	0.99 ± 0.0001	-13.74 ± 0.46	-12.16

Table 4.7, Continued.

Core-modified profile				
Internal radius range covered by CO observed data (kpc)	External radius range covered by HI observed data (kpc)	Total dark matter mass by CO in internal radius with HI in external radius (x 10^11 M⊙)	Total dark matter mass by CO and HI compared with dark matter mass by HI only (x 10^9 M⊙)	Percentage of dark matter mass accuracy increment (%)
0 to 0.1	0.1 to 10	1.02 ± 0.003	0.18 ± 0.22	0.18
0 to 0.5	0.5 to 10	1.05 ± 0.02	3.94 ± 2.02	3.88
0 to 1.0	1.0 to 10	1.08 ± 0.03	6.24 ± 2.98	6.14
0 to 1.5	1.5 to 10	1.08 ± 0.04	6.64 ± 3.54	6.54
0 to 2.0	2.0 to 10	1.07 ± 0.04	5.51 ± 3.94	5.43
0 to 2.5	2.5 to 10	1.04 ± 0.04	2.92 ± 4.25	2.88
0 to 3.0	3.0 to 10	1.00 ± 0.05	-1.01 ± 4.50	-0.99
0 to 3.5	3.5 to 10	0.95 ± 0.05	-6.05 ± 4.71	-5.95
0 to 4.0	4.0 to 10	0.89 ± 0.05	-11.91 ± 4.90	-11.72
0 to 4.5	4.5 to 10	0.83 ± 0.05	-18.29 ± 5.06	-18.00

Table 4.7, Continued.

CoreNFW profile				
Internal radius range covered by CO observed data (kpc)	External radius range covered by HI observed data (kpc)	Total dark matter mass by CO in internal radius with HI in external radius (x 10^11 M⊙)	Total dark matter mass by CO and HI compared with dark matter mass by HI only (x 10^9 M⊙)	Percentage of dark matter mass accuracy increment (%)
0 to 0.1	0.1 to 10	1.05 ± 0.004	0.24 ± 0.24	0.23
0 to 0.5	0.5 to 10	1.09 ± 0.02	3.50 ± 1.91	3.34
0 to 1.0	1.0 to 10	1.11 ± 0.03	5.68 ± 3.06	5.40
0 to 1.5	1.5 to 10	1.11 ± 0.04	6.18 ± 3.82	5.88
0 to 2.0	2.0 to 10	1.10 ± 0.05	5.29 ± 4.39	5.03
0 to 2.5	2.5 to 10	1.08 ± 0.05	3.12 ± 4.84	2.97
0 to 3.0	3.0 to 10	1.05 ± 0.05	-0.14 ± 5.22	-0.13
0 to 3.5	3.5 to 10	1.01 ± 0.06	-4.34 ± 5.54	-4.13
0 to 4.0	4.0 to 10	0.96 ± 0.06	-9.31 ± 5.82	-8.86
0 to 4.5	4.5 to 10	0.90 ± 0.06	-14.88 ± 6.08	-14.16

In Table 4.7, for all five dark matter profiles, column 1 and column 2 illustrate the radius covered by CO and HI observed data respectively. Column 3 demonstrates the total dark matter mass by CO in the internal radius with HI in the external radius. Column 4 shows the total dark matter mass by CO and HI compared with dark matter mass by HI

only, which is the total dark matter mass in column 3 minus the total dark matter mass by HI observed data within 10 kpc radius in Table 6. Lastly, column 5 displays the percentage of dark matter mass accuracy increment by comparing total dark matter mass by CO and HI with total dark matter mass by HI only.

As the radius increases, the total dark matter mass by CO in the internal radius with HI in the external radius (column 3) increases until a peak then starts decreasing. As the radius increases, the radius covered by CO increasing and the radius covered by HI decreasing. Initially, the dark matter mass by CO increasing and the dark matter mass by HI decreasing due to the radius covered by HI decreasing. After a certain radius, the dark matter mass by both CO and HI observed data decreasing. This is because CO is rich in the internal region of the galaxy and the dark matter mass by CO starts decreasing after a certain radius. Next, for better illustration, the percentage of dark matter mass accuracy increment (column 5) against the radius by five dark matter profiles are plotted as shown in Figure 4.6.

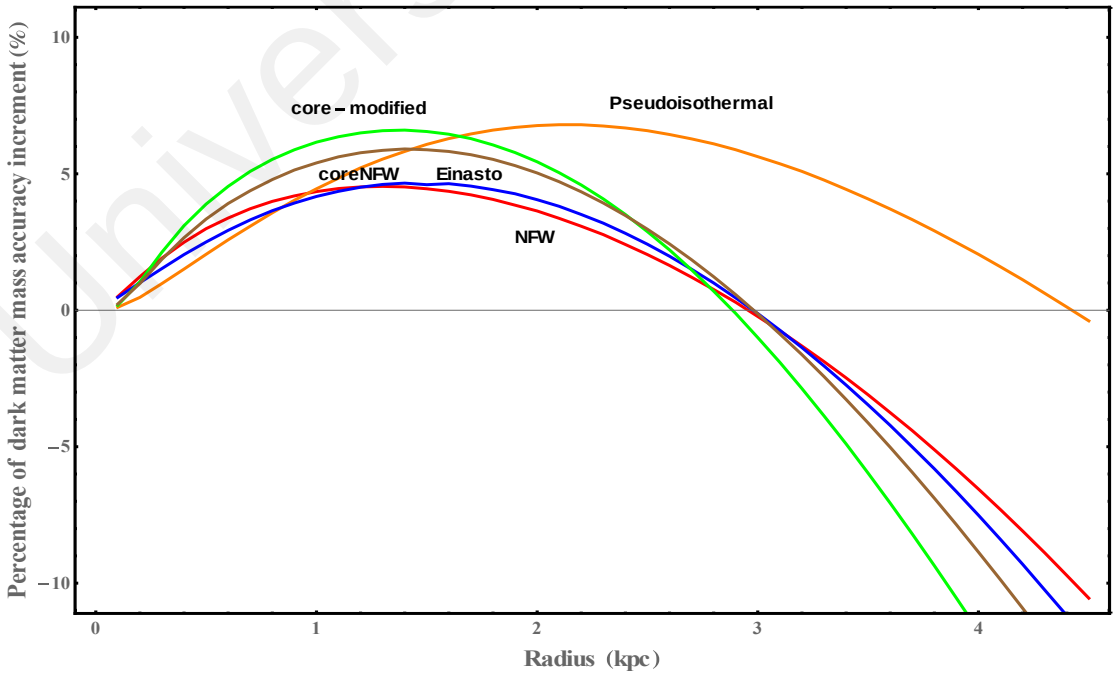

Figure 4.6: The percentage of dark matter mass accuracy increment against the radius by five dark matter profiles.

By referring to Table 4.7 and Figure 4.6, the internal radius covered by CO where the percentage of maximum increase in accuracy of dark matter mass achieved by five dark matter profiles is as shown in Table 4.8.

Table 4.8: The internal radius covered by CO where the percentage of maximum increase in accuracy of dark matter mass achieved by five dark matter profiles

Dark Matter Profile	Internal radius covered by CO where the percentage of maximum increase in accuracy of dark matter mass achieved (kpc)	Percentage of maximum increase in accuracy of dark matter mass (%)
Pseudoisothermal (orange)	2.2	6.79
NFW (red)	1.3	4.54
Einasto (blue)	1.5	4.67
Core-modified (green)	1.4	6.60
coreNFW (brown)	1.4	5.91

In Table 4.8, the percentage of maximum increase in accuracy of dark matter mass achieved when the internal radius covered by CO from 0 kpc until the radius between the range of 1.3 kpc to 2.2 kpc and the percentage of maximum increase in accuracy of dark matter mass is between the ranges of 4% to 7%. Among these five dark matter profiles, the Pseudoisothermal profile has a higher radius and both Pseudoisothermal and core-modified profiles have a slightly higher percentage compared to other dark matter halo models. The range of radius and percentage will be reduced by looking at NFW, Einasto, and coreNFW these three profiles only. By looking at these three profiles, percentage of

maximum accuracy increase in dark matter mass achieved when the internal radius covered by CO from 0 kpc until the radius between the range of 1.3 kpc to 1.5 kpc and percentage of maximum increase in accuracy of dark matter mass is in between the range of 4% to 6%. The small range of these three profiles indicates that there is a consistency for the maximum increment in the accuracy of dark matter mass in the galaxy NGC 4321 by the inclusion of CO.

Furthermore, in Figure 4.6, all dark matter profiles show a negative percentage after a certain radius. This means the dark matter mass by CO and HI will be less than the dark matter mass by HI only after a certain radius. The reason has been discussed on page 24, which is because CO is rich in the center part of the galaxy and the mass of dark matter by CO starts decreasing after a certain radius. In Figure 4.6, Pseudoisothermal and core-modified profiles show a negative percentage after 4.4 kpc and 2.8 kpc radius respectively. Meanwhile, the NFW, Einasto and coreNFW profiles illustrate a negative percentage after an exactly same radius, 2.9 kpc.

CHAPTER 5: CONCLUSION AND FUTURE RECOMMENDATIONS

By referring to the original first objective of this thesis, the dark matter distribution in the galaxy NGC 4321 has been analyzed to a larger radius by applying HI observed data. Previous dark matter studies in the galaxy by Ali (Ali et al., 2019) focused in the central region, up to a radius of 0.7 kpc by applying CO observed data. In this research, the dark matter distribution was analyzed up to a radius of 10 kpc by applying HI observed data, which extends the understanding of the dark matter distribution in the galaxy NGC 4321.

By referring to the original second objective of this thesis, it is found that the Pseudoisothermal profile is the best model among the nine dark matter profiles in the galaxy NGC 4321. The Pseudoisothermal profile is linearly at the internal region and flat at the large radii. This fitting characteristic is very suitable on this galaxy with the best fitting among the nine dark matter halo models with a x^2_{redu} of 1.25.

By referring to the original third objective of this thesis, it is found that the mass of dark matter for the four accepted profiles (NFW, coreNFW, Einasto and Pseudoisothermal) is within the range from $(1.08 \pm 0.01) \times 10^{11}$ M⊙ to $(1.19 \pm 0.10) \times 10^{11}$ M⊙. To be more precise, the Pseudoisothermal profile achieved the best fitting among the nine dark matter profiles and the dark matter mass of the Pseudoisothermal profile is $(1.08 \pm 0.01 \times 10^{11})$ M⊙.

By referring to the original fourth objective of this thesis, the accuracy of dark matter mass improved in the galaxy NGC 4321 was evaluated by considering both HI and CO in those five accepted dark matter halo profiles. Out of five dark matter profiles, three dark matter profiles are found to have consistency on the dark matter mass increment in galaxy NGC 4321, which are NFW, Einasto, and coreNFW profiles. The percentage of maximum increase in accuracy of dark matter mass of these three dark matter profiles

achieved in the range of 4% to 6% when the internal region covered by CO is from 0 kpc until the radius within the range of 1.3 kpc to 1.5 kpc. Furthermore, the radius of total dark matter mass by CO and HI less than dark matter mass by HI only is the same and consistent, 2.9 kpc. The consistencies of these three dark matter profiles indicate that the maximum dark matter mass accuracy will be increased by the inclusion of CO observed data in the internal region of the galaxy. This dark matter mass study by the inclusion of CO observed data in the internal region of the galaxy can be implemented to more and more galaxies to increase the accuracy of dark matter mass in the respective galaxies.

The dark matter of spiral galaxy NGC 4321 has been successfully analyzed by using the nine dark matter profiles and by using both HI and CO observed data. Nevertheless, the research in science is always can be enhanced. In spiral galaxy NGC 4321, Pseudoisothermal profile is the best fitted dark matter profile and the percentage of maximum increase in accuracy of dark matter mass achieved in the range of 4% to 6% when the internal region covered by CO is from 0 kpc until the radius within the range of 1.3 kpc to 1.5 kpc, however, the data size is one galaxy only. The suggested future research for this work is the nine dark matter profiles and the dark matter mass calculation by the inclusion of CO can be widely implemented to more and more spiral galaxies in the universe. By implementing the nine dark matter profiles and inclusion of CO to more and more spiral galaxies, we will have more data size and can judge better on which dark matter profile is the best fitted profile and the percentage of maximum increase in accuracy of dark matter mass achieved can be determined for overall spiral galaxies.

REFERENCES

Ali, I., Hwang, C.-Y., & Abidin, Z. Z. (2019). Dark Matter In The Central Region Of The Spiral Galaxy NGC4321. *Journal of Fundamental and Applied Sciences, 11*(2), 632-650.

Allaert, F., Gentile, G., & Baes, M. (2017). Testing baryon-induced core formation in ΛCDM: A comparison of the DC14 and coreNFW dark matter halo models on galaxy rotation curves. *Astronomy & Astrophysics, 605*, Article#A55.

Allard, E. L., Knapen, J. H., Peletier, R. F., & Sarzi, M. (2006). The star formation history and evolution of the circumnuclear region of M100. *Monthly Notices of the Royal Astronomical Society, 371*(3), 1087-1105.

Azeez, J. H., Hwang, C.-Y., Abidin, Z. Z., & Ibrahim, Z. A. (2016). Kennicutt-Schmidt law in the central region of NGC 4321 as seen by ALMA. *Scientific reports, 6*, Article#26896.

Babcock, H. W. (1939). The rotation of the Andromeda Nebula. *Lick Observatory Bulletin, 19*, 41-51.

Barnes, D. G., Staveley-Smith, L., de Blok, W. e. a., Oosterloo, T., Stewart, I. M., Wright, A., . . . Calabretta, M. (2001). The H i Parkes All Sky Survey: southern observations, calibration and robust imaging. *Monthly Notices of the Royal Astronomical Society, 322*(3), 486-498.

Begeman, K. (1989). HI rotation curves of spiral galaxies. I-NGC 3198. *Astronomy and Astrophysics, 223*, 47-60.

Begeman, K., Broeils, A., & Sanders, R. (1991). Extended rotation curves of spiral galaxies: Dark haloes and modified dynamics. *Monthly Notices of the Royal Astronomical Society, 249*(3), 523-537.

Belkora, L. (2002). *Minding the heavens: the story of our discovery of the Milky Way*. Florida, United States: CRC Press.

Bergh, S., & Van den Bergh, S. (1998). *Galaxy morphology and classification*. Cambridge, England: Cambridge University Press.

Bertone, G., & Hooper, D. (2018). History of dark matter. *Reviews of Modern Physics, 90*(4), Article#045002.

Bevington, P., & Robinson, D. (1969). Least-squares fit to an arbitrary function. *Data Reduction and Error Analysis for the Physical Sciences*, 204-246.

Binney, J., Binney, J., Michael, M., & Merrifield, M. (1998). *Galactic astronomy* (Vol. 9). New Jersey, United States: Princeton University Press.

Bosma, A. (1978). *The distribution and kinematics of neutral hydrogen in spiral galaxies of various morphological types.* Rijksuniversiteit te Groningen., Groningen, Netherland.

Bosma, A. (1981). 21-cm line studies of spiral galaxies. I-Observations of the galaxies NGC 5033, 3198, 5055, 2841, and 7331. *The Astronomical Journal, 86*, 1791-1824.

Bosma, A., & Van der Kruit, P. (1979). The local mass-to-light ratio in spiral galaxies. *Astronomy and Astrophysics, 79*, 281-286.

Bowman, J. D. (2008). *HI and Cosmology: What We Need To Know.* Paper presented at the AIP Conference Proceedings.

Briggs, D. (1995). *High Fidelity Deconvolution of Moderately Resolved Sources.* New Mexico Institute of Mining Technology, Socorro, New Mexico, USA.

Brownstein, J. R. (2009). Modified gravity and the phantom of dark matter. *Ph. D. Thesis*.

Burbidge, E. M., & Burbidge, G. (1960). Motions in Barred Spiral Galaxies. I. The Nuclei of NGC 1097 and NGC 1365. *The Astrophysical Journal, 132*, Article#30.

Burkert, A. (1995). The structure of dark matter halos in dwarf galaxies. *The Astrophysical Journal Letters, 447*(1), Article#L25.

Cavin, J. D. (2012). The Charles Messier Catalog. In *The Amateur Astronomer's Guide to the Deep-Sky Catalogs* (pp. 123-129). New York, United States: Springer.

Cepa, J., Beckman, J., Knapen, J., Nakai, N., & Kuno, N. (1992). Star formation in the spiral arms of NGC 4321. I-CO observations. *The Astronomical Journal, 103*, 429-435.

Chemin, L., De Blok, W., & Mamon, G. A. (2011). Improved modeling of the mass distribution of disk galaxies by the Einasto halo model. *The Astronomical Journal, 142*(4), Article#109.

Chung, A., Van Gorkom, J., Kenney, J. D., Crowl, H., & Vollmer, B. (2009). VLA imaging of Virgo spirals in atomic gas (VIVA). I. The Atlas and the HI properties. *The Astronomical Journal, 138*(6), Article#1741.

Ciambur, B. C., & Graham, A. W. (2016). Quantifying the (X/peanut)-shaped structure in edge-on disc galaxies: length, strength, and nested peanuts. *Monthly Notices of the Royal Astronomical Society, 459*(2), 1276-1292.

Cintio, A. D., Brook, C. B., Dutton, A. A., Macciò, A. V., Stinson, G. S., & Knebe, A. (2014). A mass-dependent density profile for dark matter haloes including the influence of galaxy formation. *Monthly Notices of the Royal Astronomical Society, 441*(4), 2986-2995.

Combes, F. (1991). Distribution of CO in the Milky Way. *Annual Review of Astronomy and Astrophysics, 29*(1), 195-237.

Danver, C.-G. (1942). A Morphological Investigation of Some Near Galaxies with Regard to the Lengths and the Form of their Arms, their Inclinations and their Symmetry Properties. *Annals of the Observatory of Lund, 10*, 3-193.

De Blok, W., McGaugh, S. S., & Rubin, V. C. (2001). High-resolution rotation curves of low surface brightness galaxies. II. Mass models. *The Astronomical Journal, 122*(5), Article#2396.

De Blok, W., Walter, F., Brinks, E., Trachternach, C., Oh, S., & Kennicutt Jr, R. (2008). High-resolution rotation curves and galaxy mass models from THINGS. *The Astronomical Journal, 136*(6), Article#2648.

De Naray, R. K., McGaugh, S. S., De Blok, W., & Bosma, A. (2006). High-resolution optical velocity fields of 11 low surface brightness galaxies. *The Astrophysical Journal Supplement Series, 165*(2), Article#461.

De Vaucouleurs, G. (1959). General physical properties of external galaxies. In *Astrophysik IV: Sternsysteme/Astrophysics IV: Stellar Systems* (pp. 311-372). New York, United States: Springer.

Di Paolo, C., Salucci, P., & Erkurt, A. (2019). The universal rotation curve of low surface brightness galaxies–IV. The interrelation between dark and luminous matter. *Monthly Notices of the Royal Astronomical Society, 490*(4), 5451-5477.

Diemand, J., Moore, B., & Stadel, J. (2004). Convergence and scatter of cluster density profiles. *Monthly Notices of the Royal Astronomical Society, 353*(2), 624-632.

Donato, F., Gentile, G., Salucci, P., Frigerio Martins, C., Wilkinson, M., Gilmore, G., . . . Wyse, R. (2009). A constant dark matter halo surface density in galaxies. *Monthly Notices of the Royal Astronomical Society, 397*(3), 1169-1176.

Džudžar, R., Kilborn, V., Meurer, G., Sweet, S. M., Drinkwater, M., Bekki, K., . . . Putman, M. (2019). The neutral hydrogen properties of galaxies in gas-rich groups. *Monthly Notices of the Royal Astronomical Society, 483*(4), 5409-5425.

Einasto, J., Kaasik, A., & Saar, E. (1974). Dynamic evidence on massive coronas of galaxies. *Nature, 250*(5464), 309-310.

Elmegreen, D. M., & Elmegreen, B. G. (1987). Arm classifications for spiral galaxies. *The Astrophysical Journal, 314*, 3-9.

Ewen, H. I., & Purcell, E. M. (1951). Observation of a line in the galactic radio spectrum. In *Classics in Radio Astronomy* (pp. 328-330). New York, United States: Springer.

Faber, S., & Jackson, R. E. (1976). Velocity dispersions and mass-to-light ratios for elliptical galaxies. *The Astrophysical Journal, 204*, 668-683.

Ferrarese, L., Freedman, W. L., Hill, R. J., Saha, A., Madore, B. F., Kennicutt Jr, R. C., . . . Hoessel, J. G. (1996). The extragalactic distance scale key project. Iv. The discovery of Cepheids and a new distance to M100 using the Hubble Space Telescope. *The Astrophysical Journal, 464*, Article#568.

Frank, B. S., de Blok, W., Walter, F., Leroy, A., & Carignan, C. (2016). The Impact of Molecular Gas on Mass Models of Nearby Galaxies. *The Astronomical Journal, 151*(4), Article#94.

Freeman, K. C. (1970). On the disks of spiral and S0 galaxies. *The Astrophysical Journal, 160*, Article#811.

Gammaldi, V., Karukes, E., & Salucci, P. (2018). Theoretical predictions for dark matter detection in dwarf irregular galaxies with gamma rays. *Physical Review D, 98*(8), Article#083008.

Garcia-Burillo, S., Guelin, M., & Cernicharo, J. (1993). CO in M51-Part One-Molecular Spiral Structure. *Astronomy and Astrophysics, 274*, Article#123.

Gott III, J. R., Jurić, M., Schlegel, D., Hoyle, F., Vogeley, M., Tegmark, M., . . . Brinkmann, J. (2005). A Map of the Universe. *The Astrophysical Journal, 624*(2), Article#463.

Graham, A. W., Merritt, D., Moore, B., Diemand, J., & Terzić, B. (2006). Empirical models for dark matter halos. II. Inner profile slopes, dynamical profiles, and ρ/σ3. *The Astronomical Journal, 132*(6), Article#2701.

Graham, A. W., & Worley, C. C. (2008). Inclination-and dust-corrected galaxy parameters: bulge-to-disc ratios and size–luminosity relations. *Monthly Notices of the Royal Astronomical Society, 388*(4), 1708-1728.

Gunn, J. E., & Gott III, J. R. (1972). On the infall of matter into clusters of galaxies and some effects on their evolution. *The Astrophysical Journal, 176*, Article#1.

Hashim, N., Abidin, Z., Ibrahim, U., Hassan, M., Hamidi, Z., Umar, R., & Ibrahim, Z. (2015). The nonlinear least square fitting for rotation curve of orion dwarf spiral. *Sains Malaysiana, 44*(3), 457-462.

Helfer, T. T., Thornley, M. D., Regan, M. W., Wong, T., Sheth, K., Vogel, S. N., . . . Bock, D. C.-J. (2003). The BIMA survey of nearby galaxies (BIMA SONG). II. The CO data. *The Astrophysical Journal Supplement Series, 145*(2), Article#259.

Hellwig, H., Vessot, R. F., Levine, M. W., Zitzewitz, P. W., Allan, D. W., & Glaze, D. J. (1970). Measurement of the unperturbed hydrogen hyperfine transition frequency. *IEEE Transactions on Instrumentation and Measurement, 19*(4), 200-209.

Henbest, N., & Couper, H. (1994). *The guide to the galaxy*. Cambridge, England: Cambridge United Press.

Hernquist, L. (1990). An analytical model for spherical galaxies and bulges. *The Astrophysical Journal, 356*, 359-364.

Herschel, W. (2012). 'The Scientific Papers of Sir William Herschel'at 100. *Astronomy & Geophysics, 53*(2), 2-13.

Hess, K. M., Cluver, M., Yahya, S., Leisman, L., Serra, P., Lucero, D. M., . . . Carignan, C. (2017). H i in group interactions: HCG 44. *Monthly Notices of the Royal Astronomical Society, 464*(1), 957-967.

Holmberg, E. (1958). A photographic photometry of extragalactic nebulae. *Meddelanden fran Lunds Astronomiska Observatorium Serie, 136*, Article#1.

Horesh, A., & Sfaradi, I. (2020). A VLA Radio Detection of Supernova SN2020oi. *Transient Name Server AstroNote, 10*, Article#1.

Hubble, E. (1934). The realm of the nebulae. *The Scientific Monthly, 39*(3), 193-202.

Jarrett, T. (2000). Near‐Infrared Galaxy Morphology Atlas. *Publications of the Astronomical Society of the Pacific, 112*(774), Article#1008.

Jimenez, R., Verde, L., & Oh, S. P. (2003). Dark halo properties from rotation curves. *Monthly Notices of the Royal Astronomical Society, 339*(1), 243-259.

Jog, C. J. (2002). Large-scale asymmetry of rotation curves in lopsided spiral galaxies. *Astronomy & Astrophysics, 391*(2), 471-479.

Kahn, F., & Woltjer, L. (1959). Intergalactic Matter and the Galaxy. *The Astrophysical Journal, 130*, Article#705.

Kenney, J. D., & Young, J. S. (1988). CO observations of all Virgo Cluster spiral galaxies brighter than B (T) exp 0= 12. *The Astrophysical Journal Supplement Series, 66*, 261-296.

Klypin, A., Kravtsov, A. V., Bullock, J. S., & Primack, J. R. (2001). Resolving the structure of cold dark matter halos. *The Astrophysical Journal, 554*(2), Article#903.

Knapen, J., Shlosman, I., Heller, C., Rand, R., Beckman, J., & Rozas, M. (2000). Kinematics of ionized and molecular hydrogen in the core of M100. *The Astrophysical Journal, 528*(1), 219.

Knapen, J. H., Cepa, J., Beckman, J. E., Soledad del Rio, M., & Pedlar, A. (1993). Star Formation in the Spiral Arms of NGC 4321. II. H i Distribution and Kinematics. *The Astrophysical Journal, 416*, Article#563.

Koopmann, R. A., & Kenney, J. D. (2004). Hα morphologies and environmental effects in virgo cluster spiral galaxies. *The Astrophysical Journal, 613*(2), Article#866.

Koopmann, R. A., Kenney, J. D., & Young, J. (2001). An Atlas of Hα and R Images and Radial Profiles of 63 Bright Virgo Cluster Spiral Galaxies. *The Astrophysical Journal Supplement Series, 135*(2), Article#125.

Larsen, W. A., & McCleary, S. J. (1972). The use of partial residual plots in regression analysis. *Technometrics, 14*(3), 781-790.

Li, P., Lelli, F., McGaugh, S., & Schombert, J. (2020). A comprehensive catalog of dark matter halo models for SPARC galaxies. *The Astrophysical Journal Supplement Series, 247*(1), 31.

Li, X., Tang, L., & Lin, H.-N. (2017). Comparing dark matter models, modified Newtonian dynamics and modified gravity in accounting for galaxy rotation curves. *Chinese Physics C, 41*(5), Article#055101.

Lindblad, B. (1925). On the cause of star-streaming. *The Astrophysical Journal, 62*, Article#191.

Mackie, G. (1999). To see the Universe in a Grain of Taranaki Sand. Melbourne, Australia: Swinburne University of Technology.

Marov, M. Y. (2015). The Structure of the Universe. In *The Fundamentals of Modern Astrophysics* (pp. 279-294). New York, United States: Springer.

Mayall, N. (1951). In the structure of the galaxy. *Ann Arbor: Univ. Mich. Press, 19*.

Melvin, T., Masters, K., Lintott, C., Nichol, R. C., Simmons, B., Bamford, S. P., . . . Fortson, L. (2014). Galaxy Zoo: an independent look at the evolution of the bar fraction over the last eight billion years from HST-COSMOS. *Monthly Notices of the Royal Astronomical Society, 438*(4), 2882-2897.

Millar, A. J. (2014). *Dark Matters.* University of Melbourne, Melbourne, Australia.

Moore, B., Quinn, T., Governato, F., Stadel, J., & Lake, G. (1999). Cold collapse and the core catastrophe. *Monthly Notices of the Royal Astronomical Society, 310*(4), 1147-1152.

Muller, C. A., & Oort, J. H. (1951). Observation of a line in the galactic radio spectrum: the interstellar hydrogen line at 1,420 Mc./sec., and an estimate of galactic rotation. *Nature, 168*(4270), 357-358.

Nakai, N., Kuno, N., Handa, T., & Sofue, Y. (1994). Distribution and dynamics of molecular gas in the galaxy M51. 1: data and spiral structure. *Publications of the Astronomical Society of Japan, 46*, 527-538.

Navarro, J., Ludlow, A., Springel, V., Wang, J., Vogelsberger, M., White, S., . . . Helmi, A. (2010). The diversity and similarity of cold dark matter halos. *Monthly Notices of the Royal Astronomical Society, 402*, Article#21.

Navarro, J. F., Frenk, C. S., & White, S. D. (1997). A universal density profile from hierarchical clustering. *The Astrophysical Journal, 490*(2), 493.

Oikawa, S., & Sofue, Y. (2014). Rotation curve anomaly and galactic warp in M 51. *Publications of the Astronomical Society of Japan, 66*(4).

Oort, J. (1941). Note on the structure of the inner parts of the galactic system. *Bulletin of the Astronomical Institutes of the Netherlands, 9*, Article#193.

Oort, J. H. (1940). Some Problems Concerning the Structure and Dynamics of the Galactic System and the Elliptical Nebulae NGC 3115 and 4494. *Astrophysical Journal*, Article#91.

Ostriker, J., Peebles, P., & Yahil, A. (1974). The size and mass of galaxies, and the mass of the universe. *The Astrophysical Journal, 193*, L1-L4.

Ostriker, J. P., & Peebles, P. J. (1973). A numerical study of the stability of flattened galaxies: or, can cold galaxies survive? *The Astrophysical Journal, 186*, 467-480.

Padmanabhan, H. (2017). Neutral hydrogen in the post-reionization universe. *Proceedings of the International Astronomical Union, 12*(S333), 216-221.

Page, T. (1952). Radial Velocities and Masses of Double Galaxies. *The Astrophysical Journal, 116*, Article#63.

Parsons, W. (1968). third Earl of Rosse. *Hermathena*(107), 5-13.

Pease, F. (1918). The rotation and radial velocity of the central part of the Andromeda nebula. *Proceedings of the National Academy of Sciences of the United States of America, 4*(1), Article#21.

Persic, M., Salucci, P., & Stel, F. (1996). The universal rotation curve of spiral galaxies—I. The dark matter connection. *Monthly Notices of the Royal Astronomical Society, 281*(1), 27-47.

Randriamampandry, T. H., & Carignan, C. (2014). Galaxy mass models: MOND versus dark matter haloes. *Monthly Notices of the Royal Astronomical Society, 439*(2), 2132-2145.

Read, J., Agertz, O., & Collins, M. (2016). Dark matter cores all the way down. *Monthly Notices of the Royal Astronomical Society, 459*(3), 2573-2590.

Retana-Montenegro, E., Van Hese, E., Gentile, G., Baes, M., & Frutos-Alfaro, F. (2012). Analytical properties of Einasto dark matter haloes. *Astronomy & Astrophysics, 540*, Article#A70.

Roberts, M., & Rots, A. (1973). Comparison of rotation curves of different galaxy types. *Astronomy and Astrophysics, 26*, 483-485.

Rogstad, D., & Shostak, G. (1972). Gross properties of five Scd galaxies as determined from 21-centimeter observations. *The Astrophysical Journal, 176*, Article#315.

Rubin, V. C., & Ford Jr, W. K. (1970). Rotation of the Andromeda nebula from a spectroscopic survey of emission regions. *The Astrophysical Journal, 159*, Article#379.

Rubin, V. C., Ford Jr, W. K., & Thonnard, N. (1978). Extended rotation curves of high-luminosity spiral galaxies. IV-Systematic dynamical properties, SA through SC. *The Astrophysical Journal, 225*, L107-L111.

Rubin, V. C., Ford Jr, W. K., & Thonnard, N. (1980). Rotational properties of 21 SC galaxies with a large range of luminosities and radii, from NGC 4605/R= 4kpc/to UGC 2885/R= 122 kpc. *The Astrophysical Journal, 238*, 471-487.

Sakamoto, K., Okumura, S., Minezaki, T., Kobayashi, Y., & Wada, K. (1995). Bar-Driven Gas Structure and Star Formation in the Center of M100. *The Astronomical Journal, 110*, Article#2075.

Sakamoto, K., Okumura, S. K., Ishizuki, S., & Scoville, N. (1999). CO images of the central regions of 20 nearby spiral galaxies. *The Astrophysical Journal Supplement Series, 124*(2), Article#403.

Salucci, P., & Burkert, A. (2000). Dark matter scaling relations. *The Astrophysical Journal Letters, 537*(1), Article#L9.

Schwarzschild, M. (1954). Mass distribution and mass-luminosity ratio in galaxies. *The Astronomical Journal, 59*, Article#273.

Shelest, A., & Lelli, F. (2020). From spirals to lenticulars: Evidence from the rotation curves and mass models of three early-type galaxies. *Astronomy & Astrophysics, 641*, Article#A31.

Slipher, V. (1914). The radial velocity of the Andromeda nebula. *Popular Astronomy, 22*, 19-21.

Smith, S. (1936). The mass of the Virgo cluster. *The Astrophysical Journal, 83*, Article#23.

Sofue, Y. (1997). Nuclear-to-Outer Rotation Curves of Galaxies in the CO and HI lines. *Publications of the Astronomical Society of Japan, 49*(1), 17-46.

Sofue, Y. (2013). Mass Distribution and Rotation Curve in the Galaxy. *Planets, Stars, Stellar System. Volume 5: Galactic Structure Stellar Populations, 5*, Article#985.

Sofue, Y., & Rubin, V. (2001). Rotation curves of spiral galaxies. *Annual Review of Astronomy and Astrophysics, 39*(1), 137-174.

Sofue, Y., Tutui, Y., Honma, M., Tomita, A., Takamiya, T., Koda, J., & Takeda, Y. (1999). Central rotation curves of spiral galaxies. *The Astrophysical Journal, 523*(1), Article#136.

Sparke, L. S., & Gallagher III, J. S. (2007). *Galaxies in the universe: an introduction*. Cambridge, England: Cambridge University Press.

Spence, J. R., & Stanley, D. J. (2016). Prediction interval: What to expect when you're expecting… A replication. *PloS ONE, 11*(9), e0162874.

Storey, J., Ashley, M., Naray, M., & Lloyd, J. (1994). 21 cm line of atomic hydrogen. *American Journal of Physics, 62*(12), 1077-1081.

Sullivan, W. T. (2012). *Classics in radio astronomy* (Vol. 10). New York, United States: Springer Science & Business Media.

Tank, H. K. (2015). Understanding Galaxy Rotation Curves in terms of Interference of Gravitational Waves. *viXra*.

Thompson, A. R., Clark, B., Wade, C., & Napier, P. J. (1980). The very large array. *The Astrophysical Journal Supplement Series, 44*, 151-167.

Tiley, A. L., Swinbank, A., Harrison, C., Smail, I., Turner, O., Schaller, M., . . . Sharples, R. (2019). The shapes of the rotation curves of star-forming galaxies over the last $\approx$ 10 Gyr. *Monthly Notices of the Royal Astronomical Society, 485*(1), 934-960.

Uson, J. M., Boughn, S. P., & Kuhn, J. R. (1990). The central galaxy in Abell 2029: an old supergiant. *Science, 250*(4980), 539-540.

Vafaei Sadr, A., Vos, E. E., Bassett, B. A., Hosenie, Z., Oozeer, N., & Lochner, M. (2019). DEEPSOURCE: point source detection using deep learning. *Monthly Notices of the Royal Astronomical Society, 484*(2), 2793-2806.

Van de Hulst, H. (1982). Origin of the Radio Waves from Space. In *Classics in Radio Astronomy* (pp. 302-316). New York, United States: Springer.

Van der Kruit, P. (1973). The compression strength of NGC 4321 and comparison with M51. *The Astronomical Journal, 186*, 807-813.

Verdes-Montenegro, L., Yun, M., Williams, B., Huchtmeier, W., Del Olmo, A., & Perea, J. (2001). Where is the neutral atomic gas in Hickson groups? *Astronomy & Astrophysics, 377*(3), 812-826.

Whitehurst, R. N., & Roberts, M. S. (1972). High-Velocity Neutral Hydrogen in the Central Region of the Andromeda Galaxy. *The Astrophysical Journal, 175*, Article#347.

Williams, M. J., Bureau, M., & Cappellari, M. (2009). Kinematic constraints on the stellar and dark matter content of spiral and S0 galaxies. *Monthly Notices of the Royal Astronomical Society, 400*(4), 1665-1689.

Wolf, M. (1914). Vierteljahresschr Astron. *Ges, 49*, Article#162.

Wong, T., & Blitz, L. (2002). The relationship between gas content and star formation in molecule-rich spiral galaxies. *The Astrophysical Journal, 569*(1), Article#157.

Wootten, A., & Thompson, A. R. (2009). The Atacama large millimeter/submillimeter array. *Proceedings of the IEEE, 97*(8), 1463-1471.

Wozniak, H., Friedli, D., Martinet, L., & Pfenniger, D. (1999). *Double-barred starburst galaxies viewed by ISOCAM.* Paper presented at the The Universe as Seen by ISO.

Xin, X.-S., & Zheng, X.-W. (2013). A revised rotation curve of the Milky Way with maser astrometry. *Research in Astronomy and Astrophysics, 13*(7), Article#849.

Young, J., & Scoville, N. (1982). Extragalactic CO-Gas distributions which follow the light in IC 342 and NGC 6946. *The Astrophysical Journal, 258*, 467-489.

Young, J. S., Xie, S., Tacconi, L., Knezek, P., Viscuso, P., Tacconi-Garman, L., . . . Lord, S. (1995). The FCRAO extragalactic CO survey. I. The data. *The Astrophysical Journal Supplement Series, 98*, Article#219.

Yuan, C., & Kuo, C.-l. (1998). Spiral structure in the central disks of NGC 1068 and M100. *The Astrophysical Journal, 497*(2), Article#689.

Yun, M. S., Ho, P. T., & Lo, K. (1994). A high-resolution image of atomic hydrogen in the M81 group of galaxies. *Nature, 372*(6506), 530-532.

Zackrisson, E. (2005). *Introduction to Dark Matter.* Uppsala University, Uppsala, Sweden.

Zasov, A. V., Saburova, A. S., Khoperskov, A. V., & Khoperskov, S. A. (2017). Dark matter in galaxies. *Physics-Uspekhi, 60*(1), Article#3.

Zhao, H. (1996). Analytical models for galactic nuclei. *Monthly Notices of the Royal Astronomical Society, 278*(2), 488-496.

Zwicky, F. (1933). Helvetica Physica Acta, 6, 110. *Die Rotverschiebung von extragalaktischen Nebeln*.

Zwicky, F. (1933). The redshift of extragalactic nebulae. *Helv. Phys. Acta, 6*(110), Article#138.